北海道大学大学院情報科学院

［博士論文］

# 集中巻を用いた永久磁石同期モータの高効率化に関する研究

# A study on Enhancing Efficiency of IPMSM Adopting Concentrated Winding Structure

令和５年

指導教員　小笠原　悟司　教授

提出者

専攻　情報科学専攻

学生番号　46195207

氏名　陶　咸吉　（TAO Xianji）

# Abstract

According to calculations, consumption of electromotors accounts for about half of total power generation [3]. On the other hand, taking Japan as an example, 75.7% of power generation in 2019 came from burning fossil fuels [4], which produced a large amount of greenhouse gas. With global warming and the depletion of fossil fuels, energy-saving and emission reductions have become a problem that cannot be ignored.

Generators or electromotors are generally rotating electric machines. Considering the electrical energy generated or consumed by rotating electric machines, even a tiny increase in the efficiency of rotating electric machines can result in significant energy-saving and emission reductions. Moreover, the heat dissipation system can be reduced or eliminated by enhancing efficiency and reducing losses, which can decrease system complexity and increase operational reliability. Among rotating electric machines, interior permanent magnet synchronous machines (IPMSMs) are widely used for rotating electric machines in recent years because of their outstanding characteristics, such as simply structure, high power density, and high efficiency.

On the other hand, although the efficiency of IPMSMs should be enhanced as much as possible, manufacturing difficulties and costs are always a major concern for enterprises. Compared with disturbed windings, concentrated windings have been widely adopted in IPMSMs for their shorter coil ending, which can cut manufacturing costs by reducing the usage of copper, and at the same time, the limited space effectively can be effectively used. Therefore, the objective of this paper is to enhance the efficiency of IPMSMs adopting concentrated windings while taking manufacturing difficulties and costs into account.

This paper mainly consists of two topics. The first topic proposes a novel rotor structure which can enhance the efficiency of an IPMSM adopting concentrated windings in the wide-speed, middle-torque operating area. The second topic focuses on the reduction in eddy current loss of special rectangular windings in a high-torque IPMSM used for a wind generator. The first topic is from the perspective of the rotor, and the second is to improve the efficiency of IPMSM from the perspective of the stator. Both two topics are discussed by FEM (finite element method) first, and prototype machines are manufactured to verify the FEM results.

Keyword: IPMSM, IPMSG, Concentrated windings, High efficiency, Flux barrier, Disproportional airgap, High-torque, Rectangular windings, Eddy current loss, Wind generator

# Contents

# Chapter 1. Introduction and Basic Concepts of IPMSM

As mentioned in the abstract, with global warming and the depletion of fossil fuels, higher energy-saving standards are required for rotating electric machines. The objective of this paper is to enhance the efficiency of interior permanent magnet synchronous machines (IPMSMs) adopting concentrated windings while taking manufacturing difficulties and costs into account. And this paper mainly consists of two topics. The first topic proposes a novel rotor structure which can enhance the efficiency of an IPMSM adopting concentrated windings in the wide-speed, middle-torque operating area. The second topic focuses on the reduction in eddy current loss of special rectangular windings in a high-torque IPMSM used for a wind generator. Both two topics are discussed by FEM (finite element method) first, and prototype machines are manufactured to verify the FEM results.

Although there are some similarities between the two topic models, their usage scenarios are different. Therefore, the research background and direction of each topic will be given in their respective chapters. The basic concepts of IPMSM will be given here to make it easier to understand the contents of this paper.

## Section 1.1 Difference between distributed and concentrated windings

Distributed windings and concentrated windings are the two main types of windings in IPMSMs. The comparison between distributed and concentrated windings is shown in Fig. 1.1. Although the two machines have the same 4-pole, the machine adopting distributed windings has more slots [1]. Compared with concentrated windings, each coil in distributed windings spans more slots. As a result, distributed windings have longer coil endings. Machines adopting concentrated windings have problems such as lower utilization of magnetic flux generated by permanent magnets (PMs), a decrease in reluctance torque, and an increase in iron loss by harmonics of magnetic flux. However, because of the shorter coil windings, concentrated windings can cut manufacturing costs by reducing the usage of copper, and at the same time, the limited space effectively can be effectively used.

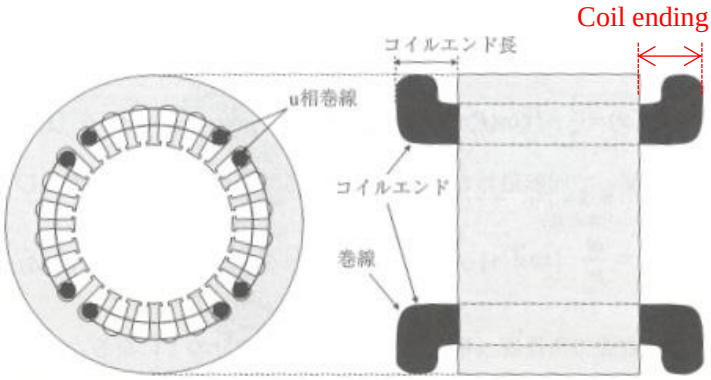


(a) Distributed windings

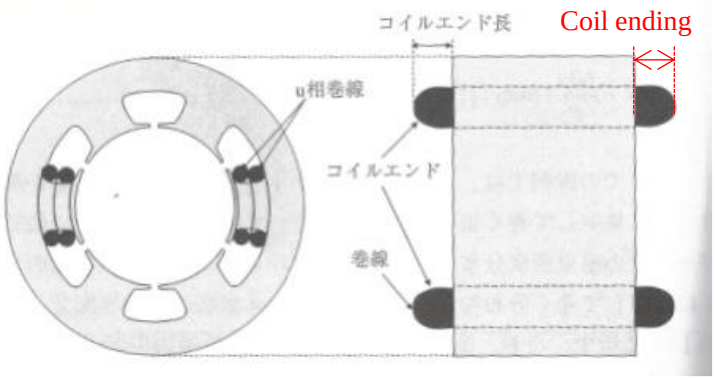


(b) Concentrated windings

Figure 1.1. Distributed and concentrated windings (4-pole machine)

Reference [1]: P. 16「省エネモータの原理と設計法」(森本 茂雄・真田 雅之著)

Fig. 1.2 shows the appearance of distributed and concentrated windings. It is obvious that concentrated windings have a shorter coil ending. As mentioned above, concentrated windings are adopted for the two topics in this paper to cut manufacturing costs.

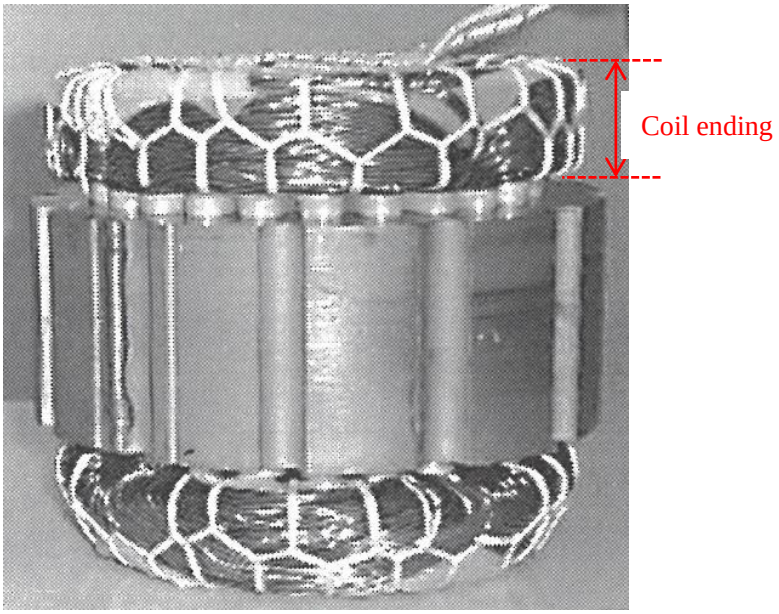


(a) Distributed windings

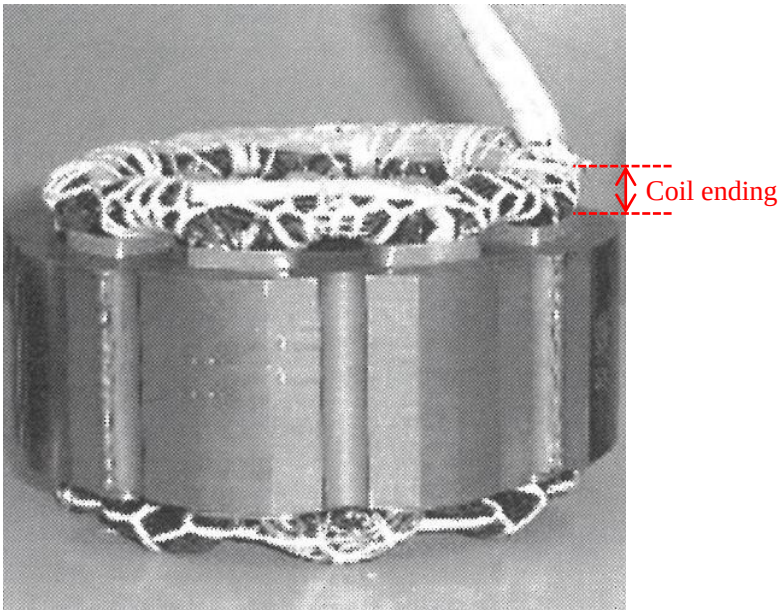


(b) Concentrated windings

Figure 1.2. Appearance of distributed and concentrated windings

Reference [1]: P. 142「省エネモータの原理と設計法」(森本 茂雄・真田 雅之著)

## Section 1.3 *Dq* transform and basic vector diagram in an IPMSM

Fig. 1.3 shows the IPMSM equivalent model in *dq* coordinate system. By using *dq* transform, the model of an IPMSM can be transformed from a stationary coordinate system to a *dq* rotating coordinate system. The direction of the *d*-axis is the maximum direction of the magnetic flux generated by the permanent magnet (PM). While the *q*-axis is a direction that makes an electrical angle of 90 deg. to the *d*-axis.

$R_a$ [Ω]: Equivalent resistance

$L_d$ [H]: *d*-axis inductance

$L_q$ [H]: *q*-axis inductance

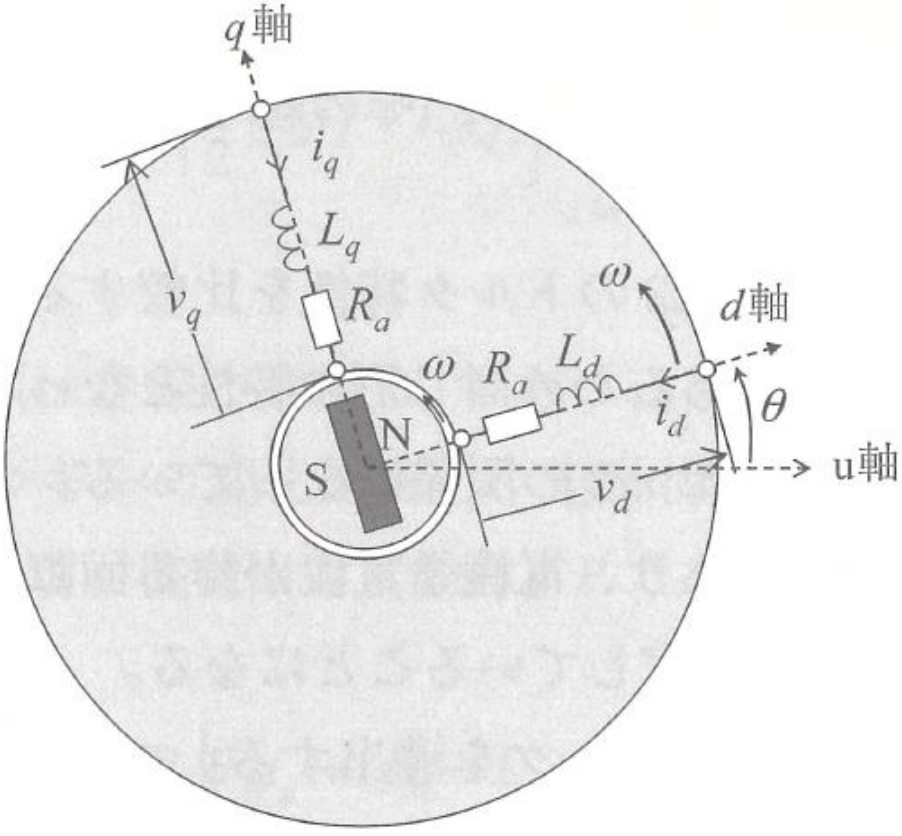


Figure 1.3. IPMSM equivalent model in *dq* coordinate system

Reference [1]: P. 47「省エネモータの原理と設計法」(森本 茂雄・真田 雅之著)

Fig. 1.4 shows the vector diagram of an IPMSM.

$\Psi_a$ [Wb]: Magnetic flux generated by PM

$i_d$ [A]: Operating current

$i_d$ [A]: $d$-axis current

$i_q$ [A]: $q$-axis current

$\Psi$ [Wb]: Total magnetic flux in an IPMSM

$L_d i_d$ [Wb]: Magnetic flux generated by $d$-axis armature reaction

$L_q i_q$ [Wb]: Magnetic flux generated by $q$-axis armature reaction, and.

As a result, the magnitude of $d$-axis magnetic flux $\Psi_d$ can be calculated by $\Psi_a i_q$ - $L_d i_d$, while the magnitude of $q$-axis magnetic flux $\Psi_q$ is $L_q i_q$. When the load current is small, the magnetic flux $\Psi$ can be regarded to be completely generated by PM magnetic flux $\Psi_a$. And the increase of load current and its phase angle $\beta$ generally leads to an increase in $q$-axis magnetic flux $\Psi_q$ and a decrease in $d$-axis magnetic flux $\Psi_d$.

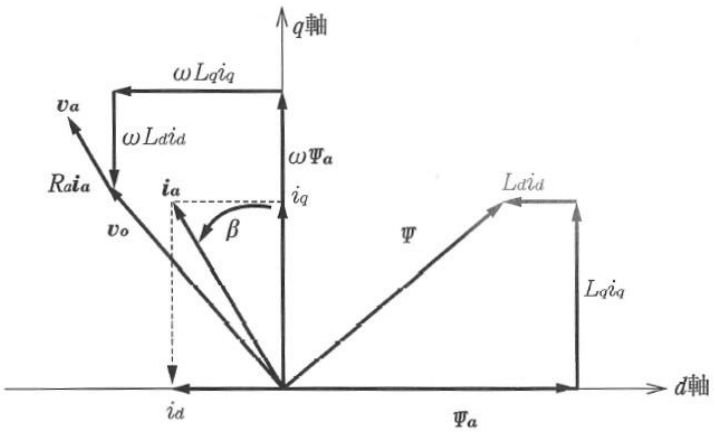


Figure 1.4. Vector diagram of an IPMSM

The torque of an IPMSM can be calculated by the following formula:

$$T = P_n\{\psi_a i_q + (L_d - L_q) i_d i_q\} \quad (1.1)$$

Where $P_n$ is the number of pole pairs. The torque of an IPMSM can be divided into magnetic torque and reluctance torque. $P_n \Psi_a i_q$ is the component of magnetic torque, while $P_n(L_d$ - $L_q) i_d i_q$ is the component of reluctance torque. It can be seen from Fig. 1.3 that because there are PMs on $d$-axis magnetic flux path and the magnetic permeability of PM is almost the same as that of air, $L_d$ is smaller than $L_q$. In general, both $L_d$ - $L_q$ and $i_d$ are negative to generate torque effectively. As a result, a decrease in $L_q$ will lead to a decrease in reluctance torque.

## Section 1.2 Losses in an IPMSM

Only copper and iron losses are examined in this paper because they account for the majority of losses in an IPMSM. The formulas are given below.

Copper loss can be calculated by the following formula:

$$P_{copper} = I_{operating}^2 \times R \tag{1.2}$$

$P_{copper}$ [W]: Copper loss

$I_{operating}$ [Arms]: Operating current

$R$ [Ω]: Resistance

According to the formula, copper loss is proportional to the square of operating current if the resistance $R$ does not change. At the same time, formular 1.1 demonstrated that operating current is related to torque.

Iron loss can be calculated by the following formula:

$$P_{iron} = P_{hysteresis} + P_{eddy} \tag{1.3}$$

$$P_{hysteresis} = m_{core} k_h f B_{max}^{1.6\sim2} \tag{1.4}$$

$$P_{eddy} = m_{core} k_e (f B_{max})^2 \tag{1.5}$$

$P_{iron}$ [W]: Iron loss

$P_{hysteresis}$ [W]: Hysteresis loss

$P_{eddy}$ [W]: Eddy current loss

$m_{core}$ [kg]: Weight of ferromagnetic material

$k_h$, $k_e$: Constants determined by ferromagnetic materials

$f$ [Hz]: Drive frequency

$B_{max}$ [T]: Maximum magnetic flux density

With other parameters unchanged, it can be seen that iron loss is related to drive frequency and maximum magnetic flux density.

# Chapter 2. Topic I: Novel Rotor Structure Employing Large Flux Barrier and Disproportional Airgap for Enhancing Efficiency of IPMSM Adopting Concentrated Winding Structure

## Section 2.1 Introduction of Topic I

Interior permanent magnet synchronous motors (IPMSMs) have been widely used in industrial applications for their outstanding characteristics, such as simple structure, high power density, wide speed range, and good speed control, especially for their high efficiency [5]-[11]. Moreover, because industrial applications are generally cost-sensitive, concentrated winding structure has been widely adopted to cut manufacturing costs and use limited space effectively [12]-[15]. At the same time, to reduce operating costs, it is also an important issue to enhance the efficiency of an IPMSM as much as possible while maintaining manufacturing costs, which is the main purpose of this chapter.

In general, an IPMSM used for an industrial application always operates in a specific operating area according to the required load. And to enhance efficiency effectively, IPMSMs should be designed suitably depending on their target operating areas. This chapter particularly concerned with efficiency in the wide-speed middle-torque operating area. Fig. 2.1(a) shows the operating area and target operating line in this chapter. The target operating point line can be considered typical operating points for a motor used in an air conditioner compressor. In most cases, the operating point moves on the target operating line depending on the temperature difference between indoor and outdoor. And a maximum torque of 2.5 Nm at 7200 rpm is also required for extreme temperature differences. To facilitate further comparison, three operating points, designated as point I (2000 rpm, 1 Nm), II (4000 rpm, 1.6 Nm), and III (7200 rpm, 1.6 Nm), respectively, have been selected for this chapter.

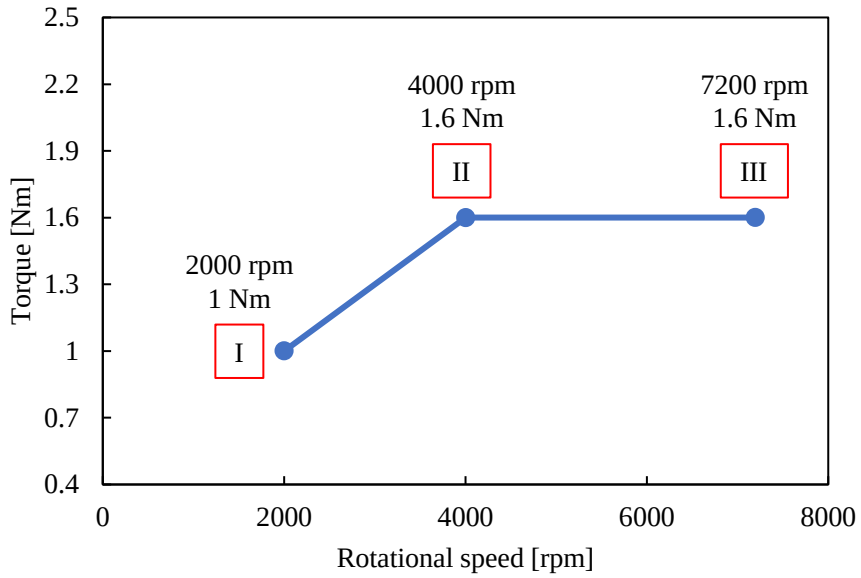


(a) Target operating area

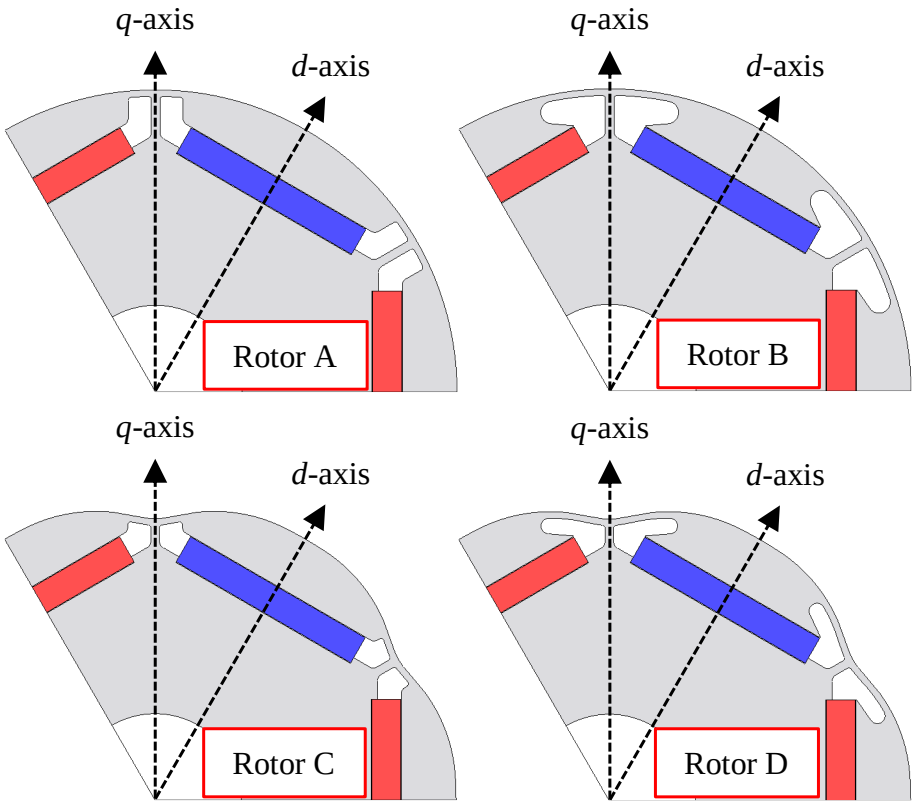


(b) A brief overview of the four rotor structures

Figure 2.1 Target operating area and a brief overview of the four rotor structures discussed in this paper

Reducing losses is the key to enhancing efficiency. The major losses of an IPMSM can be divided into copper and iron losses without considering mechanical loss. Moreover, because the magnetoresistance of air is much larger than that of ferromagnetic material, the magnetic flux path of an IPMSM can be changed by changing the shape of flux barriers and its airgap, which can affect losses significantly. In previous studies, the torque can be increased by changing the shape of flux barriers, which are mentioned in [16]-[18]. Additionally, all these studies show that an appropriate flux barrier design can reduce torque ripple. And the effect of asymmetry flux barriers examples on torque and its ripple is also discussed in [16] and [18]. Moreover, in [19], the magnetic flux leakage in the rotor iron bridges is eliminated with a rotor employing novel non-magnetic wedges. By adopting this structure, torque can also be increased because the non-magnetic wedges have a similar effect to flux barriers. At the same time, adopting a disproportional airgap can reduce the harmonic components and make the magnetic field distribution in the airgap closer to a sine wave. The study [20] uses a rotor with a disproportional airgap that shows core losses and torque ripple can be reduced while the torque decreases, and dynamic stability has also been enhanced. Similarly, in [21], cogging torque is reduced by adopting a disproportional airgap. However, contrary in study [20], the torque in this study increases. The previous studies have mentioned rotor structures with large flux barriers and disproportional airgaps, and these studies also demonstrate that both the two rotor structures can change average torque and suppress torque ripple depending on their shape. However, their advantages from the standpoint of enhancing efficiency compared with other rotor structures have not been illustrated in detail. Moreover, the efficiency of the wide-speed middle-torque operating area shown in Fig. 2.1(a) has been scarcely investigated. Therefore, this chapter has two purposes. The first purpose is to propose a novel rotor structure which can enhance efficiency at the target wide-speed middle-torque operating area without additional manufacturing costs. The second purpose is to clarify the design method for a suitable rotor structure depending on its target operating area.

For easy understanding, Fig. 2.1(b) provides a brief overview of the four rotor structures discussed in this chapter. And the stator structure has not been changed in this chapter. Rotor A, which has minimum flux barriers on $q$-axis magnetic flux path, is the basic rotor structure in this chapter. Rotor B adopts large flux barriers on $q$-axis magnetic flux which can concentrate the magnetic flux of permanent magnets (PMs) on $d$-axis while suppressing $q$-axis magnetic flux. Rotor C adopts a disproportional airgap on $q$-axis magnetic flux path which can suppress q-axis magnetic flux and $dq$-axis harmonic magnetic flux. Rotor D is the proposed rotor structure in this chapter, which employs both large flux barriers and a disproportional airgap to take advantage of both Rotors B and C.

This chapter first examines the effects of adopting large flux barriers and a disproportional airgap on the utilization ratio of magnetic flux generated by PMs, the dimension of $q$-axis magnetic flux path, and the proportion of harmonic iron loss components, before examining their effects on copper and iron losses. 2D-FEM (Finite-Element Method) is used for discussion first. And 2D-FEM results show that the efficiency of Rotor B is higher than that of Rotor C at operating point II because the copper loss of Rotor B is reduced effectively. While the efficiency of Rotor C is higher than that of Rotor B at operating point III because the iron loss of Rotor C is reduced effectively. For the target operating line, either copper or iron losses should be reduced because neither copper nor iron losses are dominant. Therefore, Rotor D is proposed to achieve the most efficient model on the target operating area by taking advantage of both Rotors B and C and realized a tradeoff between copper and iron losses to minimize total loss.

A prototype machine is manufactured to verify the 2D-FEM results. Both 2D-FEM and experimental results show that the proposed rotor structure, which employs both large flux barriers and a disproportional airgap, can enhance the efficiency of an IPMSM most effectively at the target operating area. Moreover, for a low-speed high-torque operating area, adopting only large flux barriers is most suitable. And for a high-speed low-torque operating area, adopting only a disproportional airgap is most suitable.

The structure of this chapter is as follows. Section 2.2 proposes the structure of the basic model. The advantages of the rotor adopting large flux barriers and the rotor adopting a disproportional airgap are illuminated in Section 2.3 and 2.4, respectively. In Section 2.5, a novel rotor structure employing both large flux barriers and a disproportional airgap has been proposed to take advantage of the two rotor structures mentioned above. Finally, experimental verification is shown in Section 2.6.

In addition, the copper and iron losses can be changed by changing the load current and its phase angle to minimize total loss. And this control strategy is called maximum efficiency control for an IPMSM. Unless otherwise specified, the maximum efficiency control strategy is used throughout this paper. Moreover, 2D-FEA is executed by using an electromagnetic field simulator (JMAG-designer ver. 20.0, JSOL Co., Ltd.).

## Section 2.2 Basic structure of IPMSM in Topic I

The design specification for the IPMSM in this chapter are shown in Table 2.1. The stator core outer diameter is 90 mm, and the stacked length is 48 mm. The magnet weight is 61.29 g. It should be noted that the weight and shape of the magnets used for rotors have not been changed in this chapter to avoid increasing manufacturing costs. As mentioned in the previous chapter, concentrated winding structure has been used to cut manufacturing costs. Therefore, to achieve high efficiency, a 6-pole/9-slot combination has been adopted, which ensures that the inverter's maximum drive frequency is less than or equal to 400 Hz at 7200 rpm while considering the balance of copper and iron losses at the target operating line. [15]-[16].

Fig. 2.2 shows the stator and the rotor structure of the basic model, respectively. To evaluate the difference in efficiency performance of IPMSMs caused by different rotor structures, as shown in Fig. 2.2(a), the stator structure has not been changed in this chapter. Fig. 2.2(b) shows the rotor structure of the basic model, and this basic model is called Model A. The manufacturing costs and difficulty of Model A are determined by an IPMSM used for a mass-produced air-conditioner compressor. There are minimum flux barriers on *q*-axis magnetic flux path which can ensure that no magnetic flux short circuits in the rotor core. As a result, this rotor structure can generate reluctance torque easily for its wide *q*-axis magnetic flux path. Moreover, only the one-third models of the stator and rotor are shown in Fig. 2.2. The full model can be regarded as a repetition of three one-third models. As a result, the magnetic forces generated in the radial direction can be cancelled and no unbalanced magnetic force generates in the 6-pole/9-slot combination [21]-[23].

Table 2.1. Design specification of Chapter I

| Design specification | |
|---|---|
| Stator core outer diameter [mm] | 90 |
| Stator core inner diameter [mm] | 43 |
| Airgap length [mm] | 0.6 |
| Stacked length [mm] | 48 |
| Magnet weight [g] | 61.29 |
| Slots number | 9 |
| Poles number | 6 |

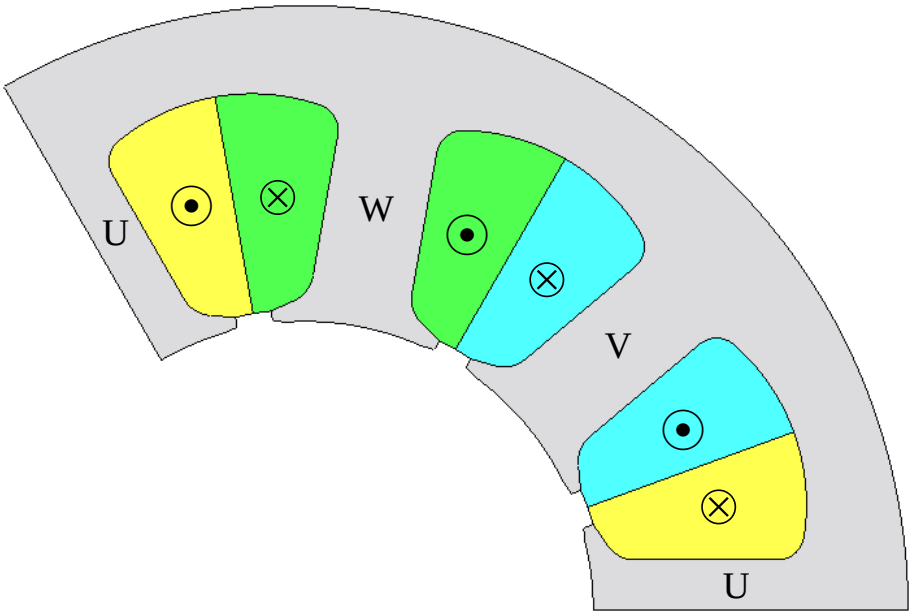


(a) Stator structure

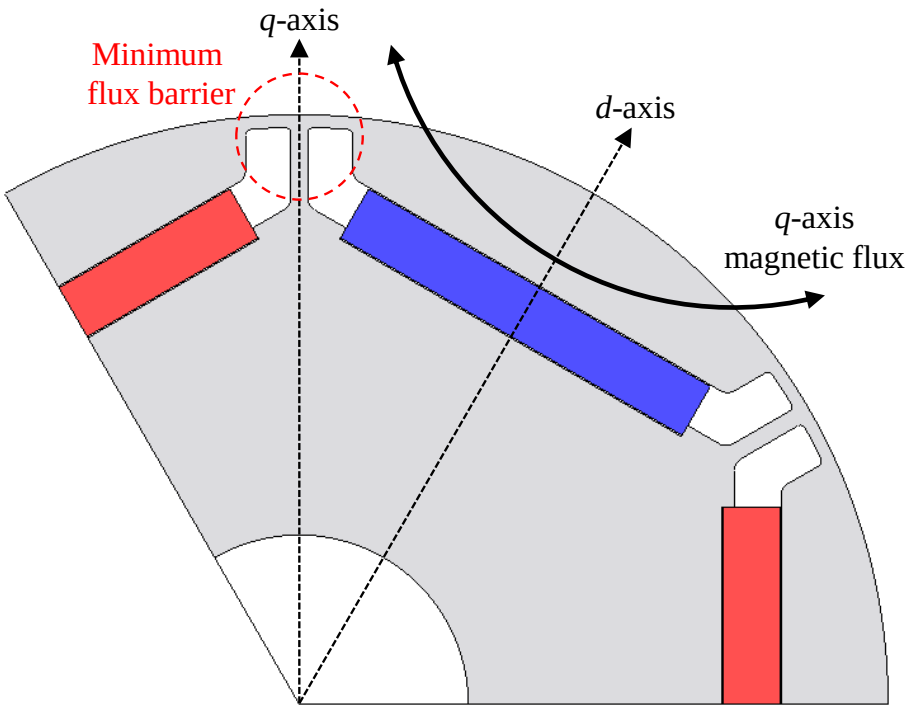


(b) Rotor structure

Fig. 2.2 Stator and rotor structures of basic model

## Section 2.3 Investigation of rotor structure which focuses on minimizing copper loss

Fig. 2.3 shows the rotor structure and its sketch for Model B, respectively. As shown in Fig. 2.3(a), compared with Model A, there are large flux barrier on *q*-axis magnetic flux path to concentrate the magnetic flux of PMs on *d*-axis while suppressing *q*-axis magnetic flux. In other words, the characteristic of Model B is that it can generate a larger PM magnetic flux density in airgap. As a result, Model B is a rotor structure which can generate magnetic torque easier. Moreover, the differences of Model B from Model A are marked by the blue lines in Fig. 2.3(b). The one-side opening angle of Model A is approximately 24 deg. To evaluate the influence of the opening angular on copper loss, angle $a$ is defined as the relative opening angle between Models A and B.

Fig. 2.4 shows the observation point of PM magnetic flux density in the airgap. To eliminate the influence of stator slots, there are no slots in the stator. At the observation point indicated by the red dot located in center of the airgap, PM magnetic flux density ($B_r$) in radial direction is observed with the variation of mechanical angle $\theta$.

Fig. 2.5 shows the magnetic flux density waveforms and their fundamental waveforms of Models A and B ($a$ = 8 deg.) observed in the airgap. The waveform of Model A is close to a rectangular wave. Compared with Model A, PM magnetic flux density has been concentrated on the *d*-axis in Model B ($a$ = 8 deg.) by the large flux barriers. As a result, the fundamental wave amplitude of magnetic flux density in Model B ($a$ = 8 deg.) is 0.820 T, which is 13.32% larger than the 0.724 T in Model A. Moreover, Model B has a total harmonic distortion (THD) of 16.81%, which is lower than the 29.44% in Model A for the fundamental wave of magnetic flux density. In general, only the fundamental component of the magnetic flux density wave contributes to magnetic torque, while the harmonic components only increase iron loss.

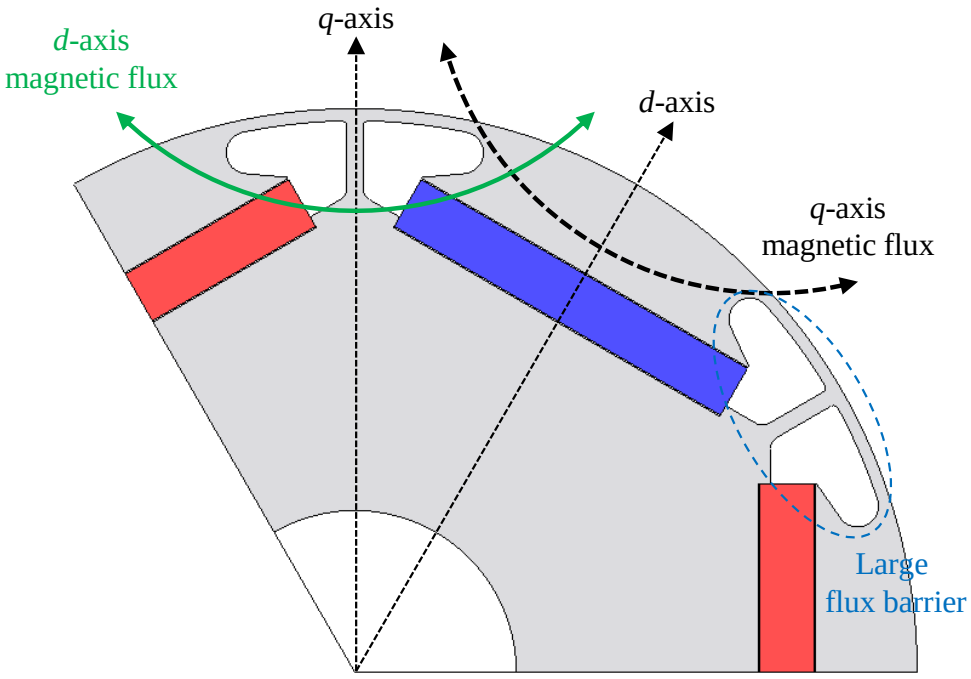


(a) Rotor structure of Model B

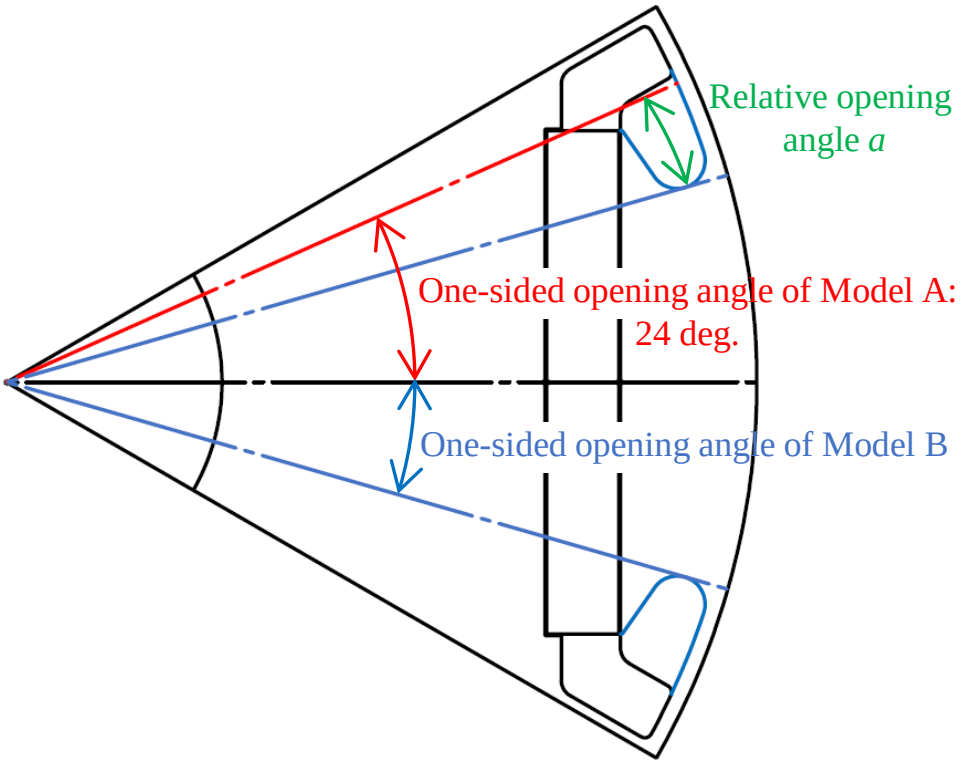


(b) Sketch of Model B

Fig. 2.3 Rotor structure and its sketch for Model B

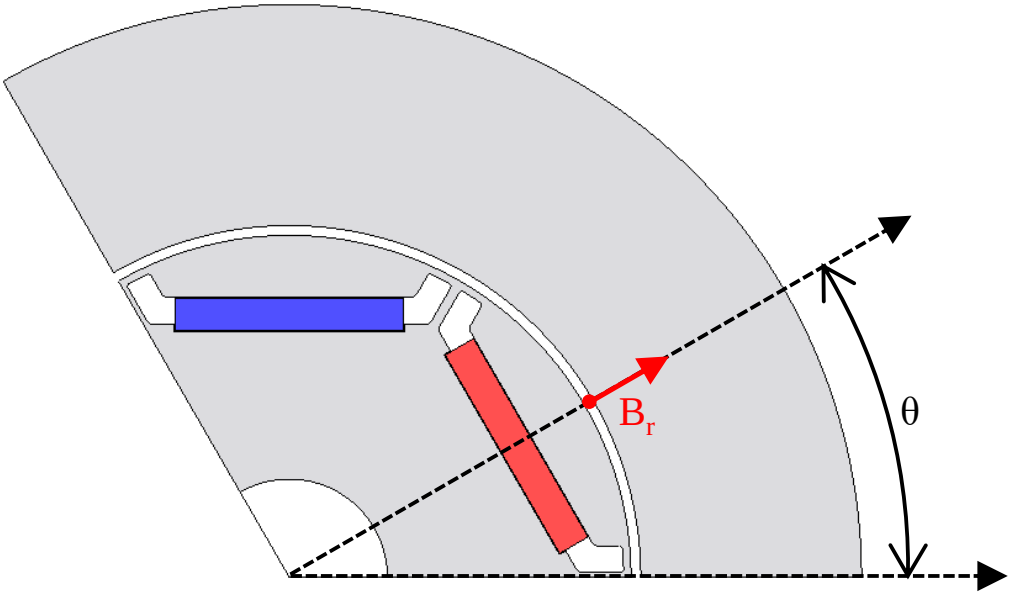


Figure 2.4. Observation point of PM magnetic flux density in the airgap

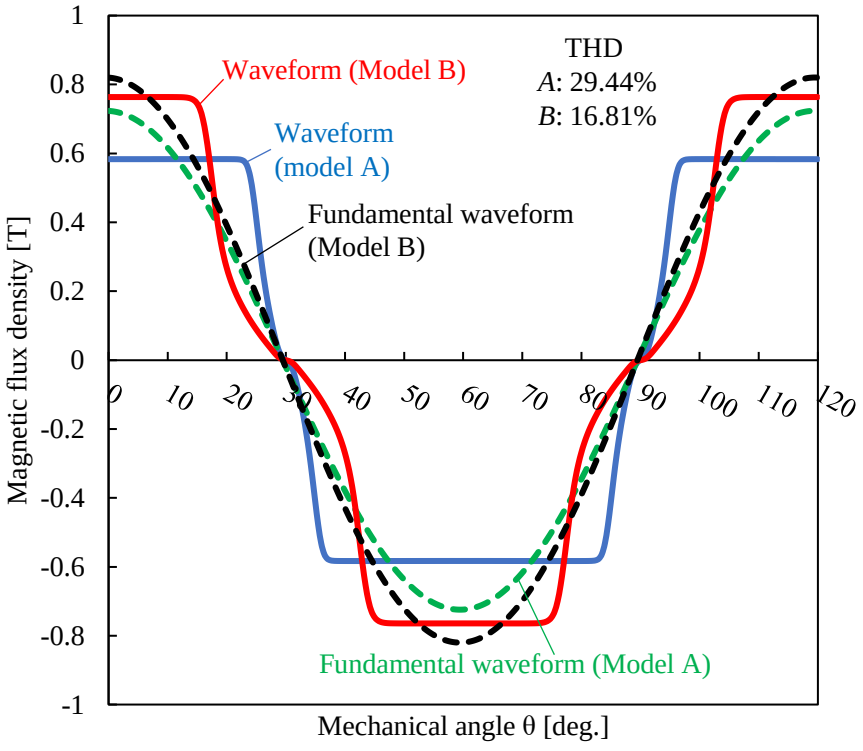


Figure 2.5 Magnetic flux density and their fundamental waveforms observed in the airgap

To determine the most optimum angle *a*, Fig. 2.6 shows the fundamental wave amplitude of magnetic flux density observed in the airgap with the variation of angle *a*. As shown in the figure, when the angle *a* is less than or equal to 8 deg., the PM magnetic flux density is gradually concentrated by the large flux barriers with the increase of angle *a*. Therefore, the fundamental wave amplitude increases as angle *a* increases. However, when angle *a* is greater than or equal to 10 deg., the fundamental wave amplitude decreases as angle *a* increases due to the magnetic saturation between the flux barriers. Moreover, the fundamental wave amplitudes at $a = 8$ deg. and $a = 10$ deg. are very similar. Furthermore, the torque of an IPMSM can be divided into magnetic torque and reluctance torque. Although the large flux barriers can increase the fundamental wave amplitude of magnetic flux density (which is also referred to as PM magnetic flux density for brevity), the *q*-axis magnetic flux path will be narrow at the same time. Fig. 2.7 shows the magnitudes of magnetic torque and reluctance torque with the variation of angle *a*. In this figure, a maximum torque control strategy has been adopted to generate the maximum torque while maintaining the same load current for all angles *a*. Model A has a torque of 1.6 Nm at 4000 rpm, with its reluctance torque being the largest and the magnetic torque being the smallest. As angle *a* increases, the *q*-axis magnetic flux path gradually becomes narrower. As a result, as angle *a* increases, the *q*-axis inductance ($L_q$) decreases, which causes the reluctance torque to decrease. Moreover, the magnitude of magnetic torque shown in Fig. 2.7 shows the same changing trends as the fundamental wave amplitude shown in Fig. 2.6. The magnetic torque has a maximum magnitude at either $a = 8$ deg. or $a = 10$ deg., which is 1.68 Nm. Considering the magnitude of the reluctance torque, the torque reaches a maximum magnitude at either $a = 6$ deg. or $a = 8$ deg.

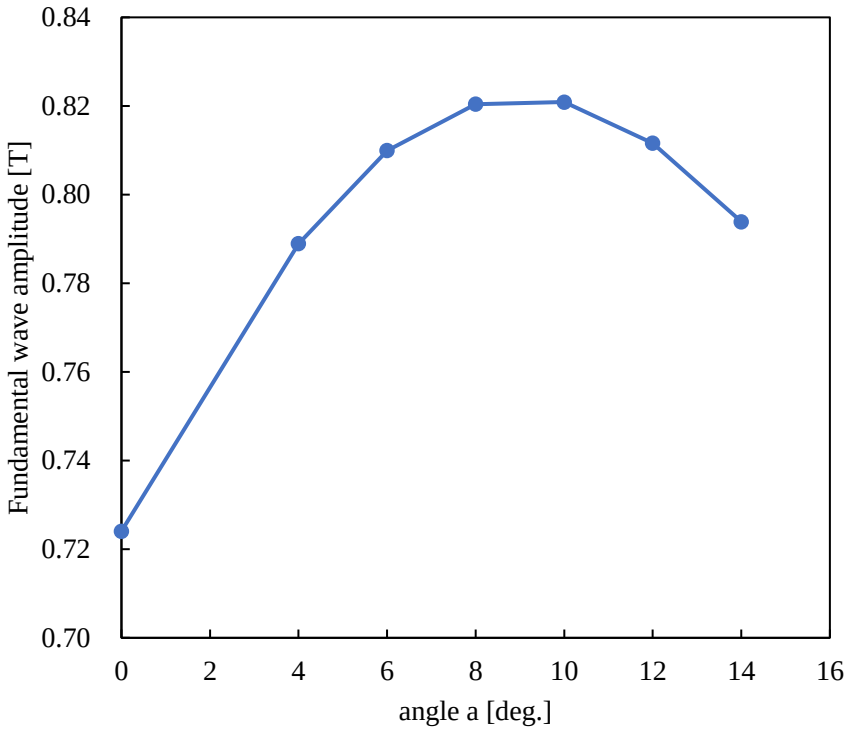


Figure 2.6. Fundamental wave amplitude of magnetic flux density observed in the airgap with the variation of angle a

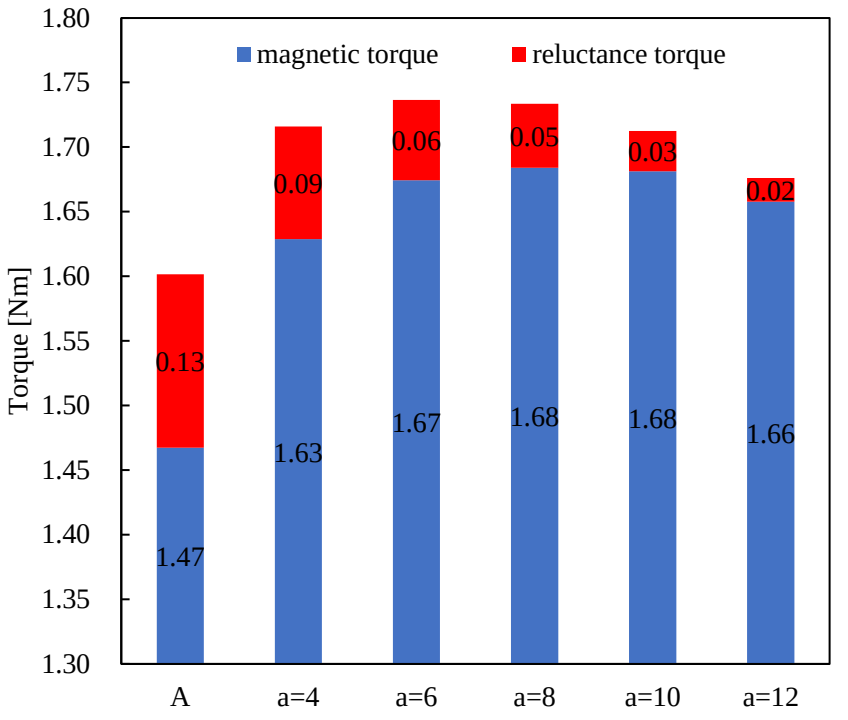


Figure 2.7. Magnitudes of magnetic torque and reluctance torque with the variation of angle *a*

Fig. 2.8 shows copper loss and efficiency with the variation of angle *a* at operating point II. When angle *a* is less than or equal to 8 deg., the copper loss decreases as angle *a* increases because the magnetic torque increases. However, when angle *a* is greater than or equal to 8 deg., the copper loss increases as angle *a* increases because the magnetic torque does not increase while the reluctance torque decreases. When *a* = 8 deg., the efficiency reaches a maximum value at operating point II, which is 93.49%. Therefore, the model whose relative opening angle *a* = 8 deg. is chosen for Model B.

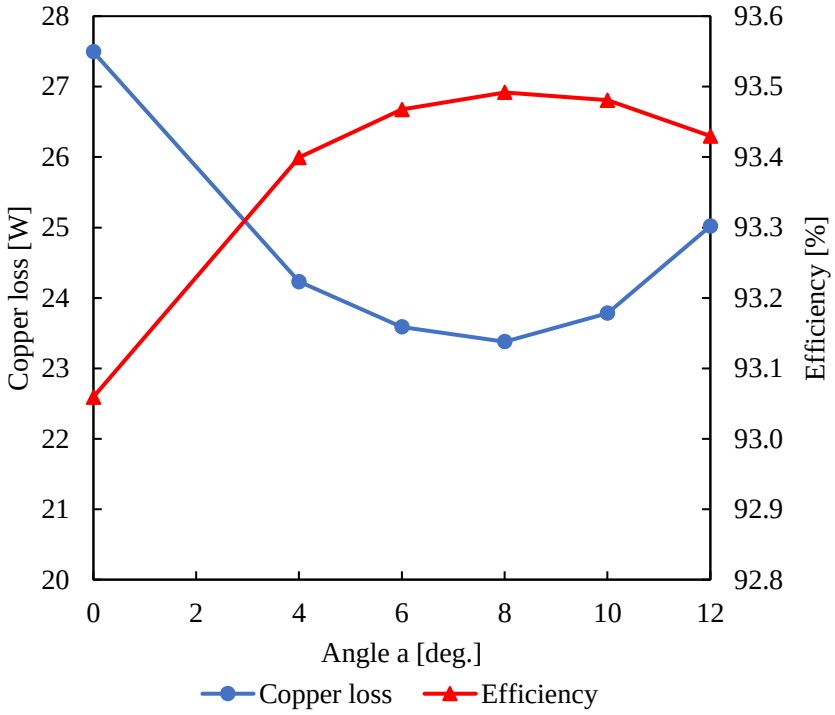


Figure 2.8. Copper loss and efficiency at operating point II

Fig. 2.9 shows the efficiency difference map obtained by subtracting the efficiency of Model A from that of Model B ($\eta_B - \eta_A$). Over the entire target operating line, Model B is more efficient than Model A. Especially at operating point II, the copper loss of Model B is 23.38 W, which is 14.97% lower than the 27.50 W in Model A. As a result, the efficiency of Model B is 93.49%, which is 0.43% higher than the 93.06% in Model A. Moreover, the top-left side of the figure is a low-speed high-torque operating area while the bottom-right side is a high-speed low-torque operating area. Because copper loss is dominant in the low-speed high-torque operating area, the efficiency of Model B has been significantly enhanced. However, the efficiency of Model B is lower than that of Model A in the high-speed low-torque operating area.

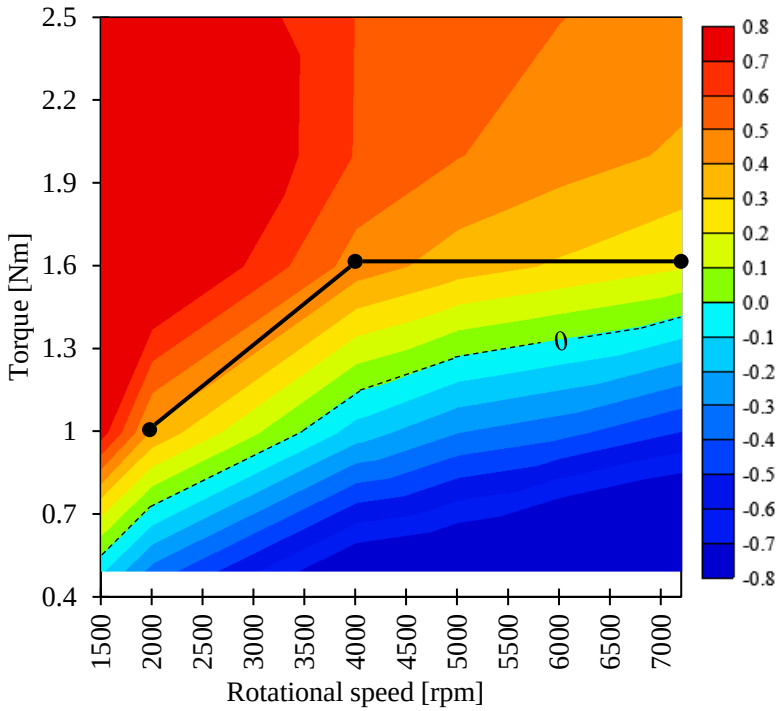


Figure 2.9 Efficiency difference map obtained by $\eta_B$ - $\eta_A$

To clarify the reason why the efficiency of Model B is lower than that of Model A at the high-speed low-torque operating area, Fig. 2.10 shows losses with the variation of torque at 7200 rpm. Because the magnetic torque in Model B has been utilized effectively, as can be seen from Fig. 2.10(a), the copper loss of Model B is smaller than that of Model A throughout the entire operating line of 7200 rpm. The iron and total losses with the variation of torque at 7200 rpm are shown in Fig. 2.10(b). Iron losses do not change as drastically as copper losses because the torque increases while the rotational speed remains at 7200 rpm. Moreover, the iron loss of Model B is larger than that of Model A at the low-torque operating area, but smaller than that of Model A at the high-torque operating area. As a result, although the copper loss of Model B is smaller than that of Model A throughout the entire operating line of 7200 rpm, considering the iron loss, the total loss of Model B is larger than that of Model A at the low-torque operating area, but smaller than that of Model A at the high-torque operating area.

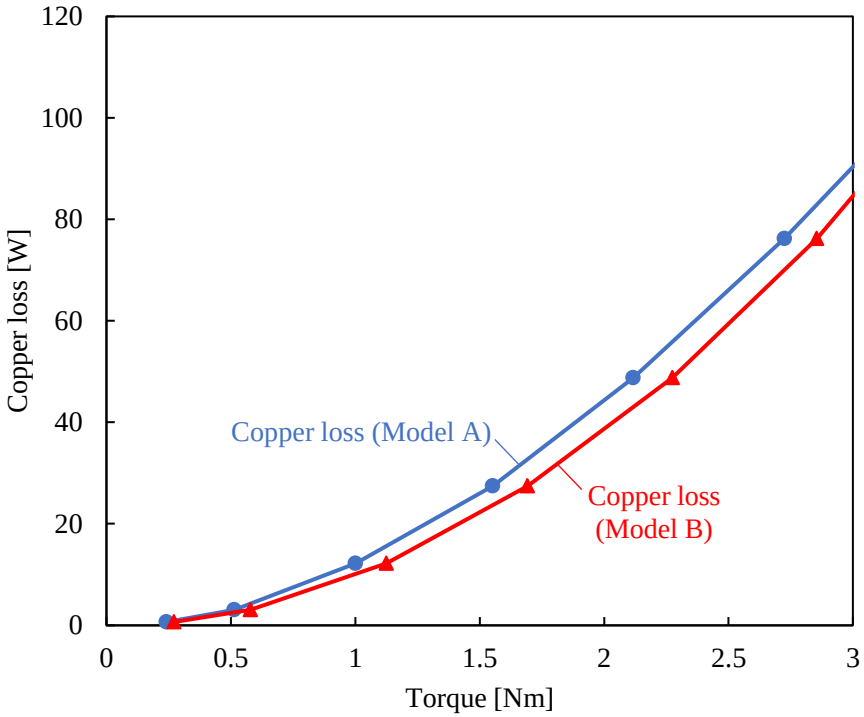


(a) Copper loss

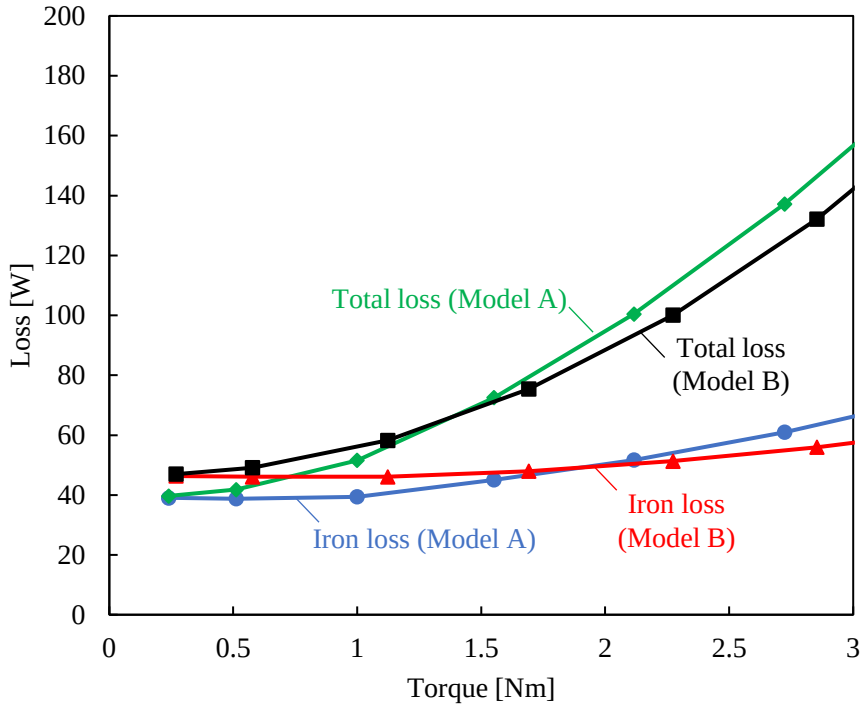


(b) Iron and total losses

Fig. 2.10 Losses with the variation of torque at 7200 rpm

Fig. 2.10 shows the losses at load, to further disassemble iron loss, Fig. 2.11 shows the spectrum of iron loss of Models A and B at 7200 rpm and no load. The iron loss component with the same frequency as the drive frequency is referred to as the fundamental iron loss component. Therefore, if the abscissa is 1, it means that the frequency of this iron loss component is the fundamental component which has the same frequency as the drive frequency. If the abscissa is 2, it means that the frequency of this iron loss component is 2 times the drive frequency, and so on. The iron loss harmonic components of Model B are 6.82 W, which is smaller than that the 7.50 W in Model A. However, the iron loss fundamental component of Model B is larger than that of Model A, which is the reason why the iron loss of Model B is larger than that of Model A at the low-torque operating area.

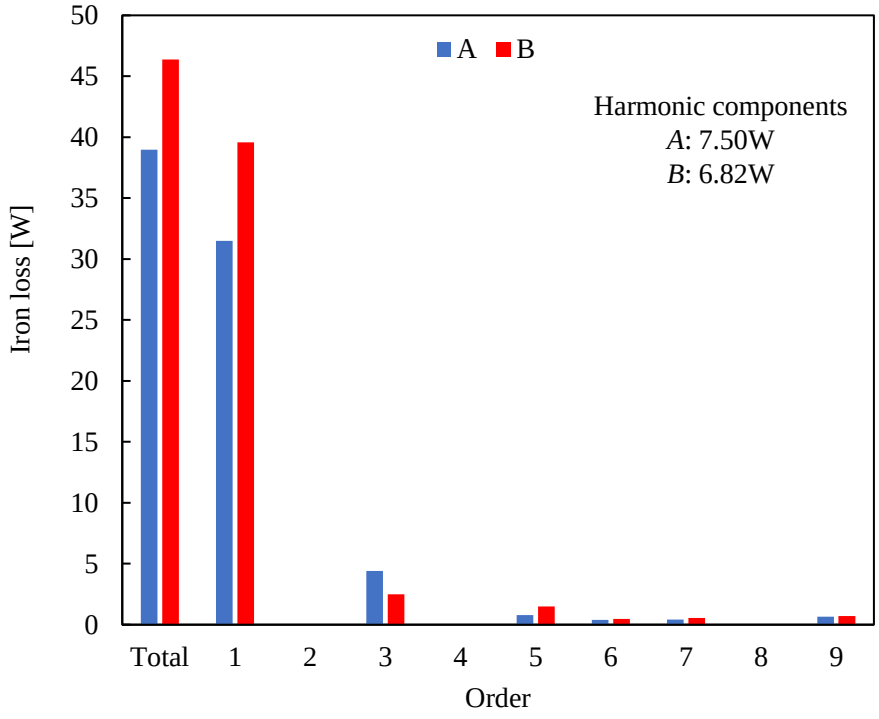


Figure 2.11. Spectrum of iron loss at 7200 rpm and no load

Fig. 2.12 shows the magnetic flux of Models A and B with the variation of torque at 7200 rpm. As shown in Fig. 2.12(a), the *d*-axis magnetic flux ($\psi_d$) of Model B is larger than that of Model A throughout the entire operating line of 7200 rpm because of its larger PM magnetic flux density. Moreover, the *q*-axis magnetic flux ($\psi_q$) of Model B is smaller than that of Model A throughout the entire operating line of 7200 rpm because of its narrower *q*-axis magnetic flux path. The load current and its phase angle are small at the low-torque operating area. Therefore, the total magnetic flux ($\psi$) can be considered as being entirely generated by the *d*-axis magnetic flux. The total magnetic flux of Model B is larger than that of Model A because of its larger *d*-axis magnetic flux. With torque increases, the load current and its phase angle also increase. As a result, the *q*-axis magnetic flux increases while the *d*-axis magnetic flux decreases. As shown in Fig. 2.12(b), when the large *q*-axis magnetic flux of Model A is considered, the total magnetic flux of Model B becomes smaller than that of Model A at the high-torque operating area.

As mentioned above, adopting large flux barriers can reduce the copper loss of Model B on the one hand because the PM magnetic flux can be concentrated on the *d*-axis and the utilization of magnetic torque can be improved. The large PM magnetic flux density, on the other hand, also causes an increase in total magnetic flux, which increases the iron loss fundamental component, particularly at the high-speed low-torque operating area.

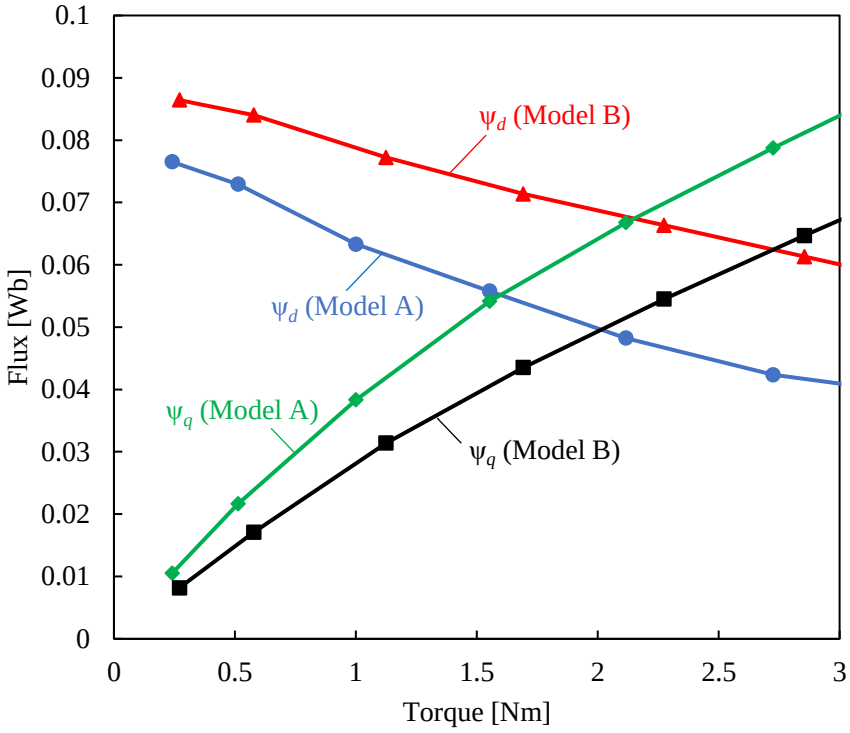


(a) $D$-axis magnetic flux $\Psi_d$ and $q$-axis magnetic flux $\Psi_q$

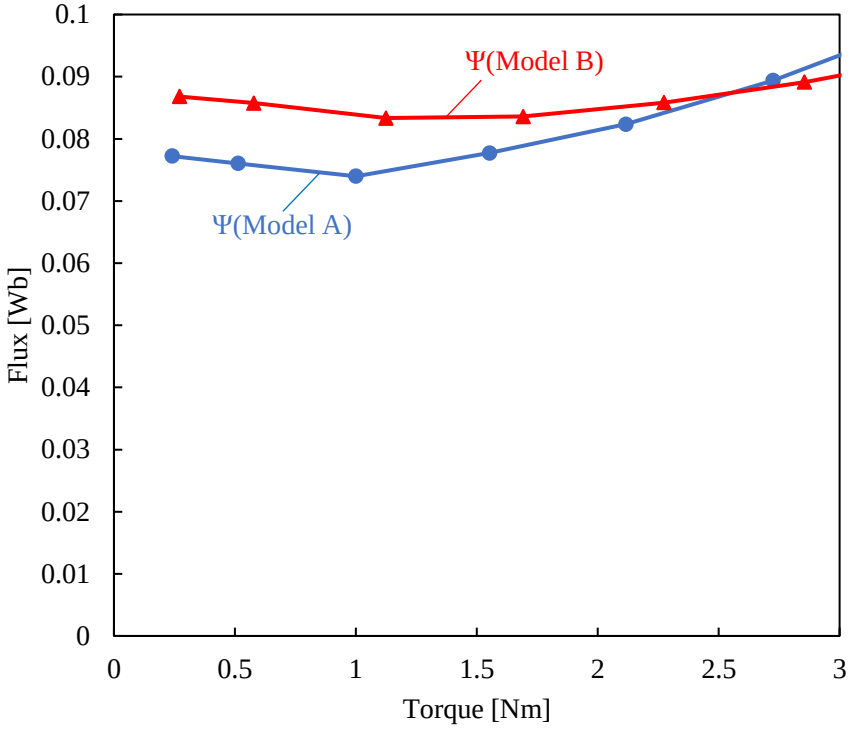


(b) Magnetic flux $\Psi$

Fig. 2.13 Magnetic flux with the variation of torque at 7200 rpm

## Section 2.4 Investigation of rotor structure which focuses on minimizing iron loss

Adopting large flux barriers has been discussed in the previous chapter to enhance efficiency by reducing copper loss. However, the large PM magnetic flux density also causes an increase in iron loss, particularly at the high-speed low-torque operating area. Considering either copper or iron losses should be reduced for the target operating line, this chapter proposes a rotor adopting a disproportional airgap to reduce iron loss by making the waveform closer to a sine wave.

As mentioned in the previous chapter, only the fundamental component of the magnetic flux density wave shown in Fig. 2.5 contributes to magnetic torque, while the harmonic components only increase iron loss. Therefore, this chapter focuses on reducing the harmonic iron components while maintaining the PM magnetic flux density unchanged.

Fig. 2.13 shows the rotor structure and its sketch for Model C, respectively. Compared with Model A, there is a disproportional airgap on $q$-axis magnetic flux path which can suppress $q$-axis magnetic flux and the harmonic components of $dq$-axis magnetic flux. Because the magnetoresistance of air is much larger than that of ferromagnetic material, a long airgap will lead to a reduction in PM magnetic flux density. Therefore, to ensure the PM magnetic flux density does not decrease, as shown in Fig. 2.13(b), a segment of the arc of Model A has been reserved. The blue arc is connected to Model A's arc, and the green line is tangent to the blue line. Length $d$ is defined as the length of the disproportional airgap.

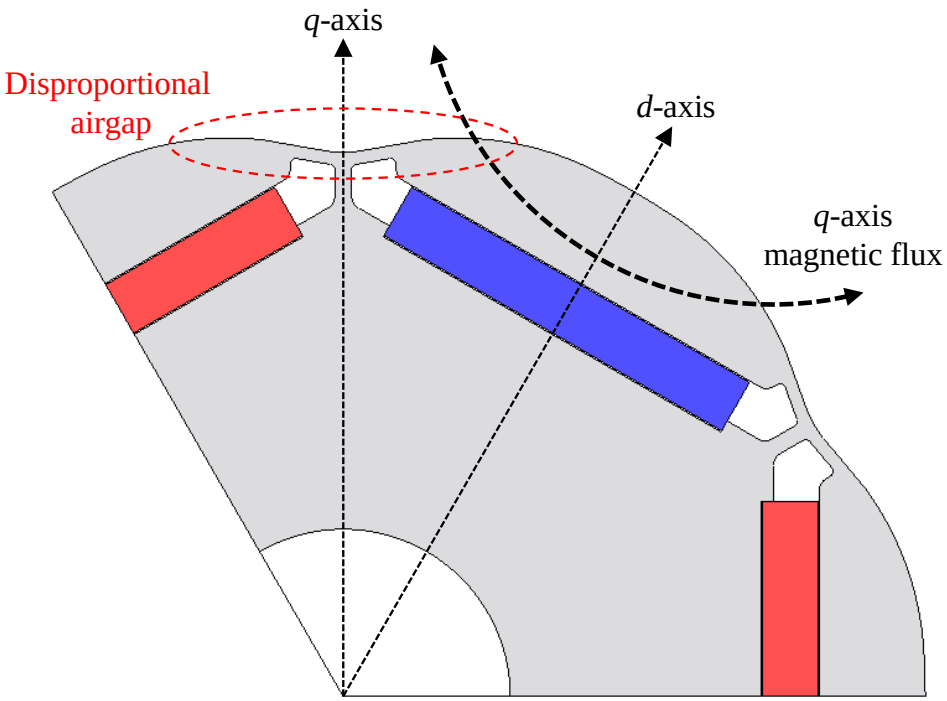


(a) Rotor structure of Model C

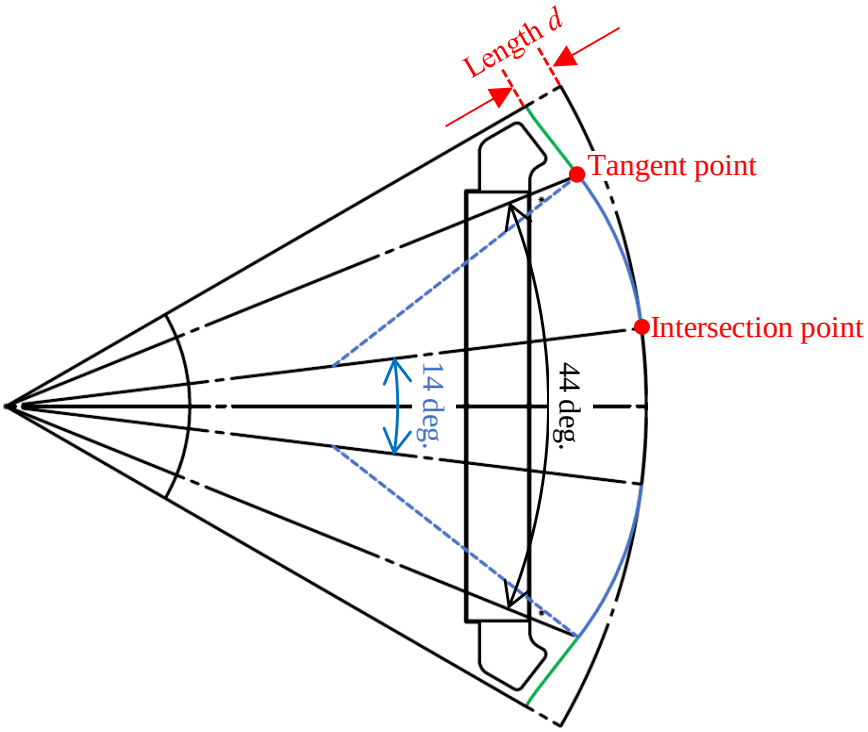


(b) Sketch of Model C

Fig. 2.13 Rotor structure and its sketch for Model C

Fig. 2.14 shows the magnetic flux density waveforms of Models A and C ($d$ = 1.3 mm) observed in the airgap. The observation method is the same as in Model B, as shown in Fig. 2.4. The waveform of Model C ($d$ = 1.3 mm) is close to a sine wave in comparison to the waveform of Model A, which is close to a rectangular wave.

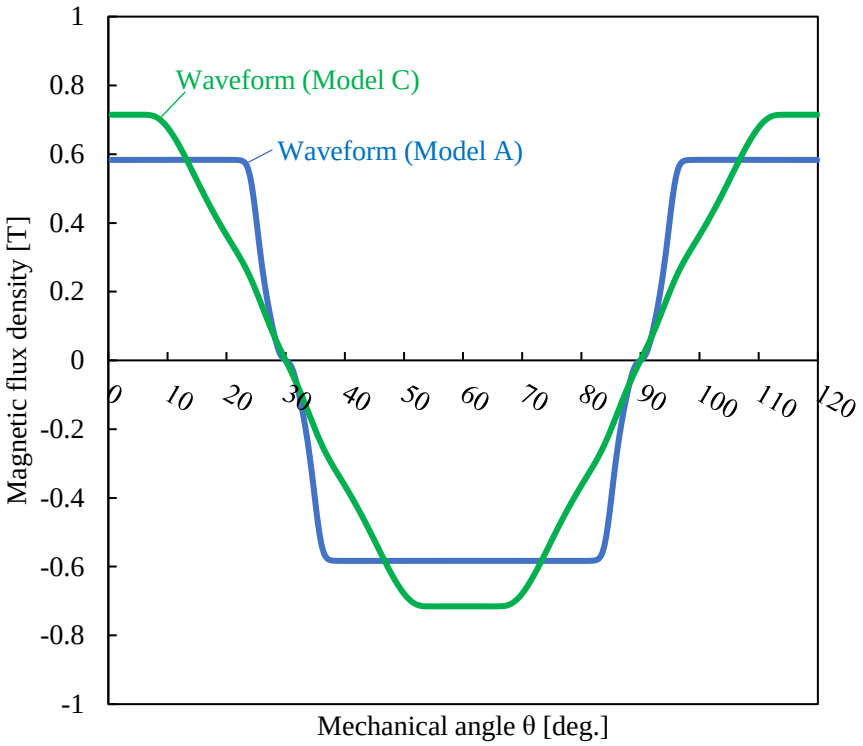


Figure 2.14. Magnetic flux density waveforms observed in the airgap

To determine the optimum disproportional airgap length $d$. Fig. 2.15 shows the fundamental wave amplitude and their THD of the magnetic flux density observed in the airgap with the variation of length $d$. The fundamental wave amplitude increases slightly with length $d$ increases. At the same time, the THD decreases first and then increases, and reaches a minimum value when $d$ = 1.3 mm. Fig. 2.16 shows the fundamental and harmonic components of iron loss with the variation of length $d$ at 7200 rpm and no load. As a result, the iron loss fundamental component increases slightly as length $d$ increases. And when length $d$ is less than or equal to 1.3 mm, the iron loss harmonic components decrease as the length $d$ increases. When length $d$ is greater than or equal to 1.3 mm, the iron loss harmonic components remain nearly unchanged. Therefore, the model whose disproportional length $d$ = 1.3mm is chosen for Model C.

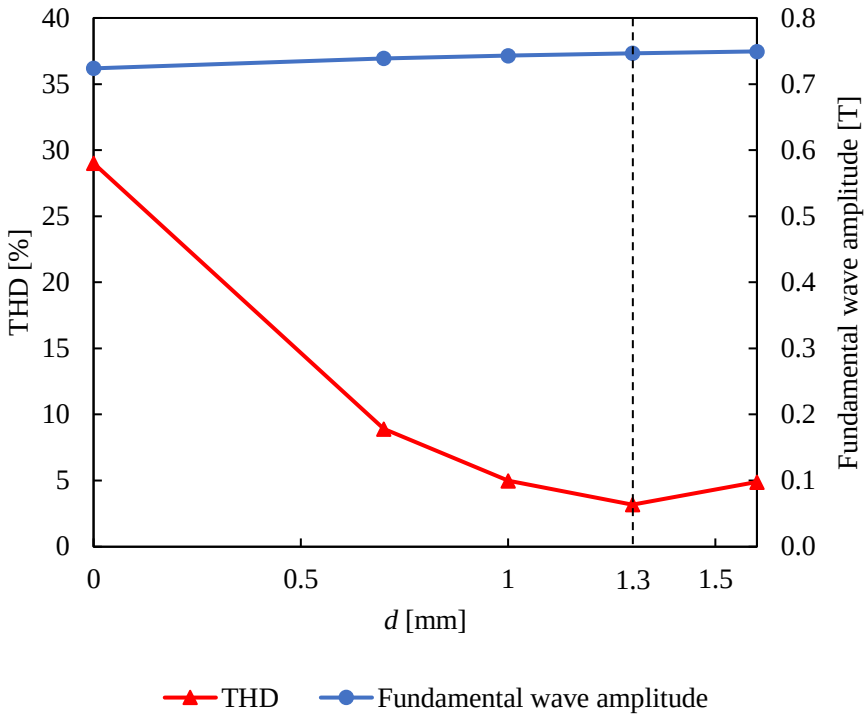


Figure 2.15. Fundamental wave amplitude and their THD of the magnetic flux density observed in the airgap with the variation of length *d*

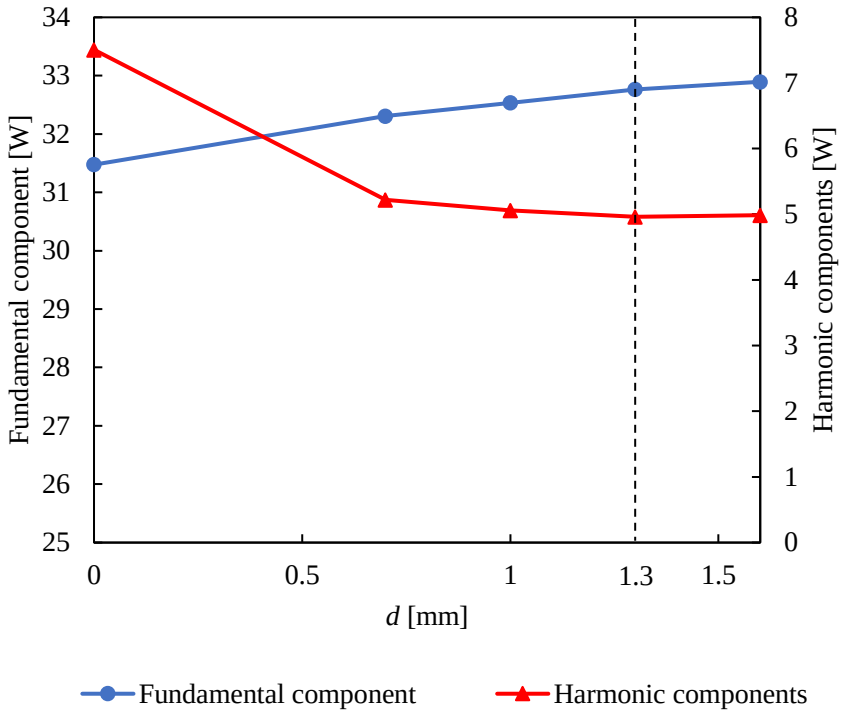


Figure 2.16. Fundamental and harmonic components of iron loss with the variation of length *d* at 7200 rpm and no load

Fig. 2.17 shows the iron loss spectrum of Models A and C at 7200 rpm and no load. The iron loss fundamental component of Model C is slightly larger than that of Model A due to its slightly larger PM magnetic flux density. However, the iron loss harmonic components of Model C decrease significantly. As a result, the iron loss of Model C is smaller than that of Model A. Moreover, Fig. 2.18 shows the $q$-axis magnetic flux waveforms of Models A and C at operating point II. Compared with Model A, the fundamental component of $q$-axis magnetic flux in Model C is 21.32% lower. As mentioned in the previous chapter, a decrease in $q$-axis magnetic flux results in a decrease in total magnetic flux, which can reduce iron loss. Furthermore, compared with Model A, Model C suppresses the 6$^{th}$ harmonic component, which can suppress the 5$^{th}$ and 7$^{th}$ iron loss.

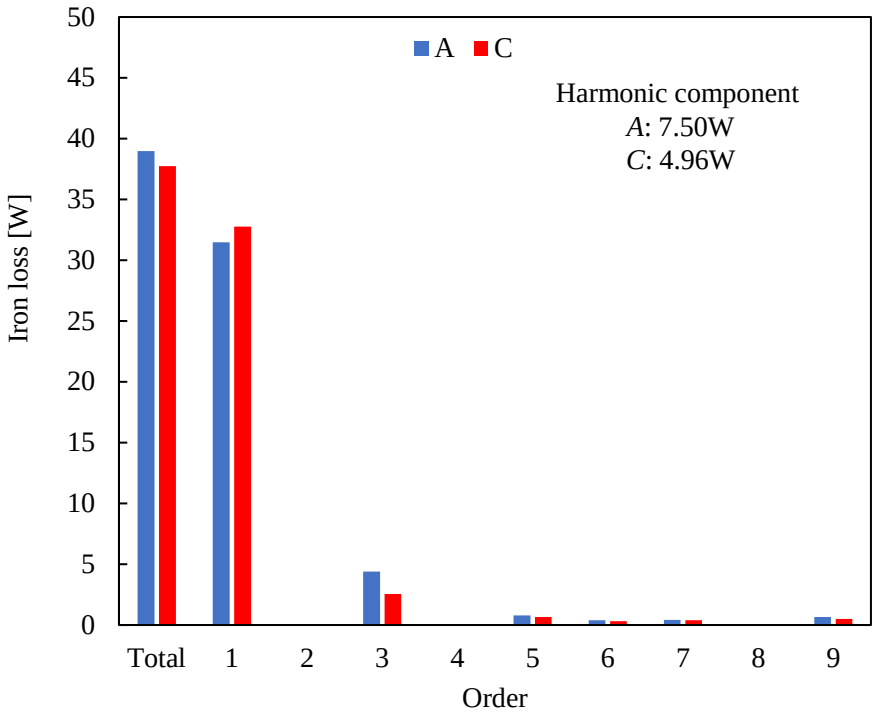


Figure 2.17. Spectrum of iron loss at 7200 rpm and no load

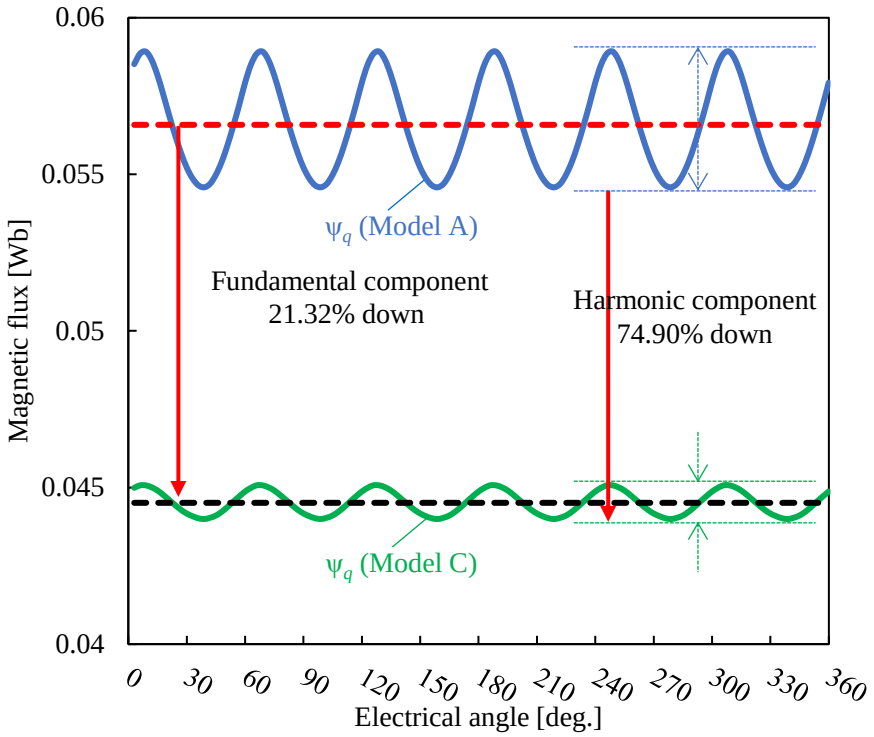


Figure 2.18. *Q*-axis magnetic flux waveforms at operating point II

Fig. 2.19 shows losses with the variation of torque at 7200 rpm. As shown in Fig. 2.19(a), the iron loss of Model C is smaller than that of Model A throughout the entire operating line of 7200 rpm. Moreover, Fig. 2.19(b) shows the total and copper losses. Same with adopting large flux barriers, the *q*-axis magnetic flux path in Model C also becomes narrower. As a result, compared with Model A, the reluctance torque of Model C is smaller at the same operating point, resulting in an increase in copper loss. Therefore, the copper loss of Model C is slightly smaller than that of Model A at the very low-torque operating area due to its slightly larger PM magnetic flux density. However, because magnetic saturation is basically nonexistent, reluctance torque increases as load current and its angle increase. As a result, because the reluctance torque of Model C is smaller at the same operating point, its copper loss increases faster than that of model A when torque increases. Considering iron loss should be emphasized at this operating line of 7200 rpm due to high rotational speed, Model C has a smaller total loss than that of Model A throughout the entire operating line of 7200 rpm because of its smaller iron loss.

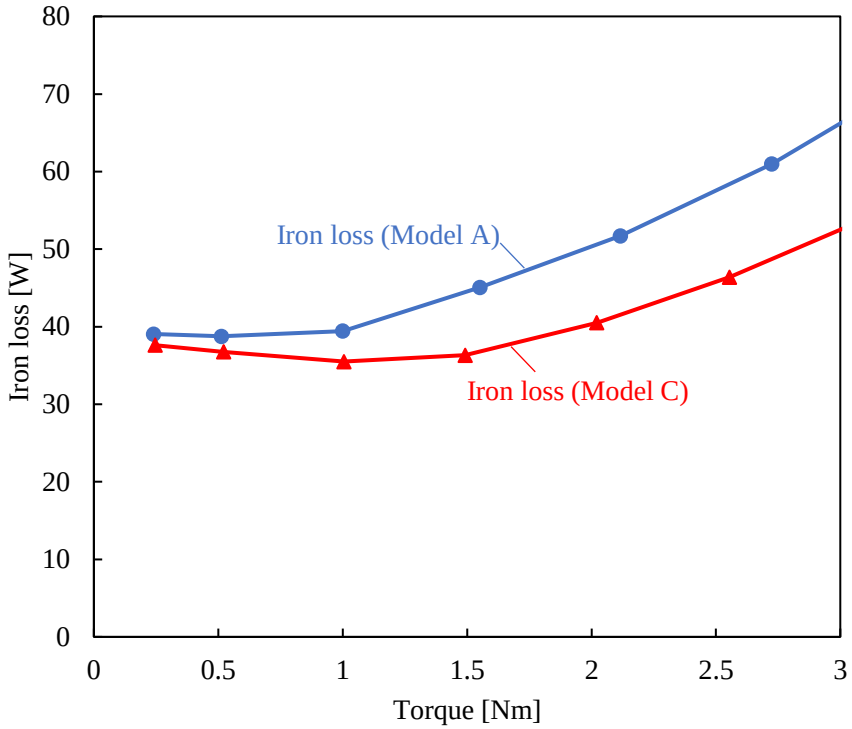


(a) Iron loss

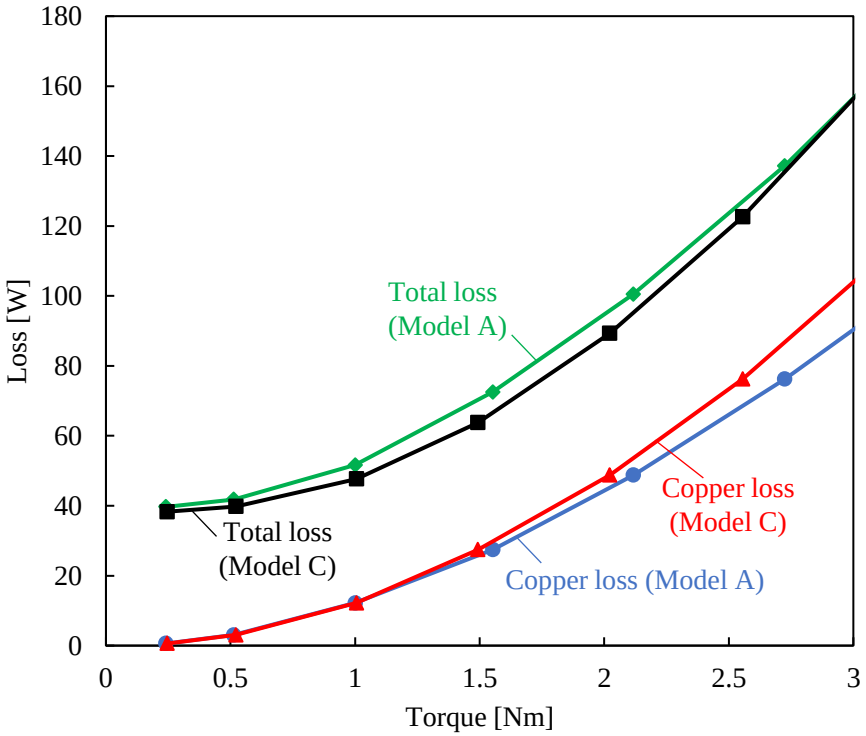


(b) Copper and total losses

Fig. 2.19 Losses with the variation of torque at 7200 rpm

Fig. 2.20 shows the efficiency difference map obtained by subtracting the efficiency of Model A from that of Model C ($\eta_C$ - $\eta_A$). Same with Model B, Model C is also more efficient than Model A over the entire target operating line. Especially at operating point III, the iron loss of Model C is 37.00 W, which is 17.31% lower than the 44.75 W in Model A. As a result, the efficiency of Model C is 94.64%, which is 0.46% higher than the 94.18% in Model A. Moreover, because iron loss is dominant in the high-speed low-torque operating area, the efficiency of Model C has been significantly enhanced.

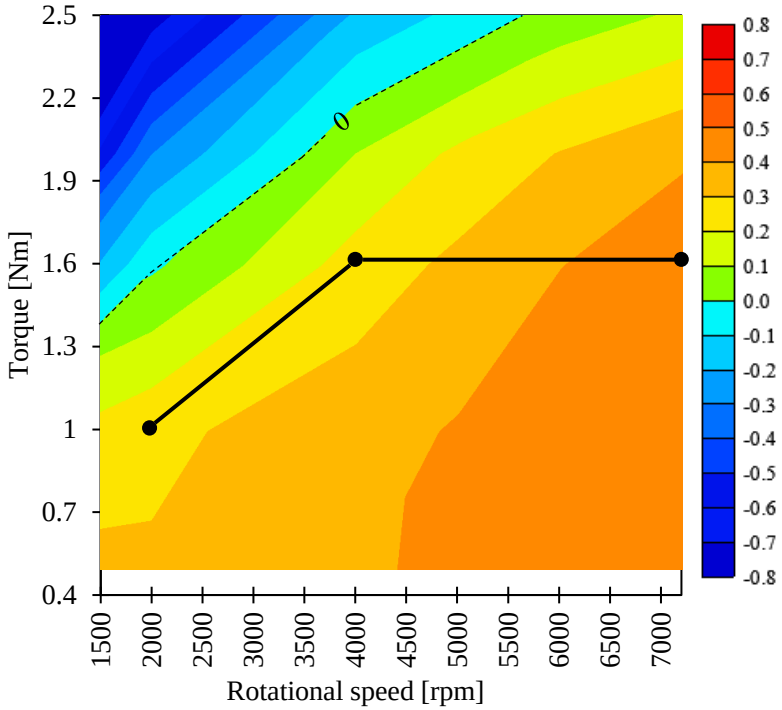


Figure 2.20 Efficiency difference map obtained by $\eta_C$ - $\eta_A$

Fig. 21 shows the efficiency difference map obtained by subtracting the efficiency of Model B from that of Model C ($\eta_C - \eta_B$). At operating point III, the iron losses of Model B and C are 47.55 W and 37.00 W, respectively. As a result of a smaller iron loss, the efficiency of Model C is 0.29% larger. However, when the operating point is changed from III to II, the torque remains constant at 1.6 Nm while rotational speed decreases. Therefore, copper loss does not change drastically as iron loss does. The iron loss of Model C decreases from 37.00 W at operating point III to 19.04 W at operating point II, while the copper loss only decreases from 31.54 W to 29.14 W. The copper and iron losses of Model B are 23.38 W and 23.21 W at operating point II, respectively. Although the iron loss of Model C is still smaller than that of Model B, copper loss should be emphasized at operating point II. As a result of a smaller copper loss, the efficiency of Model B is 0.19% higher than that of Model C at operating point II.

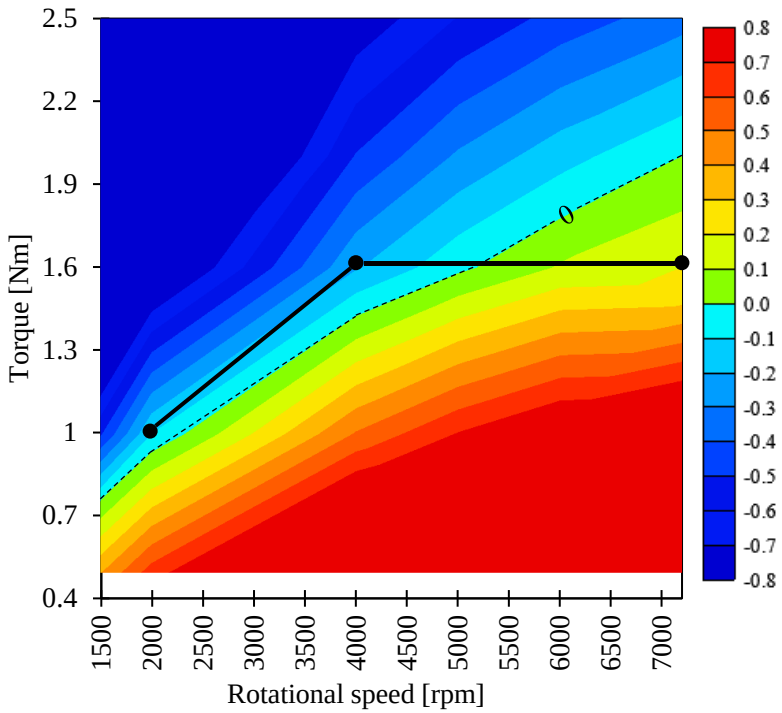


Figure 2.21 Efficiency difference map obtained by $\eta_C$ - $\eta_B$

Fig. 2.22 shows the comparison of efficiency over the entire operating area. The efficiency of Model B is the highest in operating areas *E* and *F*, where copper loss should be emphasized. While the efficiency of Model C is the highest at operating areas *G* and *H*, where iron loss should be emphasized. Moreover, although the efficiency of both Models B and C is higher than that of Model A over the entire target operating line, Model B is more efficient at operating point II, while the Model C is more efficient at operating point III.

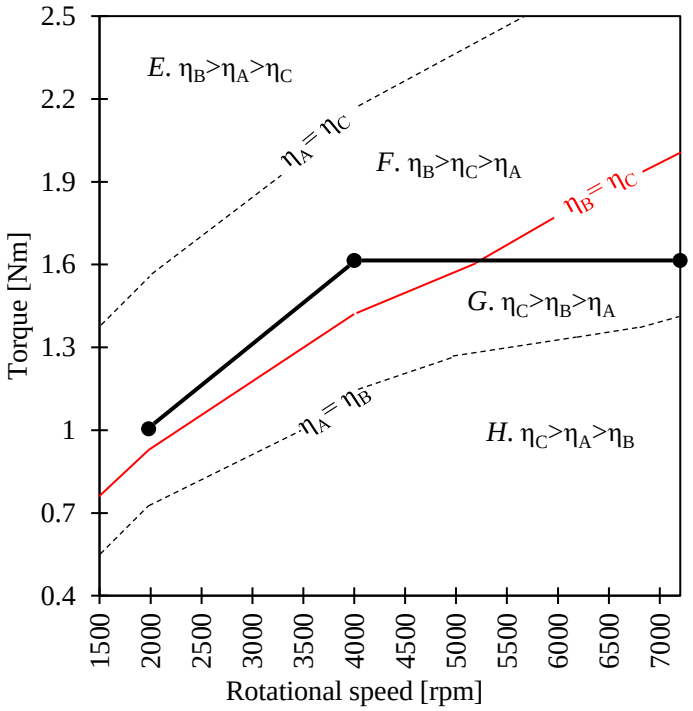


Figure 2.22 Comparison of efficiency over entire operating area

## Section 2.5 Investigation of rotor structure that can take advantage of both Rotors B and C

In chapters III and IV, Model B can reduce copper loss by adopting large flux barriers to concentrate the magnetic flux of PMs on *d*-axis while suppressing *q*-axis magnetic flux. And Model C can reduce iron loss by adopting a disproportional airgap to suppress *q*-axis magnetic flux and the harmonic components of *dq*-axis magnetic flux. To take advantage of both Models B and C for further enhancing efficiency on the target operating line, a novel rotor structure is proposed in this chapter.

Fig. 2.23 shows the rotor structure of Model D. There are both large flux barriers and a disproportional airgap on *q*-axis magnetic flux path to concentrate the magnetic flux of PMs on *d*-axis while suppressing *q*-axis magnetic flux and the harmonic components of *dq*-axis magnetic flux in this model.

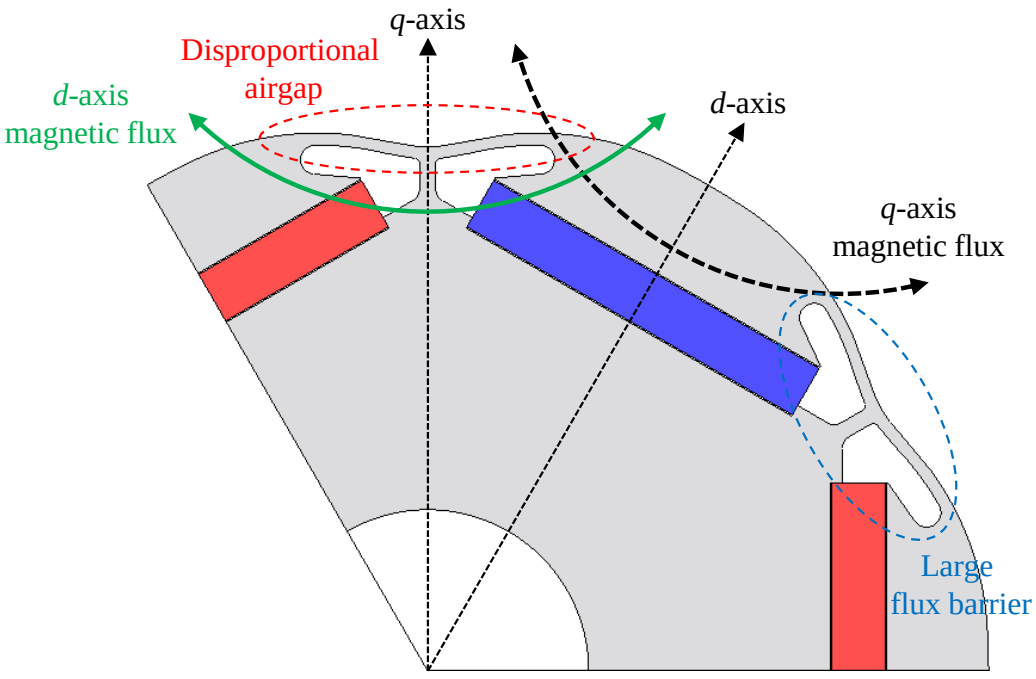


Figure 2.23 Rotor structure of Model D

Fig. 2.24 shows the magnetic flux density waveforms of Models B, C and D observed in the airgap. The observation method is the same as in Model B, as shown in Fig. 2.4. Table 2.2 shows the fundamental wave amplitudes and their THDs of the magnetic flux density waveforms shown in Fig. 2.24. The fundamental wave amplitude of Model D is

0.808 T, which is 1.52% lower than the 0.820 T in Model B and 8.20% higher than the 0.747 T in Model C. Moreover, the THD of Model D is 14.30%, which is smaller than the 16.81% in Model B and higher than the 3.18% in Model C. Furthermore, Fig. 2.25 shows the $q$-axis magnetic flux waveforms of Models B, C and D at operating point II. The fundamental component of $q$-axis magnetic flux in Model D is the smallest because of its narrowest $q$-axis magnetic flux path. Therefore, iron loss can be suppressed in Model D by suppressing $q$-axis magnetic flux, as discussed in Section 2.3.

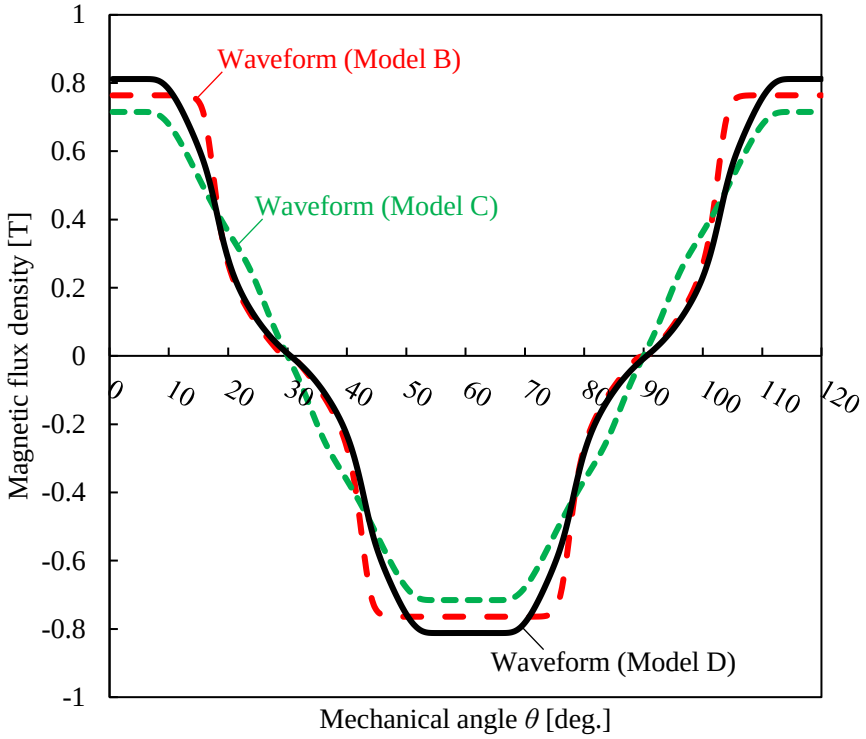


Figure 2.24 Magnetic flux density waveforms observed in the airgap

Table 2.2 Fundamental wave amplitudes and their THDs of the magnetic flux density waveforms

| | A | B | C | D |
|---|---|---|---|---|
| Fundamental wave amplitude [T] | 0.724 | 0.820 | 0.747 | 0.808 |
| THD [%] | 29.44 | 16.81 | 3.18 | 14.30 |

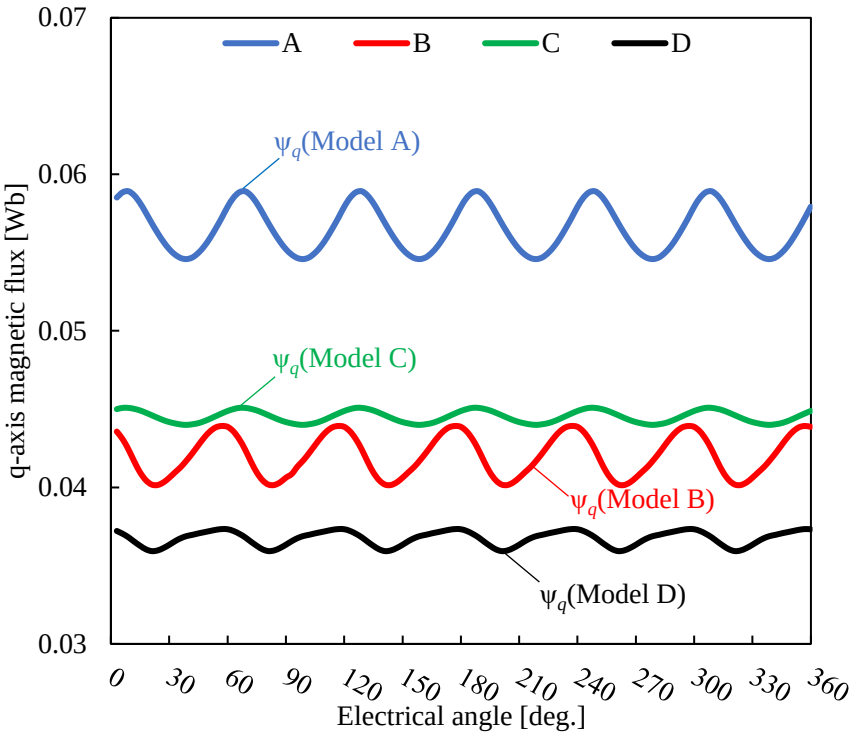


Figure 2.25 *Q*-axis magnetic flux waveform at operating point II

As can be seen in Figs. 2.11 and 2.17, iron loss has a significant 3rd harmonic component in addition to the 5th and 7th harmonic components. Fig. 2.26 shows the cause of the generation of 3rd harmonic magnetic flux. A portion of magnetic flux generated by PMs passes the stator tooth's lower portion without interlinking with the armature windings. Therefore, this magnetic flux component will not be reflected in either *d*-axis magnetic flux or *q*-axis magnetic flux. The magnetic path of the 3rd harmonic magnetic flux implies that it can be suppressed by narrowing the *q*-axis magnetic flux path. Fig. 2.27 shows the 3rd harmonic iron loss component distributions of the four models at 7200 rpm and no load. The lower part of the stator tooth generates a large 3rd harmonic iron loss component, as shown in Fig. 2.27(a). The value of Model A is the largest, which is 4.40 W. And the 3rd harmonic iron loss of Model D is the smallest, which is 1.72 W.

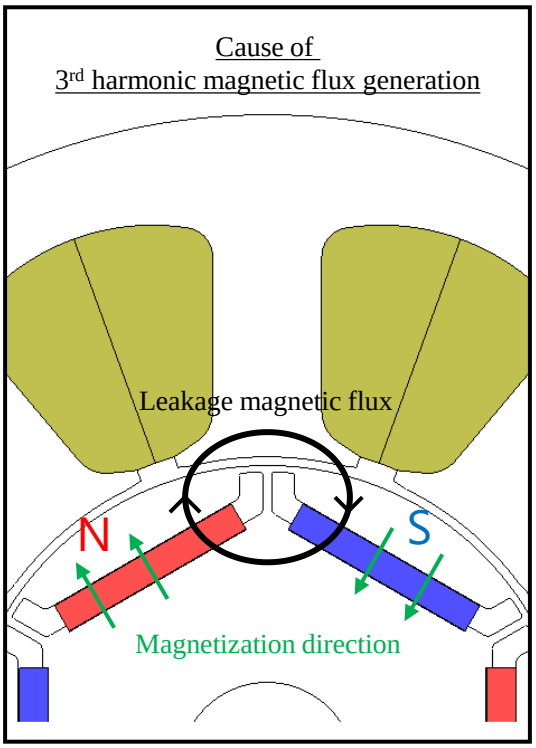


Figure 2.26 Cause of 3rd harmonic magnetic flux generation

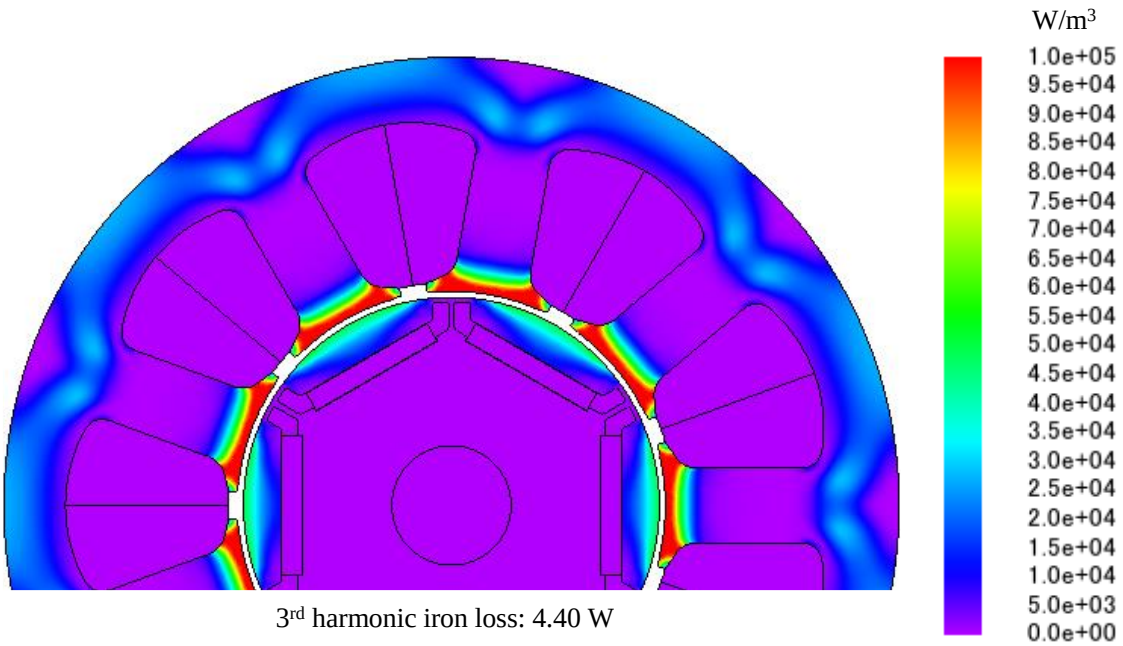


3rd harmonic iron loss: 4.40 W

(a) Model A

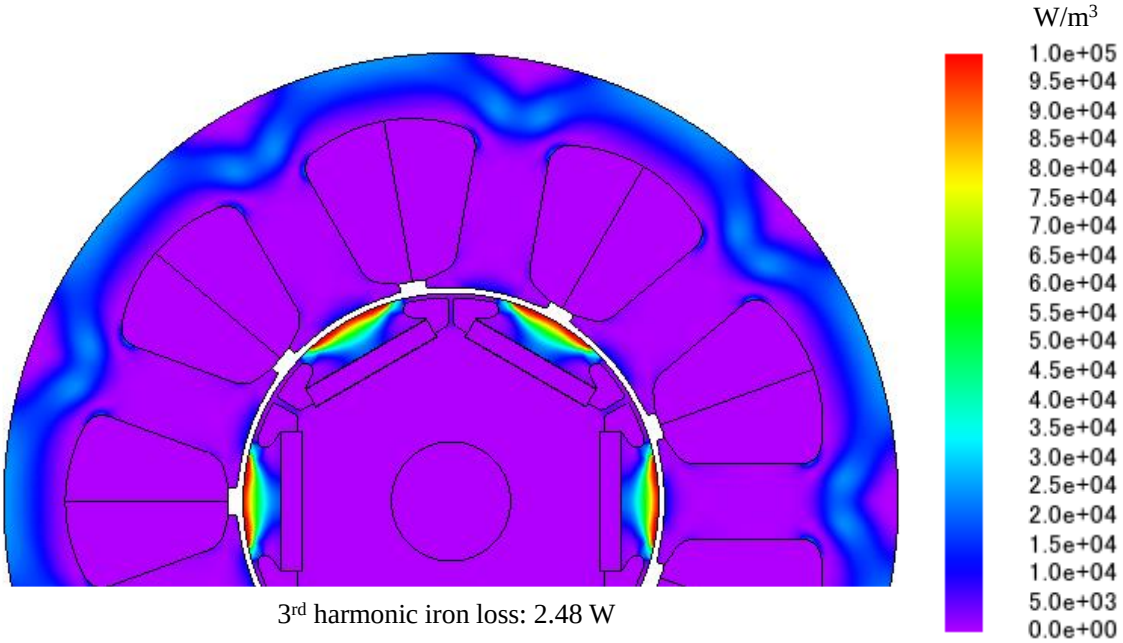


3rd harmonic iron loss: 2.48 W

(b) Model B

Figure 2.27 3rd harmonic iron loss component distribution at 7200 rpm and no load

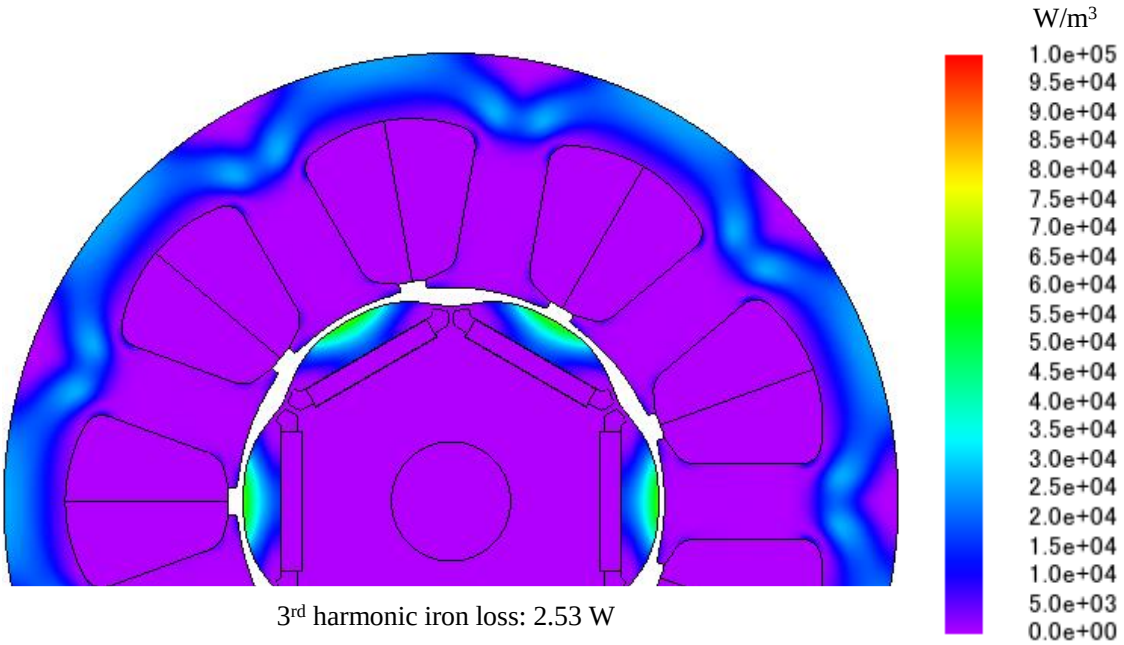


3rd harmonic iron loss: 2.53 W

(c) Model C

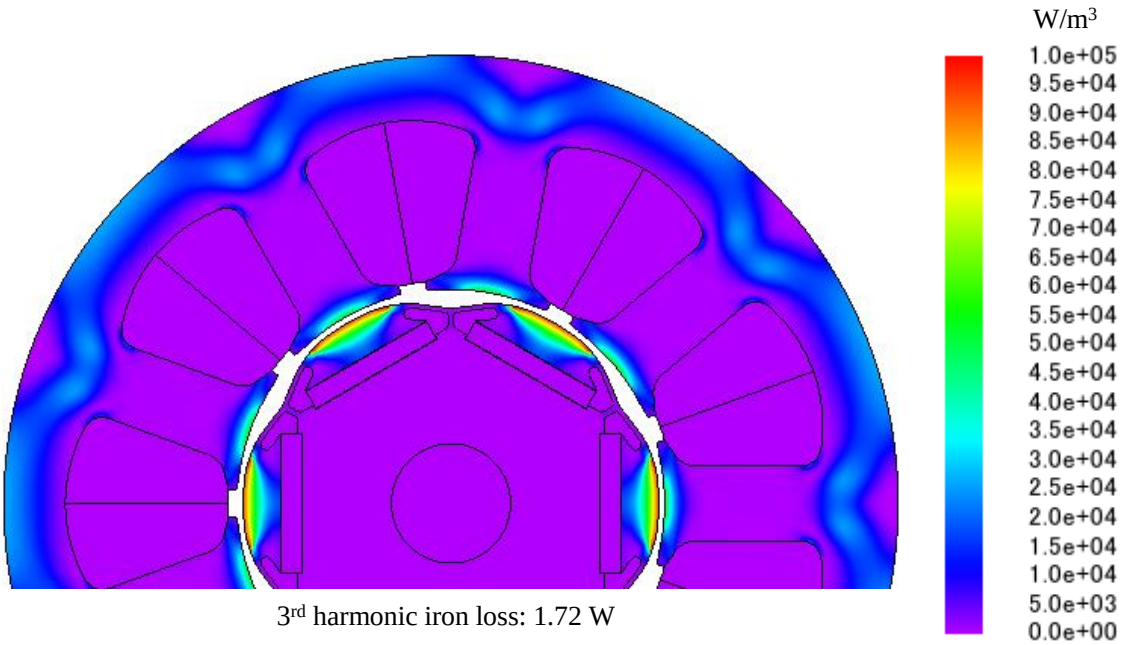


3rd harmonic iron loss: 1.72 W

(d) Model D

Figure 2.27 3rd harmonic iron loss component distribution at 7200 rpm and no load

Fig. 2.28 shows the efficiency difference map obtained by subtracting the efficiency of Model B from that of Model D ($\eta_D - \eta_B$). Model D has a slightly smaller PM magnetic flux density than Model B, and the *q*-axis magnetic flux has been effectively suppressed, resulting in an increase in copper loss and a decrease in iron loss. As a result, the efficiency of Model D is slightly higher than that of Model B at operating points I and II, and higher than Model B at operating point III.

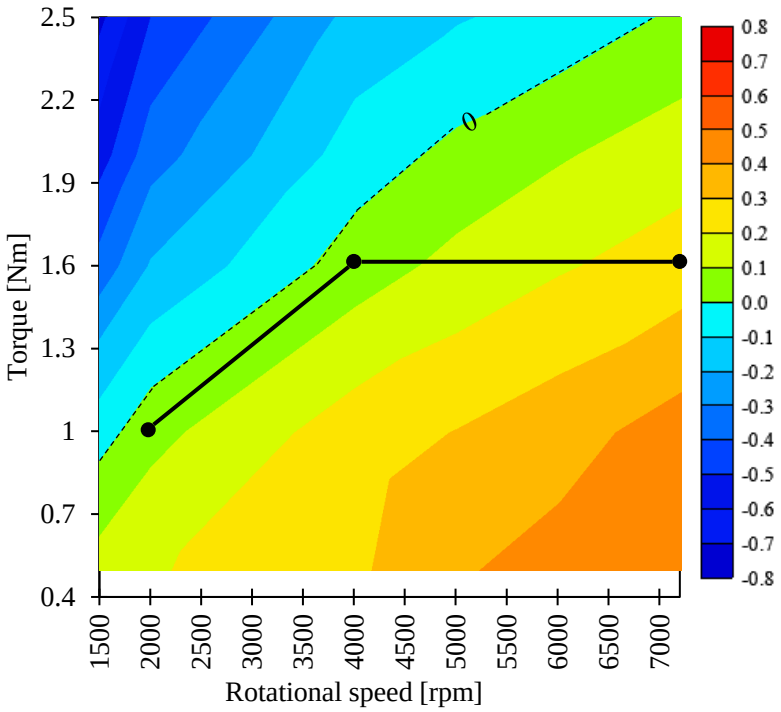


Figure 2.28 Efficiency difference map obtained by $\eta_D$- $\eta_B$

Fig. 2.29 shows the efficiency difference map obtained by subtracting the efficiency of Model C from that of Model D ($\eta_D - \eta_C$). Model D has a larger PM magnetic flux density than Model C, resulting in an increase in iron loss and a decrease in copper loss. And a smaller *q*-axis magnetic flux, which can suppress iron loss. As a result, the efficiency of Model D is nearly equal to that of Model C at operating point III, but higher at operating points I and II.

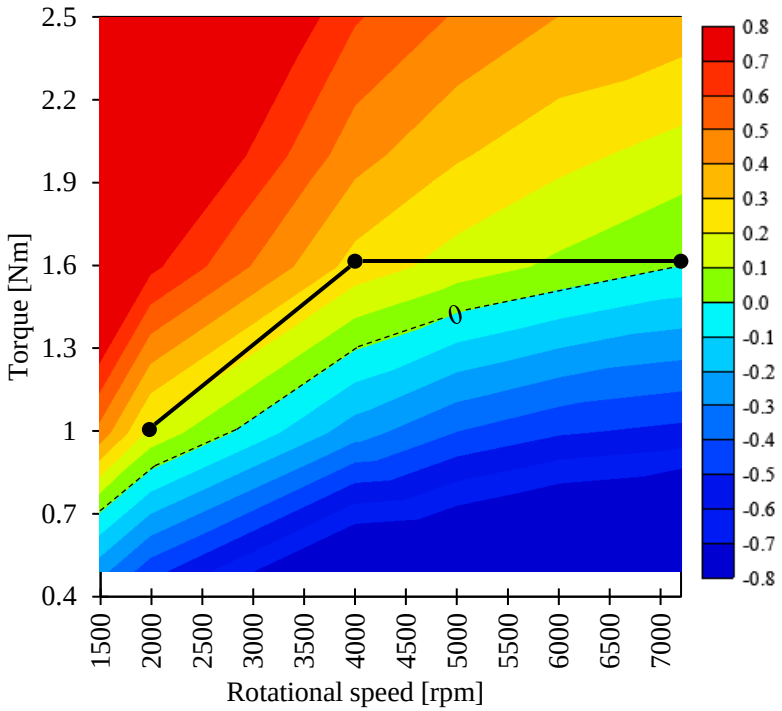


Figure 2.29 Efficiency difference map obtained by $\eta_D$- $\eta_C$

Fig. 2.30 shows the comparison of the efficiency of Models B, and D over the entire operating area. The copper loss is dominant in operating area *E*. Therefore, Model B has the highest efficiency in this operating area because of its largest PM magnetic flux density, implying that the magnetic torque was utilized most effectively. The iron loss is dominant in operating area *H*. Therefore, Model C has the highest efficiency in this operating area because its PM magnetic flux density is small, and the *q*-axis and the harmonic components of *dq*-axis magnetic flux were suppressed. The efficiency of Model D is the highest at operating points *F* and *G* because the magnetic torque was utilized effectively, and the *q*-axis magnetic flux is the smallest, while the harmonic components of *dq*-axis magnetic flux were also suppressed. The iron loss of Model D is smaller than that of Model B, while the copper loss is smaller than that of Model C. As a result, Model D realized a tradeoff between copper and iron losses to minimize total loss, and has the highest efficiency at the target operating line.

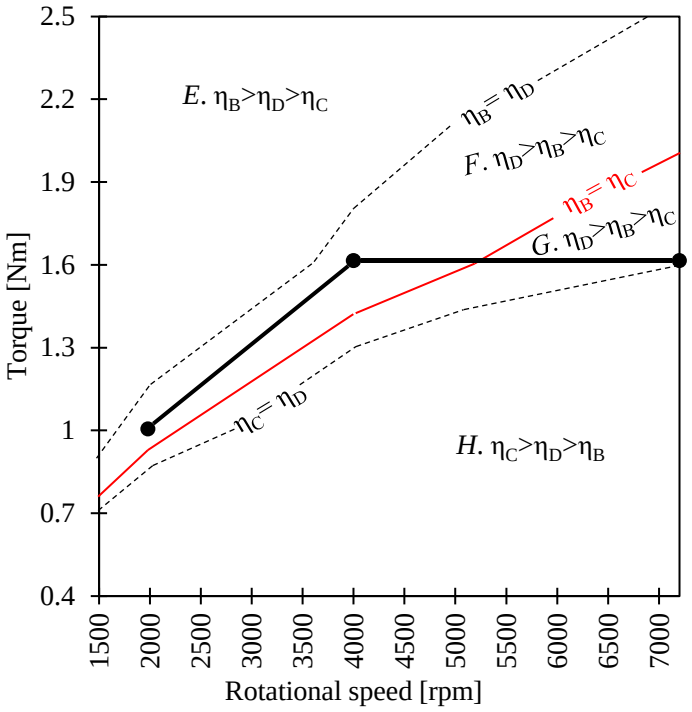


Figure 2.30 Comparison of efficiency over entire operating area

## Section 2.6 Experimental verification of Topic I

A prototype machine is manufactured to verify the 2D-FEM results. Fig. 2.31 shows the appearance of the prototype machine.

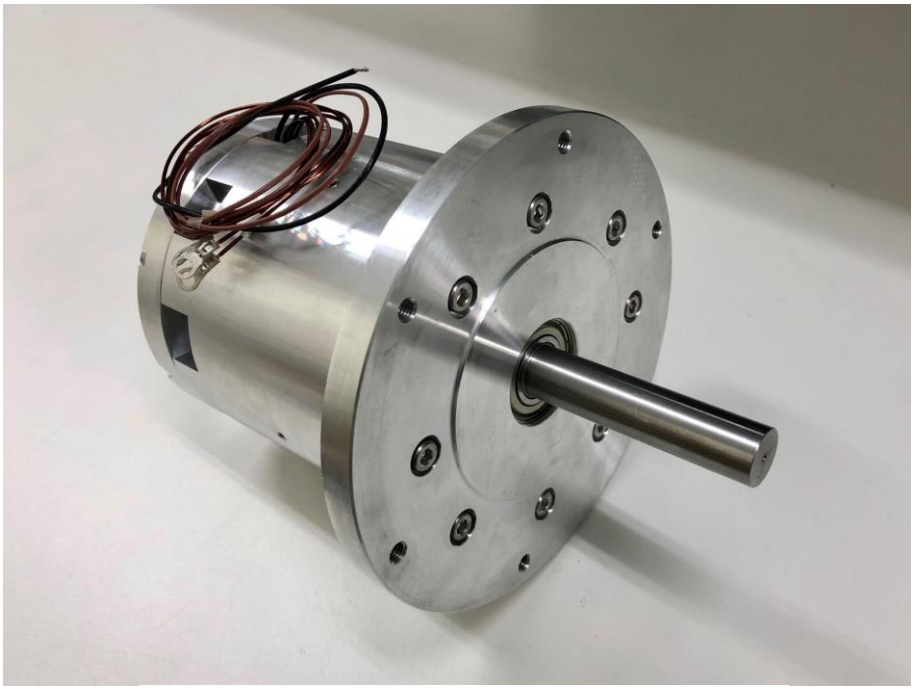

Figure 2.31 Appearance of the prototype machine

Fig. 2.32 shows the appearance and enlarged views of the four rotors. To ensure the experimental accuracy, the rotors can be disassembled from the shaft while the same shaft is being used.

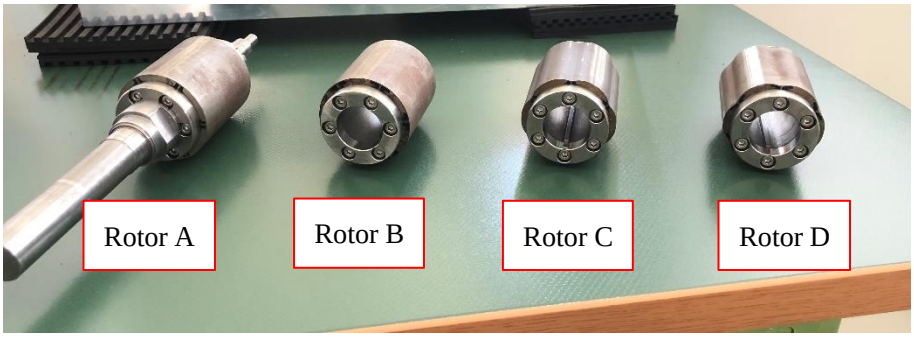


(a) Appearance of the four rotors

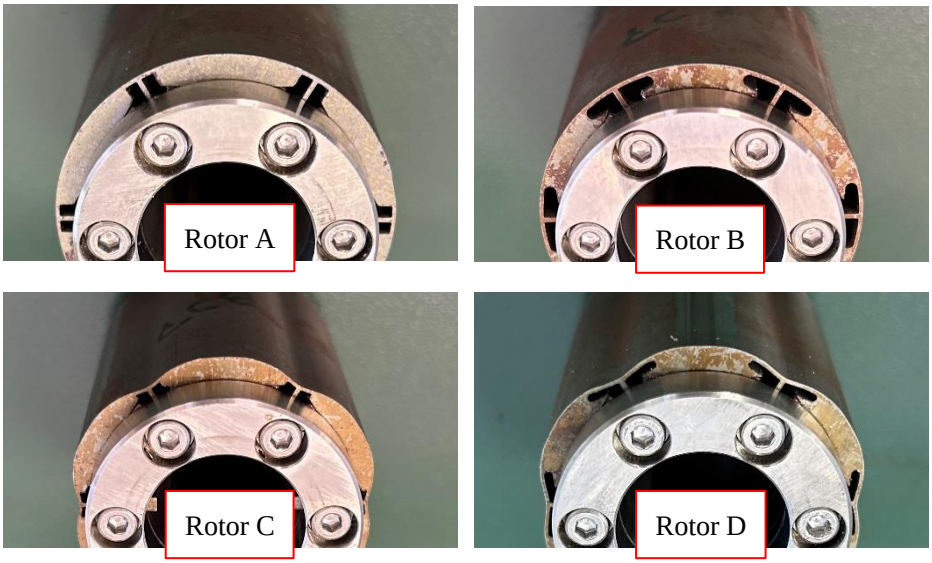


(b) Enlarged views of the four rotors

Figure 2.32 Appearance and enlarged views of the four rotors

The mechanical stress distribution of Models A and D are shown in Fig. 2.33. Because the diameter of the rotor is 41.8 mm, and the maximum rotational speed is 7200 rpm, the max mechanical stress for Model D is only 17 Mpa, which is sufficient for the 278 Mpa yield strength of the electrical steel used in the prototype. Moreover, because the width of bridges in rotor remains constant for Models A and D, mechanical stress does not change significantly.

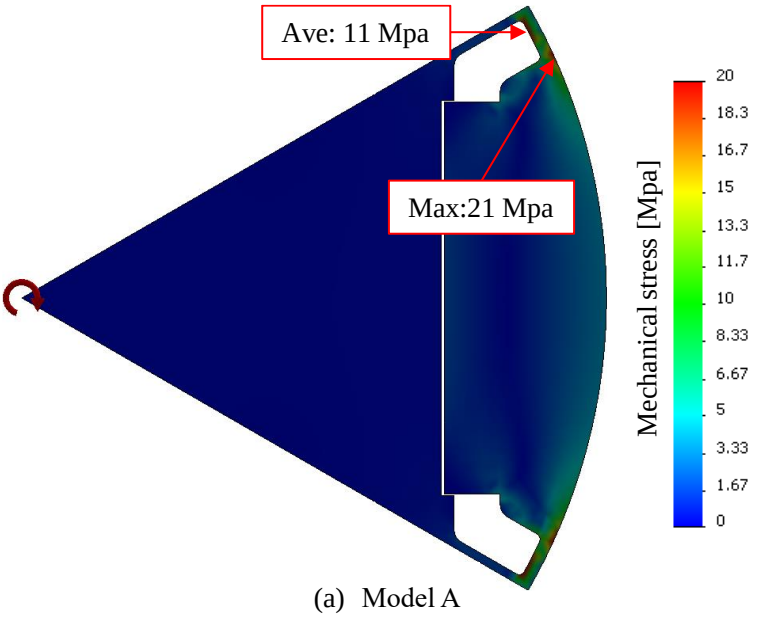


(a) Model A

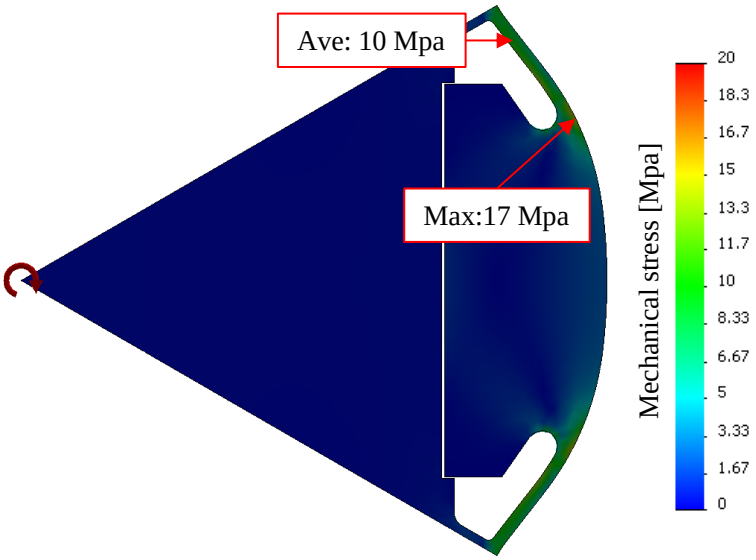


(b) Model D

Figure 2.33 Mechanical stress distribution of Models A and D

Fig. 2.34 shows the appearance of the measurement and drive devices. Fig. 2.34(b) shows the test platform and the prototype. The digital controller and inverter are shown in Fig. 2.34(c), and the power meter, which model is YOKOGAWA WT1804E, is shown in Fig. 2.34(d).

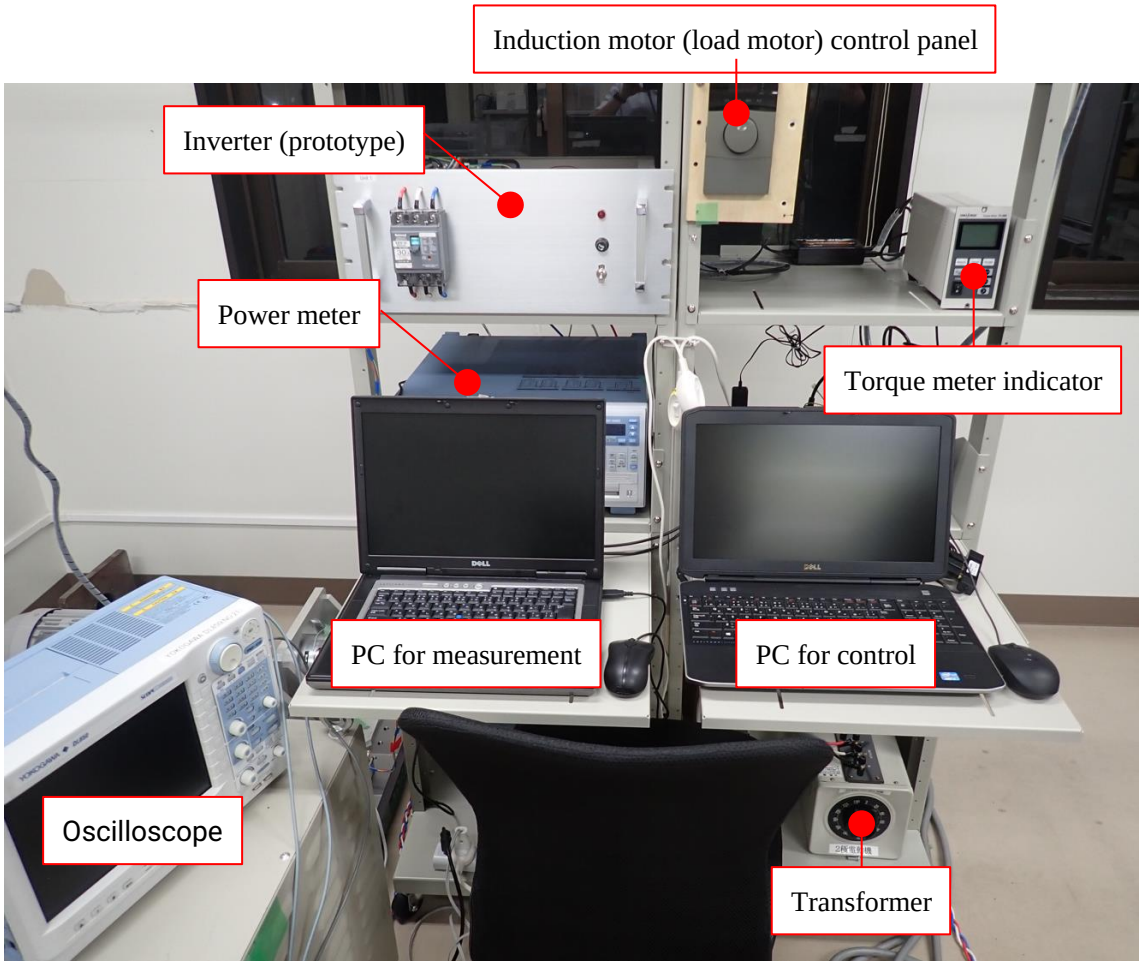


(a) Control and record devices

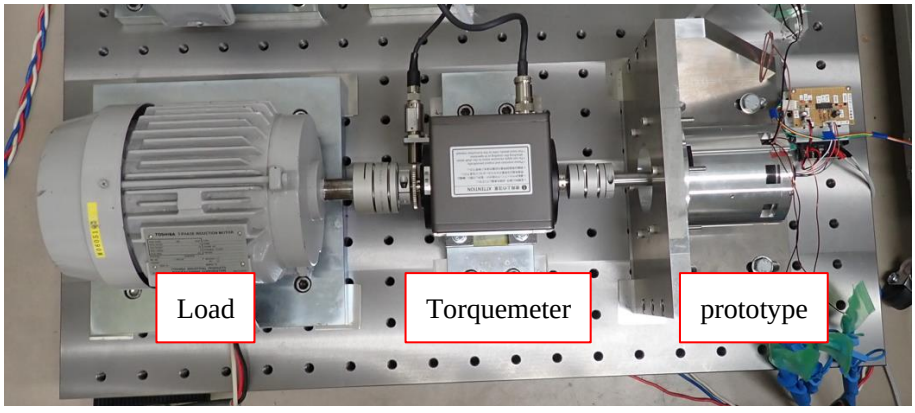


(b) Test platform

Figure 2.34 Appearance of the measure and drive devices

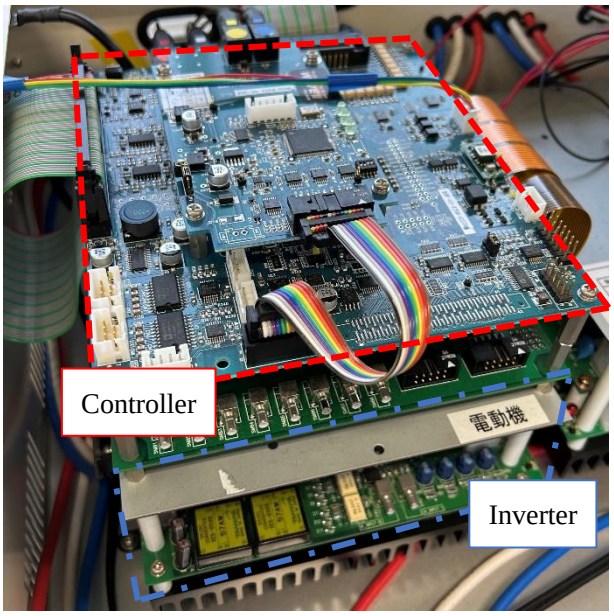


(c) Digital controller and inverter


(d) Power meter

Figure 2.34 Appearance of the measure and drive devices

Fig. 2.35 shows the back electromotive forces (b-EMFs) of the four models at 4000 rpm. The measured waveforms of the four models, as shown in the figure, well matched the 2D-FEM analytical results. It should be noted that the waveform of Model C is close to an ideal sine wave. In general, the iron loss is considered to be reduced when the b-EMF voltage is closer to a sine wave. In fact, Model C always has the smallest iron loss. However, Model D has the highest efficiency for the target operating area because not only iron loss, but also copper loss should be considered.

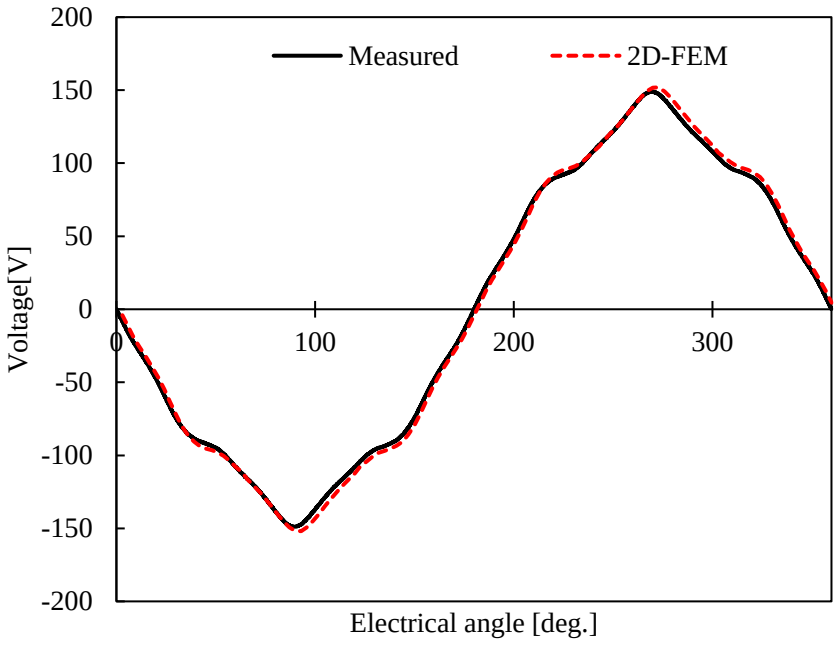


(a) Model A

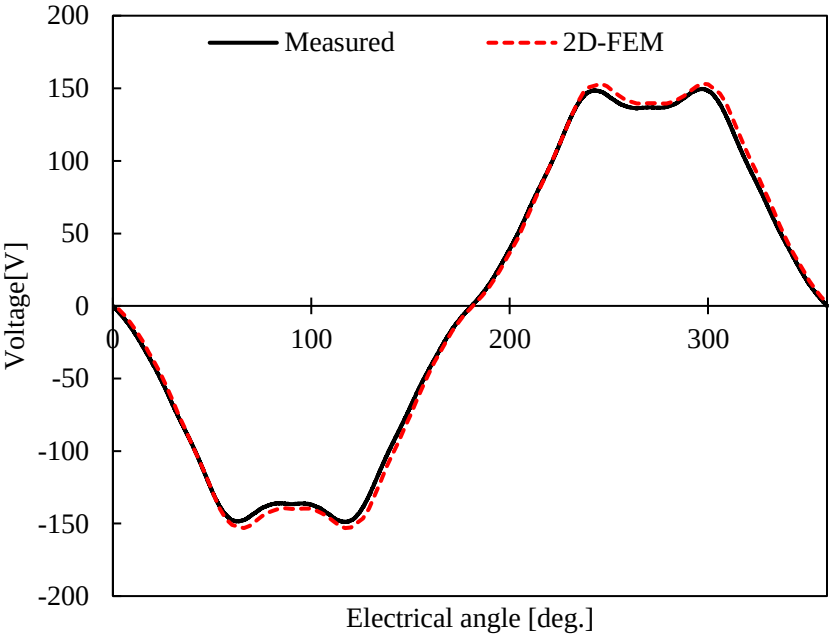


(b) Model B

Figure 2.35 B-EMF of the four models

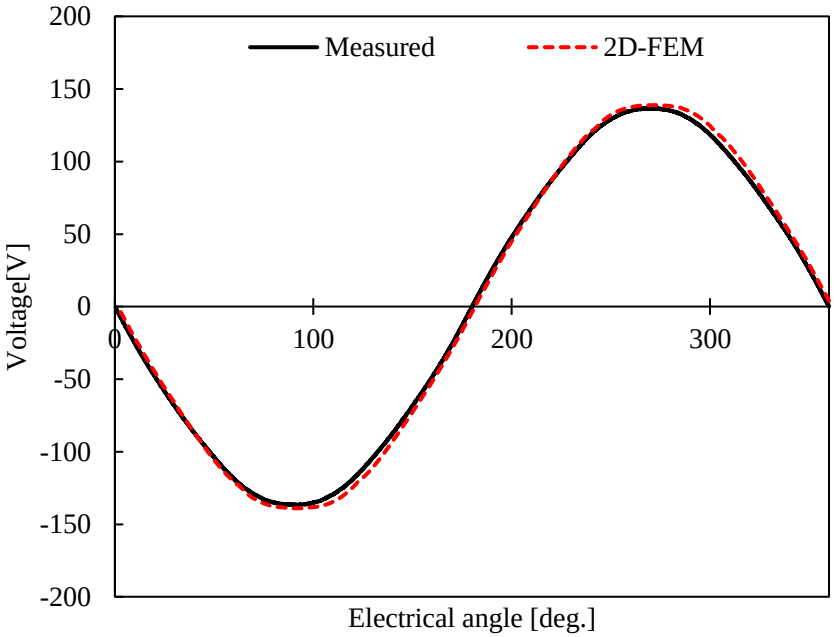


(c) Model C

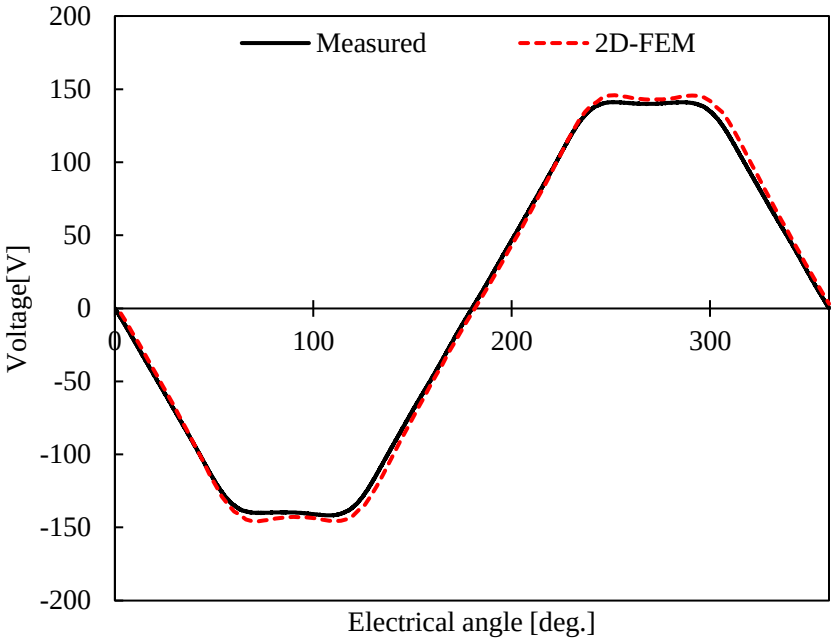


(d) Model D

Figure 2.35 B-EMF of the four models

Figs. 2.36 to 2.39 shows the comparison of efficiency maps obtained by 2D-FEM and measured efficiency maps of the four models. The *dq*-axis current control strategy using PI (proportional-integral) controller is adopted. It can be seen that the four measured efficiency maps of the four models generally follow the trends of their efficiency maps obtained by 2D-FEM. Moreover, the highest efficiencies of the four models all higher than 94.5%. And among the four models, Model D has the widest operating area where efficiency is higher than 94.5%.

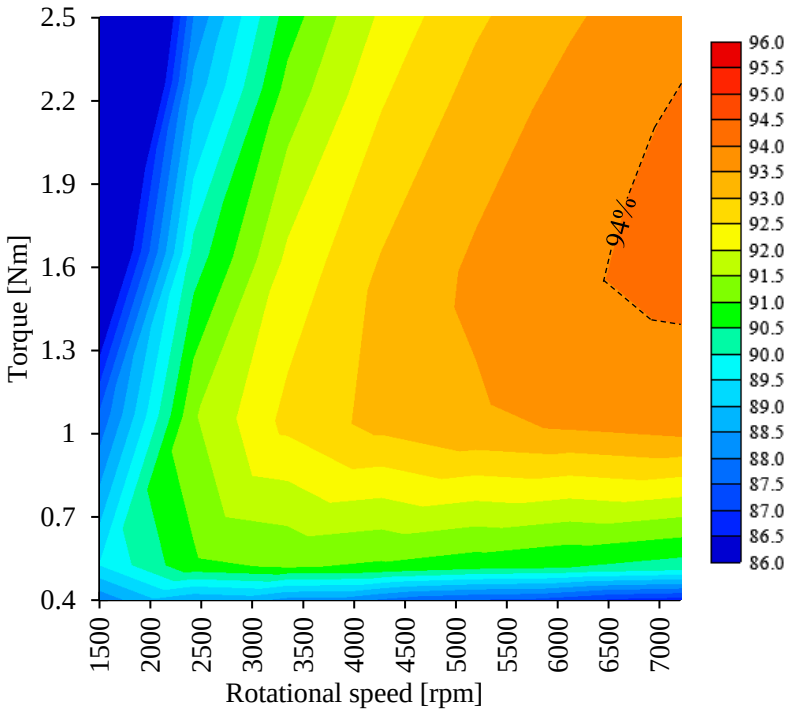


(a) Efficiency map obtained by 2D-FEM of Model A

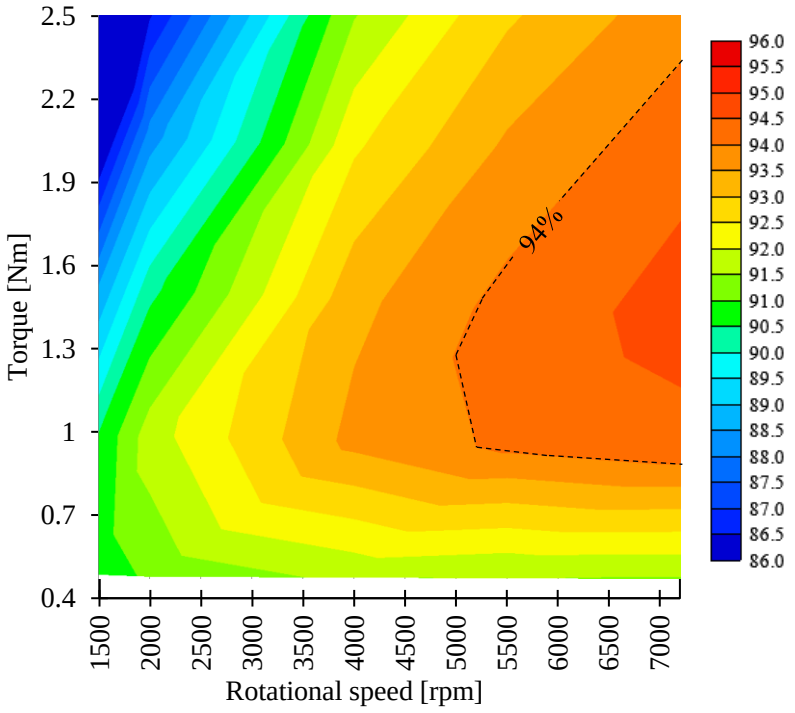


(b) Measured efficiency map of Model A

Figure 2.36 Comparison of efficiency map obtained by 2D-FEM and measured efficiency map of Model A

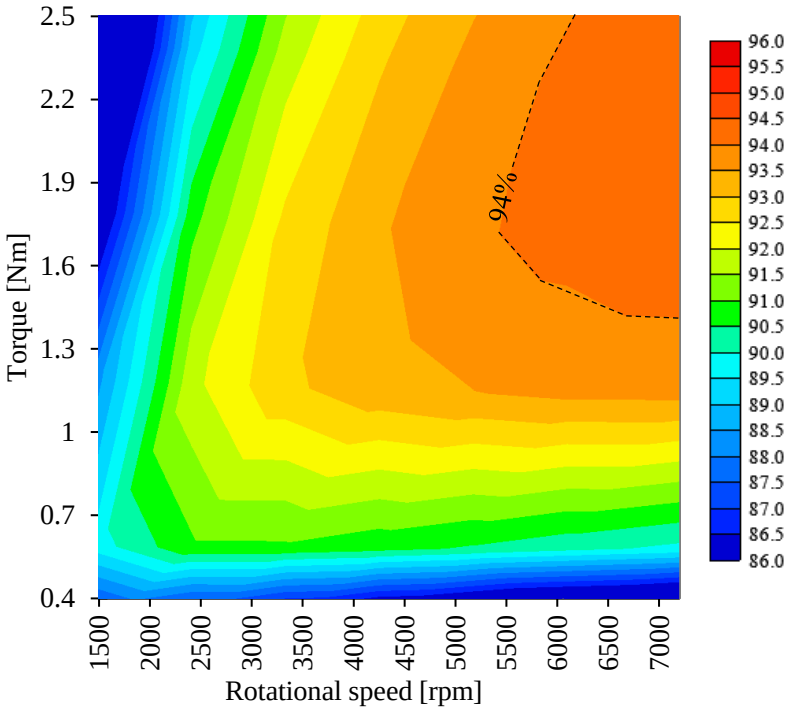


(a) Efficiency map obtained by 2D-FEMof Model B

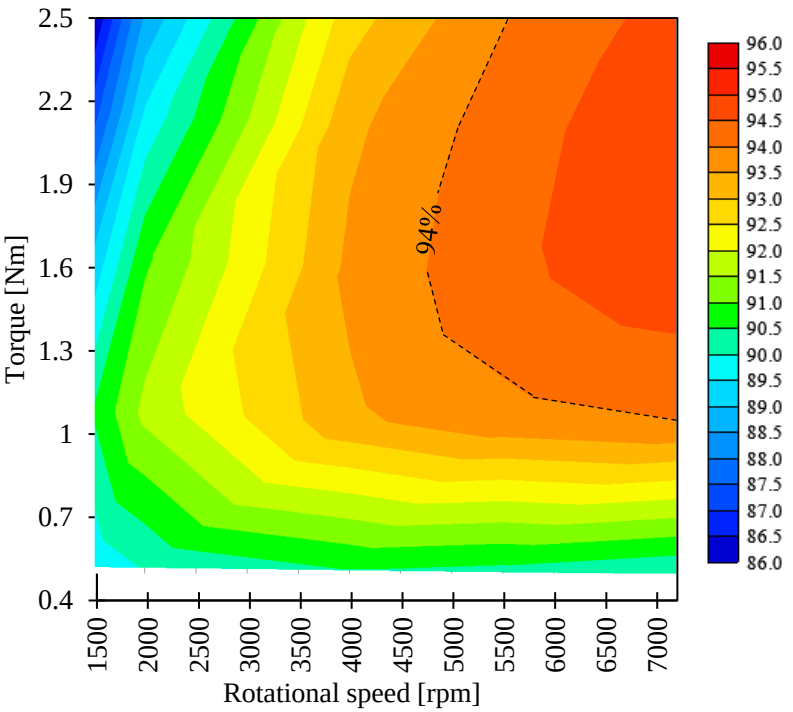


(b) Measured efficiency map of Model B

Figure 2.37 Comparison of efficiency map obtained by 2D-FEM and measured efficiency map of Model B

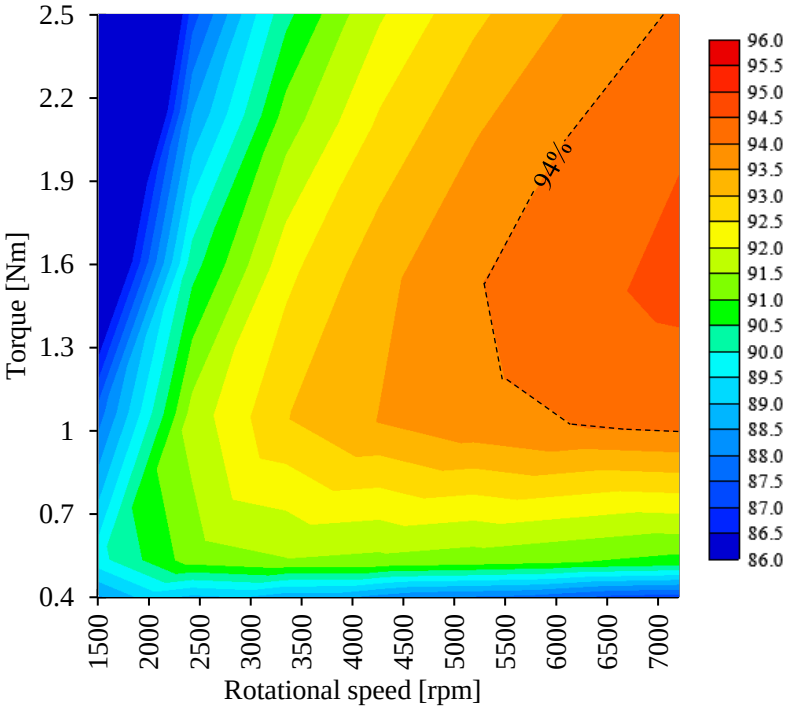


(a) Efficiency map obtained by 2D-FEM of Model C

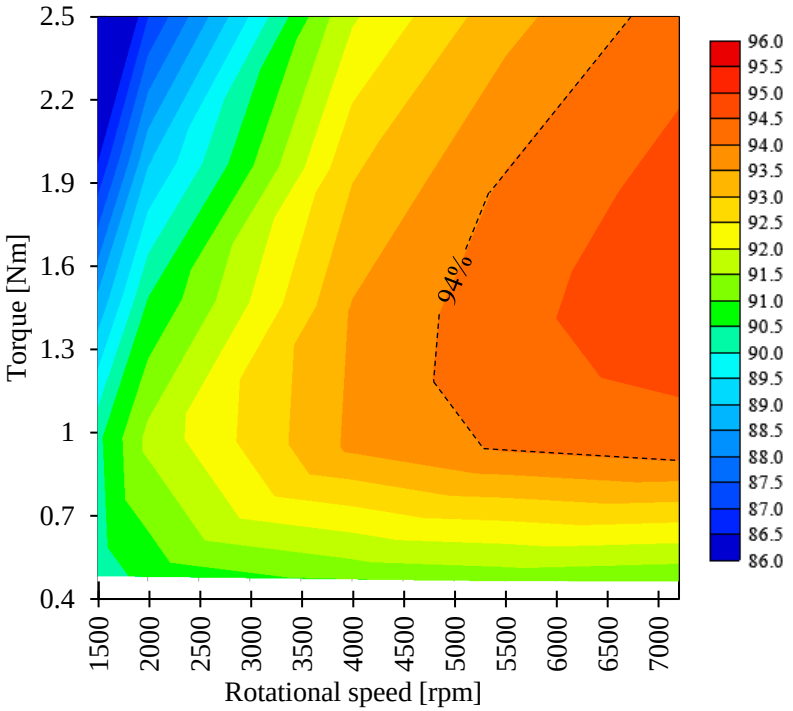


(b) Measured efficiency map of Model C

Figure 2.38 Comparison of efficiency map obtained by 2D-FEM and measured efficiency map of Model C

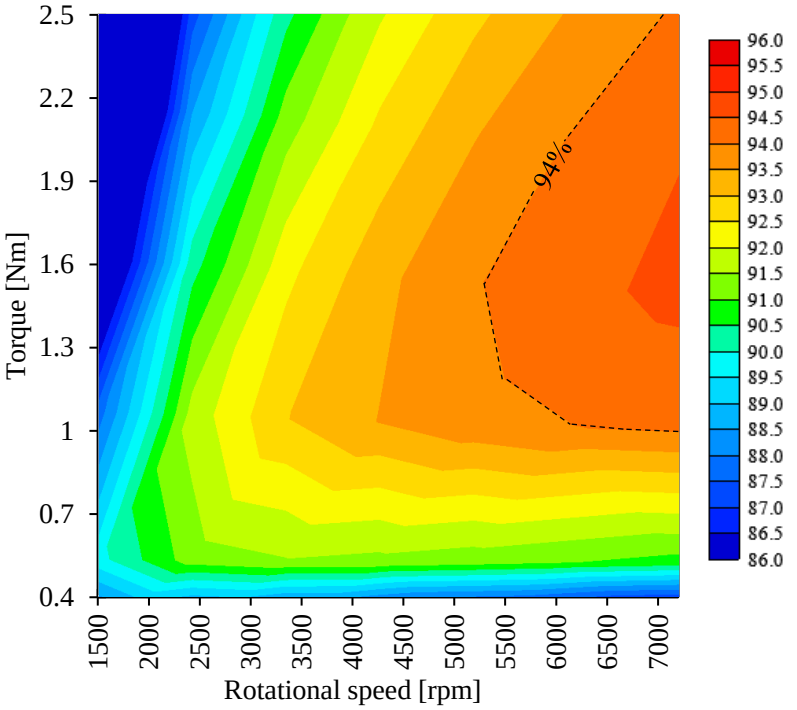


(a) Efficiency map obtained by 2D-FEM of Model D

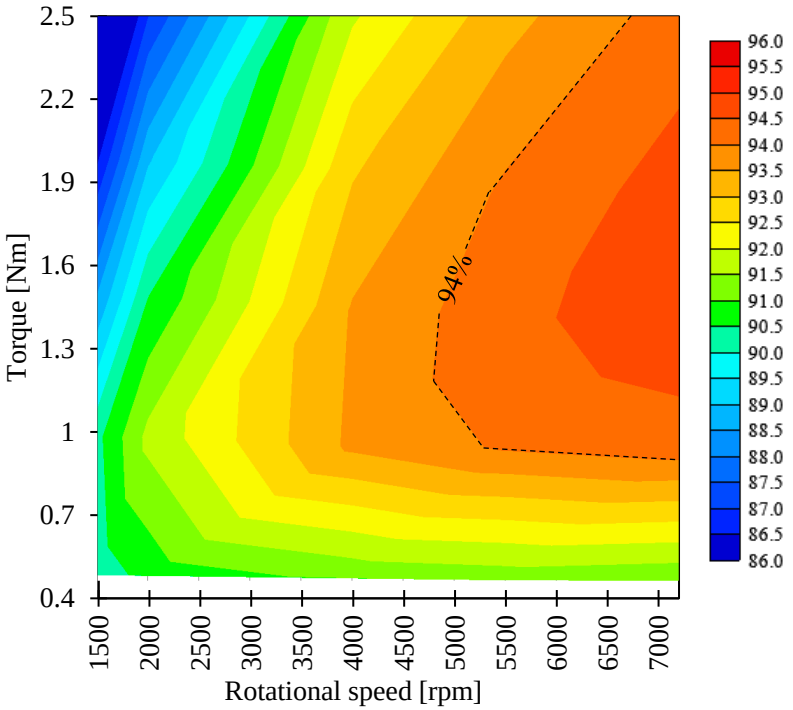


(b) Measured efficiency map of Model D

Figure 2.39 Comparison of efficiency map obtained by 2D-FEM and measured efficiency map of Model D

Fig. 2.40 shows the measured efficiency difference map obtained by subtracting the efficiency of Model B from that of Model D ($\eta_D - \eta_B$). And Fig. 2.41 shows the measured efficiency difference map obtained by subtracting the efficiency of Model C from that of Model D ($\eta_D - \eta_C$). The efficiency of Model D is higher than that of both Models B and C at the target operating line. Moreover, Fig. 2.42 shows the comparison of the measured efficiency of Models B, C, and D over the entire operating area. The efficiency of Model D is highest at the target operating line. It should be noted that when compared to the 2D-FEM results, the operating area with the highest measured efficiency of Model D shifted slightly to the low-torque operating area because the proportion of copper loss in measured results is larger.

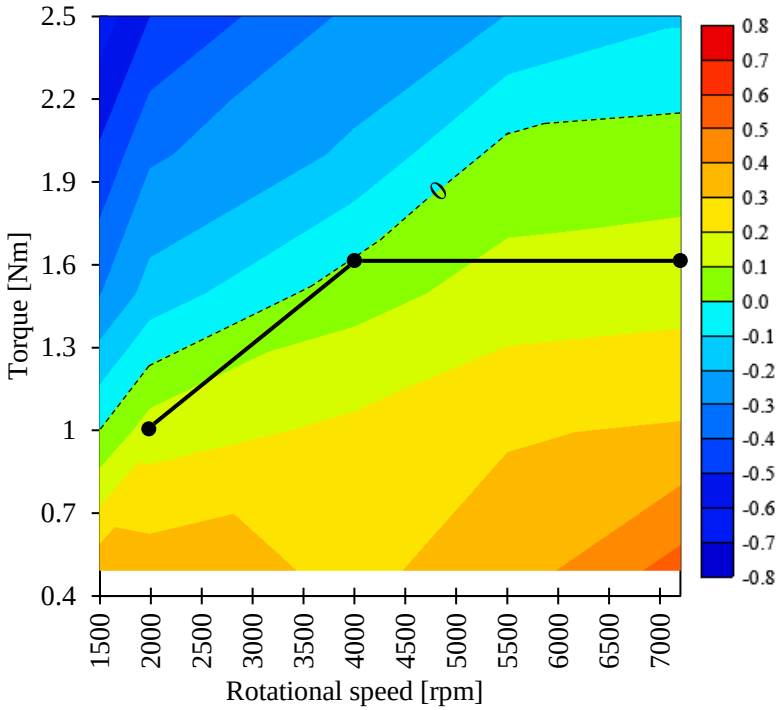


Figure 2.40 Measure efficiency difference map obtained by $\eta_D - \eta_B$

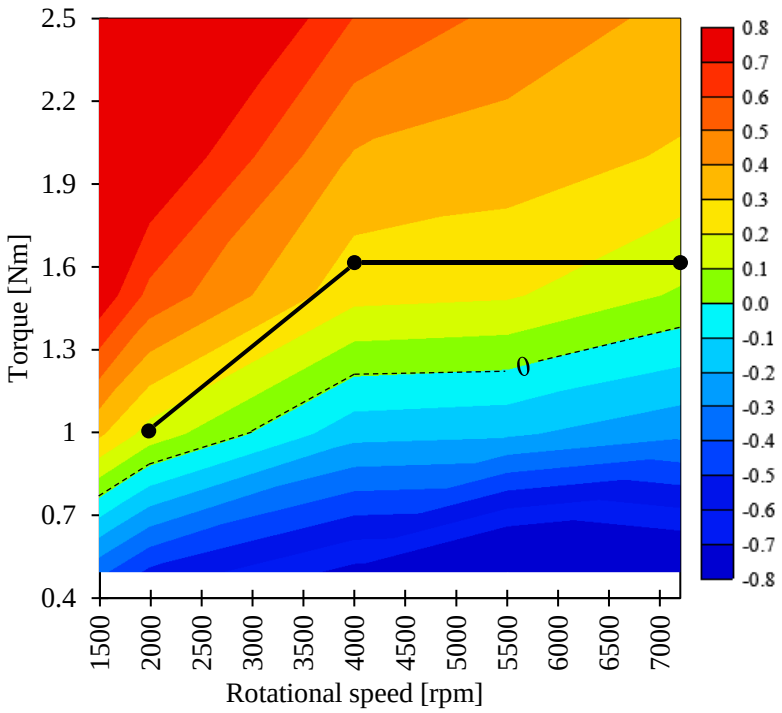


Figure 2.41 Measure efficiency difference map obtained by $\eta_D - \eta_C$

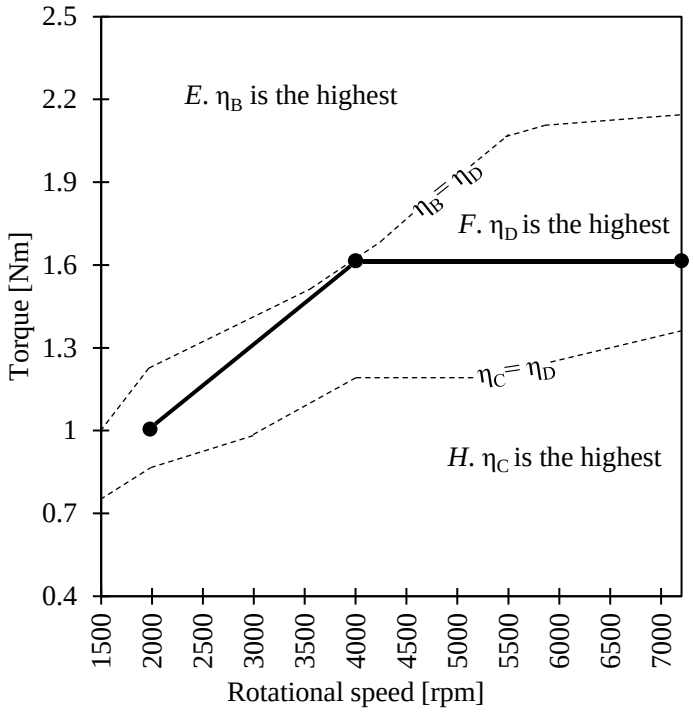


Figure 2.42 Comparison of the measured efficiency over the entire operating area

## Section 2.7 Conclusion of Topic I

This chapter proposed a novel rotor structure which can enhance efficiency at the target wide-speed middle-torque operating area without additional manufacturing costs. The proposed rotor structure employs both large flux barriers and a disproportional airgap on *q*-axis magnetic flux to concentrate the magnetic flux of PMs on *d*-axis while suppressing *q*-axis magnetic flux and the harmonic components of *dq*-axis magnetic flux. This chapter first examined the effects of adopting large flux barriers and a disproportional airgap on utilization ratio of magnetic flux generated by PMs, the dimension of *q*-axis magnetic flux path, and the proportion of harmonic iron loss components, before examining their effects on copper and iron losses. As a result, the proposed rotor structure can reduce copper loss by effectively utilizing magnetic torque and iron loss by suppressing *q*-axis magnetic flux. A tradeoff between copper and iron losses has been realized in the proposed rotor structure to minimize total loss for the target operating line. Furthermore, this chapter also clarified the design method for a suitable rotor structure depending on its target operating area. The results are as follows. For the target wide-speed middle-torque operating area, the proposed rotor structure is most suitable. For a low-speed high-torque operating area, adopting only large flux barriers is most suitable. And for a high-speed low-torque operating area, adopting only a disproportional airgap is most suitable. Finally, a prototype was manufactured to verify the results above.

## Section 2.8 Data of Topic I

Table 2.3 Operating point I (2000 rpm, 1 Nm)

| | A | B | C | D |
|---|---|---|---|---|
| Rotational speed [rpm] | 2000 | 2000 | 2000 | 2000 |
| Winding resistance (one phase) [ohm] | 0.601348 | 0.601348 | 0.601348 | 0.601348 |
| Operating current [Arms] | 2.452 | 2.219 | 2.46 | 2.28 |
| Current phase angle [deg.] | 22 | 16 | 16 | 14 |
| Average torque [Nm] | 0.995 | 1.002 | 0.999 | 0.998 |
| Maximum torque [Nm] | 1.200 | 1.149 | 1.049 | 1.156 |
| Minimum torque [Nm] | 0.794 | 0.763 | 0.955 | 0.820 |
| Torque ripple [%] | 40.850 | 38.462 | 9.397 | 33.629 |
| Magnet torque ratio [%] | 92.492 | 96.966 | 97.299 | 98.397 |
| Reluctance torque ratio [%] | 7.508 | 3.034 | 2.701 | 1.603 |
| Ld [mH] | 4.642 | 3.647 | 3.830 | 3.330 |
| Lq [mH] | 10.076 | 7.840 | 7.149 | 6.271 |
| Copper loss [W] | 10.846 | 8.883 | 10.917 | 9.378 |
| Total iron loss [W] | 8.413 | 9.468 | 7.748 | 8.788 |
| Stator core iron loss [W] | 7.923 | 8.989 | 7.476 | 8.494 |
| Rotor core iron loss [W] | 0.438 | 0.376 | 0.266 | 0.273 |
| Magnet eddy current loss [W] | 0.052 | 0.103 | 0.005 | 0.021 |
| Output [W] | 208.476 | 209.757 | 209.203 | 209.099 |
| Input [W] | 227.735 | 228.108 | 227.868 | 227.265 |
| Efficiency [%] | 91.54 | 91.96 | 91.81 | 92.01 |

Table 2.4 Operating point II (4000 rpm, 1.6 Nm)

| | A | B | C | D |
|---|---|---|---|---|
| Rotational speed [rpm] | 4000 | 4000 | 4000 | 4000 |
| Winding resistance (one phase) [ohm] | 0.601348 | 0.601348 | 0.601348 | 0.601348 |
| Operating current [Arms] | 3.904 | 3.6 | 4.019 | 3.748 |
| Current phase angle [deg.] | 30 | 24 | 24 | 22 |
| Average torque [Nm] | 1.600 | 1.598 | 1.602 | 1.599 |
| Maximum torque [Nm] | 1.820 | 1.808 | 1.661 | 1.782 |
| Minimum torque [Nm] | 1.418 | 1.304 | 1.549 | 1.388 |
| Torque ripple [%] | 25.156 | 31.541 | 6.992 | 24.658 |
| Magnet torque ratio [%] | 85.816 | 93.727 | 93.937 | 96.279 |
| Reluctance torque ratio [%] | 14.184 | 6.273 | 6.063 | 3.721 |
| Ld [mH] | 4.822 | 4.075 | 4.268 | 3.853 |
| Lq [mH] | 9.661 | 7.378 | 7.000 | 6.103 |
| Copper loss [W] | 27.50 | 23.38 | 29.14 | 25.34 |
| Total iron loss [W] | 22.49 | 23.21 | 19.04 | 20.84 |
| Stator core iron loss [W] | 20.10 | 21.22 | 17.81 | 19.64 |
| Rotor core iron loss [W] | 1.95 | 1.35 | 1.17 | 1.02 |
| Magnet eddy current loss [W] | 0.43 | 0.63 | 0.06 | 0.18 |
| Output [W] | 670.199 | 669.2282 | 671.034 | 669.797 |
| Input [W] | 720.186 | 715.8142 | 719.210 | 715.984 |
| Efficiency [%] | 93.06 | 93.49 | 93.30 | 93.55 |

Table 2.5 Operating point III (7200 rpm, 1.6 Nm)

| | A | B | C | D |
|---|---|---|---|---|
| Rotational speed [rpm] | 7200 | 7200 | 7200 | 7200 |
| Winding resistance (one phase) [ohm] | 0.601348 | 0.601348 | 0.601348 | 0.601348 |
| Operating current [Arms] | 4.072 | 3.687 | 4.165 | 3.84 |
| Current phase angle [deg.] | 36 | 28 | 30 | 26 |
| Average torque [Nm] | 1.603 | 1.597 | 1.599 | 1.599 |
| Maximum torque [Nm] | 1.817 | 1.813 | 1.660 | 1.784 |
| Minimum torque [Nm] | 1.432 | 1.307 | 1.545 | 1.388 |
| Torque ripple [%] | 23.999 | 31.650 | 7.160 | 24.728 |
| Magnet torque ratio [%] | 83.426 | 92.669 | 92.384 | 95.538 |
| Reluctance torque ratio [%] | 16.574 | 7.331 | 7.616 | 4.462 |
| Ld [mH] | 4.997 | 4.218 | 4.446 | 3.988 |
| Lq [mH] | 9.609 | 7.376 | 7.006 | 6.109 |
| Copper loss [W] | 29.91 | 24.52 | 31.30 | 26.60 |
| Total iron loss [W] | 44.75 | 47.55 | 37.00 | 41.91 |
| Stator core iron loss [W] | 38.916 | 42.582 | 34.347 | 39.213 |
| Rotor core iron loss [W] | 4.409 | 3.014 | 2.457 | 2.150 |
| Magnet eddy current loss [W] | 1.423 | 1.952 | 0.199 | 0.553 |
| Output [W] | 1208.630 | 1204.060 | 1205.957 | 1205.778 |
| Input [W] | 1283.291 | 1276.132 | 1274.255 | 1274.295 |
| Efficiency [%] | 94.18 | 94.35 | 94.64 | 94.62 |

# Chapter 3. Topic II: Reduction in Eddy Current Loss of Special Rectangular Windings in High-torque IPMSM Used for Wind Generator

## Section 3.1 Introduction of Topic II

High-torque electric machines have been widely used in industrial applications such as energy production, electrical propulsion, and automation machinery. For wind generators, adopting high-torque electric machines can reduce or eliminate the usage of gearboxes in systems by semi-direct drive or direct drive, which can achieve higher operational reliability and cut maintenance costs [24]-[29]. Among high-torque machines, interior permanent magnet synchronous machines (IPMSMs) are widely used for their distinguished characteristics, such as simply structure, high power density, and high efficiency [6][9]. Additionally, because they do not need any external excitation current via slip-rings, which can further improve operational reliability [30].

Rectangular winding structures have been used in permanent magnet synchronous machines (PMSMs) for their high slot factor, short winding end, and good heat dissipation [31]. At the same time, concentrated winding structures have been widely adopted in PMSMs to cut manufacturing costs and use limited space effectively [12]-[15]. In previous studies, rectangular windings have been adopted in [33] to reduce the significant windings AC losses due to the proximity and skin effects caused by high speed in a PMSM adopting concentrated windings. And in [34], rectangular windings have also been adopted to minimize losses and cut manufacturing costs for a permanent magnet (PM) generator adopting concentrated windings. However, although [33] and [34] have discussed the rectangular windings used for PMSMs adopting concentrated windings and shown that losses can be reduced, neither of the models in the two studies has improved slot factor effectively. For each turn, the cross-sectional shape of the rectangular windings is typically the same. While one tooth of the concentrated windings has a generally constant upper and lower width. As a result, [33] and [34] show that adopting both concentrated windings and rectangular windings causes dead spaces to appear in the slot. To solve this problem, this paper first employs a special rectangular winding structure to improve the slot factor by eliminating the dead spaces that appear in the stator slot. However, although copper loss in rectangular windings

can be reduced by improving the slot factor, large eddy current loss occurs more easily to them due to the longer eddy current loop. Therefore, three improvements are proposed to reduce the windings eddy current loss.

Additionally, it should be noted that the objective of this chapter is an interior permanent magnet synchronous generator (IPMSG), it does not have a redundant heat dissipation system but only its shell to decrease system complexity and increase operational reliability. Therefore, windings loss should be reduced as much as possible to ensure that the IPMSG can operate continuously.

This chapter is organized as follows. FEM (Finite- Element Method) is used for discussion first, and then, a prototype machine is manufactured to verify the FEM results. Section 3.2 proposes the structure of the basic model employing special rectangular windings to eliminate the dead spaces in the stator slot. And Section 3.3 proposes three improvements to reduce windings eddy current loss. Moreover, in Section 3.4, a 3-step-skewed rotor structure is adopted to reduce cogging torque and discuss its influence on losses. Furthermore, three models adopting round windings are made and discussed for comparison in Section 3.5. Finally, a prototype machine is manufactured in Section 3.6 to verify the FEM results.

In addition, FEM is executed by using an electromagnetic field simulator (JMAG-designer ver. 20.0, JSOL CO., Ltd.). And the skin and proximity effects have been fully considered. Moreover, unless otherwise specified, the FEM results in this chapter are all obtained at the rated operating point by using a maximum efficiency control strategy.

## Section 3.2 Structure of basic model employing special rectangular windings

Table 3.1 shows the design specification of a high-torque IPMSM in this chapter. The outer diameter of the stator is 580 mm. And the rated rotational speed and torque are 2000 rpm and 1510 Nm, respectively. Fig. 3.1 shows the structures of the two basic models and the appearance of the special rectangular windings. As shown in Fig. 3.1(a), except for the turn of windings, Models A-1 and A-2 are identical. The windings are 24 turns for Model A-1, while Model A-2 has 8 turns. A disproportional airgap is adopted to suppress iron loss by suppressing *q*-axis magnetic flux fundamental component and the harmonic components of *dq*-axis [35]. Moreover, as shown in Fig. 3.1(b), Aster Windings, a special rectangular winding structure, is adopted to improve the stator slot space factor. Aster Windings is manufactured by Aster Co., Ltd, which have diff9erent cross-sectional shape but the same cross-sectional area for each turn. Aster Windings are employed for the basic two models. Because the dead spaces in the slots are significantly eliminated, the slot factor can be improved.

Table 3.1 Design specification

| Design specification | |
|---|---|
| Rated rotational speed [rpm] | 2000 |
| Rated torque [Nm] | 1510 |
| Rated capacity [kW] | 316.2 |
| Target efficiency [%] | ≥97 |
| Inverter voltage limitation [Vrms] | ≤400 |
| Stator core outer diameter [mm] | 580 |
| Airgap length [mm] | 1 |
| Poles/Slots | 24/36 |

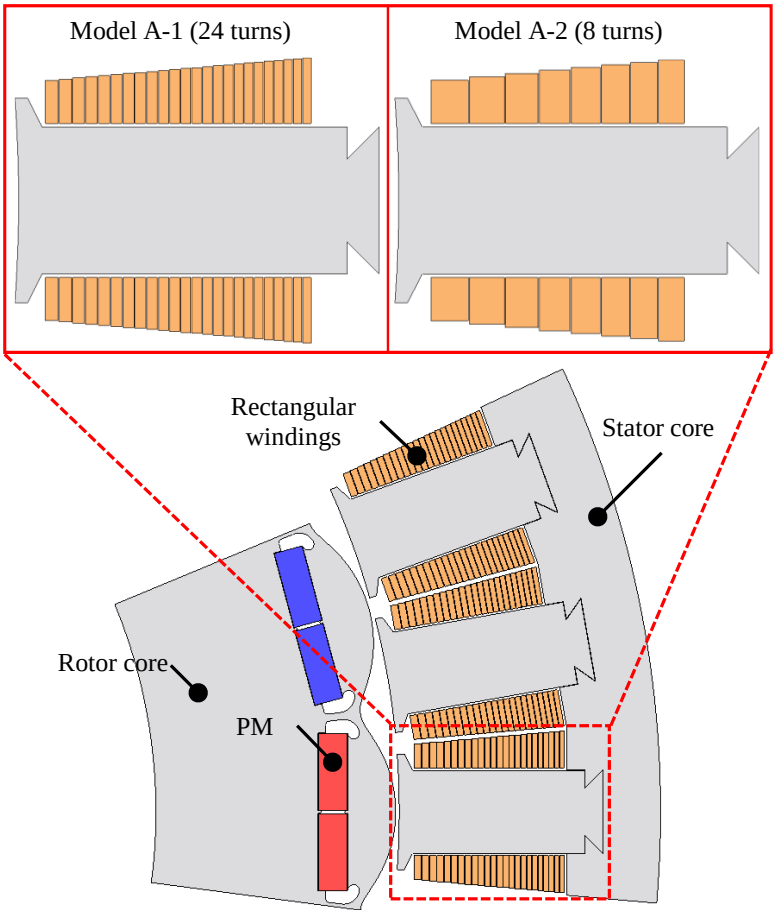


(a) Basic models

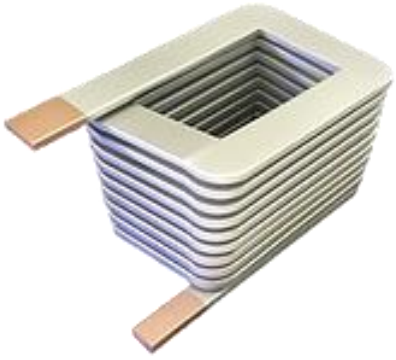

(b) Aster Windings

Figure 3.1 Structures of basic models and Aster Windings

However, compared with round windings, large eddy current loss occurs more easily in rectangular windings due to their longer eddy current loop. This also implies shortening the eddy current loop can reduce eddy current loss.

The magnetic flux passing through the windings is shown in Fig. 3.2, and it consists of two main components. $\psi_1$ is a portion of linkage magnetic flux between the stator and rotor that directly passes through the windings. $\psi_2$ is the magnetic flux that directly passes through the windings and across the adjacent teeth. The windings of Model A-1 are in the upper part of Fig. 3.2, while those of Model A-2 are in the lower part. When the dimension of one stator slot is determined, an increase in the turn of windings per slot can suppress the eddy current loss generated by the magnetic flux $\psi_2$ effectively because the cross-sectional area of each turn decreases. However, increasing the turn of windings will lead to an increase in voltage and a decrease in current for a specific operating point [36][37]. Although it is desirable to increase the turn of windings per slot as much as possible, it should be noted that the voltage should be less than or equal to 400 Vrms to ensure that the IPMSG can be easily driven by a mass-produced inverter. Additionally, the approaches to reduce the eddy current loss generated by the magnetic flux $\psi_1$ will be discussed in Section 3.3.

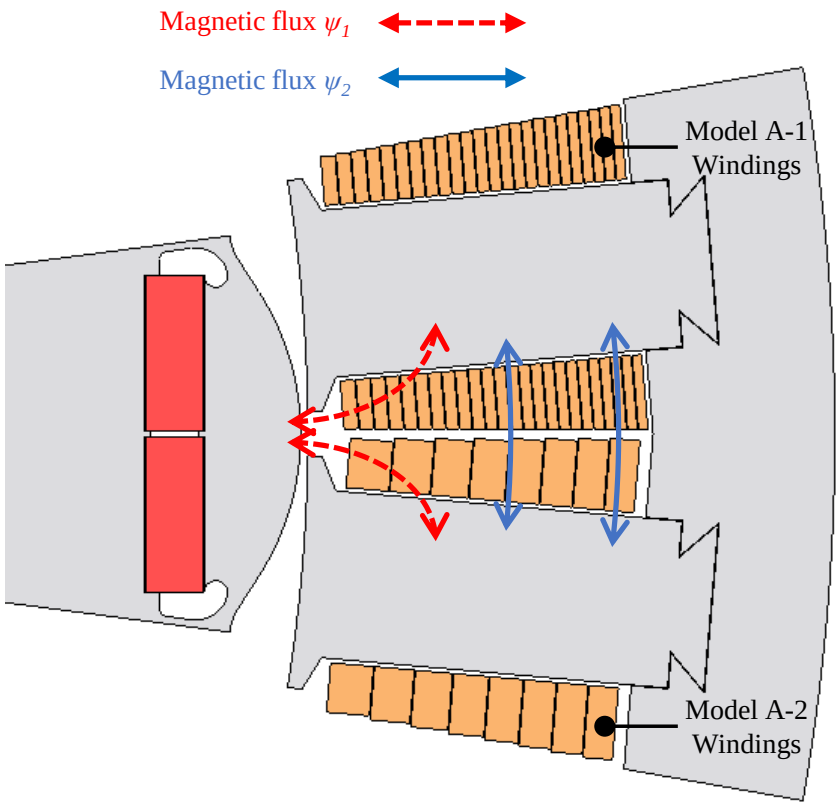


Figure 3.2 Magnetic flux passing through the windings

On the other hand, the voltage can also be reduced by increasing the parallel circle number of armature windings for a specific operating point. In other words, the IPMSG is desirable to have a pole-slot number combination that can achieve a higher parallel circle number. There are many pole-slot number combinations available for selection. Considering the design specification, a 28p-36s combination and a 24p-36s combination are suitable for the basic model. A 28p-36s model can be regarded as a parallel connection of two 14p-18s models, and the maximum parallel circle number of one 14p-18s model is 2. Therefore, the maximum parallel circle number of a 28p-36s combination is 4. At the same time, a 24p-36s model can be regarded as a parallel connection of twelve 2p-3s models. Therefore, the maximum parallel circle number of a 24p-36s combination is 12. As a result, a 24p-36s (2p-3s series) combination is selected for the two basic models to reduce voltage.

Table 3.2 shows the performances of the two basic models at the rated operating point. The stacked length is 240 mm. Due to employing Aster Windings, the slot space factor of the two basic models can reach up to 77%. As a result, the copper losses for Models A-1 and A-2 are all only 1.354 kW. It should be noted that the two models have the same copper loss because their slot factors and current density are identical. However, Model A-2 only has 8 turns in its windings, compared to the 24 turns in Model A-1. Therefore, Model A-2 has a longer eddy current loop for each turn, and the windings eddy current loss of Model A-2 is 32.327 kW, which is approximately 5.1 times that of the 6.317 kW in Model A-1. Moreover, although the rotor core iron loss and the PMs eddy current loss are almost unchanged, influenced by the large windings eddy current loss, the stator core iron loss in Model A-2 is 5.58% higher than that of Model A-1. Additionally, the effective voltage value is 398.8 Vrms in Model A-1. If a 28p-36s combination is adopted, due to the inverter voltage limitation, the cross-sectional area of each turn will be similar in size to that of Model A-2 because the maximum parallel circle number of armature windings is only one-third that of a 24p-36s combination.

As a result, Model A-1, hereafter referred as Model A, is chosen as the basic model. However, the windings eddy current loss of Model A still accounts for 48.51% of the total loss. And the efficiency of Model A is 95.89%, which does not satisfy the target efficiency of 97% in the design specification.

Table 3.2 Performances of basic models

| | Model A-1 | Model A-2 |
|---|---|---|
| Space factor[%] | 77 | 77 |
| Copper loss [kW] | 1.354 | 1.354 |
| Windings eddy current loss [kW] | 6.317 | 32.327 |
| Stator core iron loss [kW] | 4.598 | 4.855 |
| Rotor core iron loss [kW] | 0.542 | 0.543 |
| PMs eddy current loss [kW] | 0.212 | 0.210 |
| Total loss [kW] | 13.024 | 39.288 |
| Efficiency [%] | 95.89 | 87.59 |

## Section 3.2 Improvements to reduce windings eddy current loss

### Subsection 3.2.1 Removing a portion of windings

Fig. 3.3 shows the joule loss density distribution of windings for Model A at 0.1 rpm and 2000 rpm, respectively. And the windings joule loss is at its highest level at this moment. As shown in Fig. 3.3(a), the joule loss can be regarded as generated by copper loss entirely because the rotational speed is very slow. Although the instantaneous current of each parallel branch is 39.65 A at this moment, compared with the eddy current loss at 2000 rpm, the joule loss generated by copper loss is small. Therefore, it can be seen from Fig. 3.3(a) that the color of windings joule loss density distribution is almost purple. However, when it comes to Fig. 3.3(b), large joule loss generates due to the large eddy current loss, especially for the windings close to the inner side of the stator.

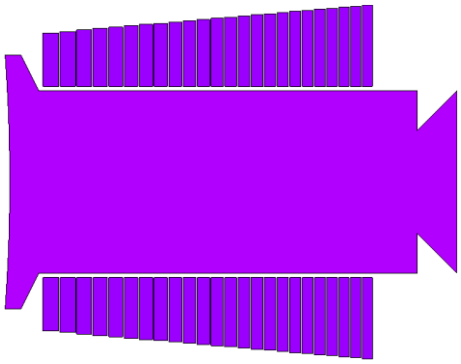

(a) 0.1 rpm

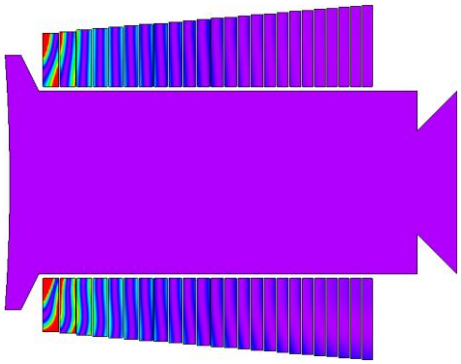

(b) 2000 rpm

Figure 3.3 Windings joule loss density distribution for Model A
(a) 0.1 rpm (b) 2000 rpm

Fig. 3.4 shows the naming convention of the windings and the distribution of eddy current loss for each turn. The coil closest to the inner side of the stator is named the 1st turn, while the coil closest to the stator yoke is named the 24th turn. The windings eddy current loss of the first 4 turns is 4.035 kW, which accounts for 63.88% of the total eddy current loss.

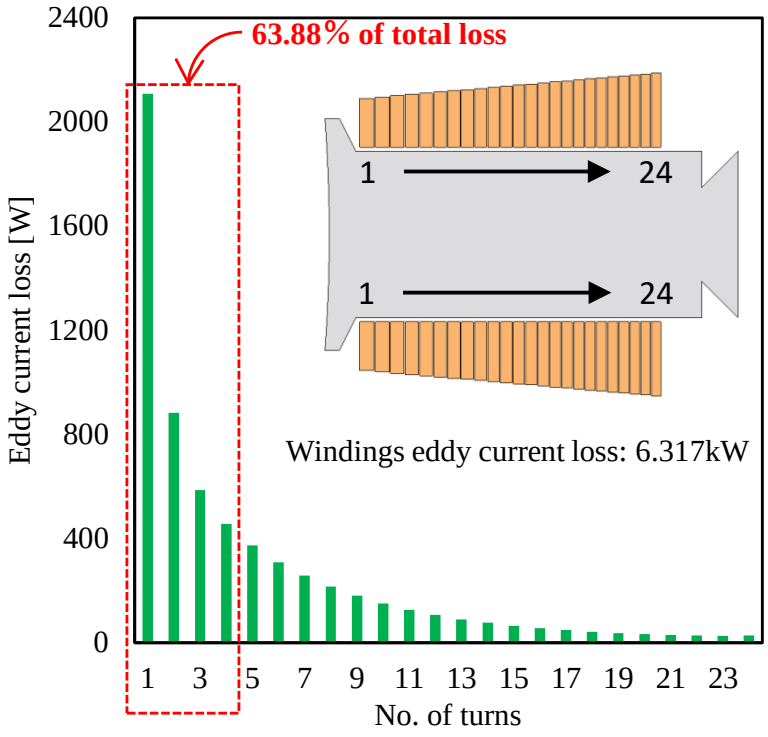


Figure 3.4 Naming convention of windings and distribution of eddy current loss for each turn

Therefore, as shown in Fig. 3.5, the first 4 turns in Model B have been removed. As a result, the copper loss increased while the eddy current loss decreased, and a tradeoff between the two losses is realized to reduce the total windings loss. The slot factor of Model B is 64%, which is still higher than common round windings models. Additionally, Fig. 3.6 shows the system used for the wind generator. The IPMSG is connected to the power system via one AC-AC inverter. Therefore, although the turn of windings in Model B decreased, the operating current and its phase angle can be controlled to make sure that the power out remains unchanged.

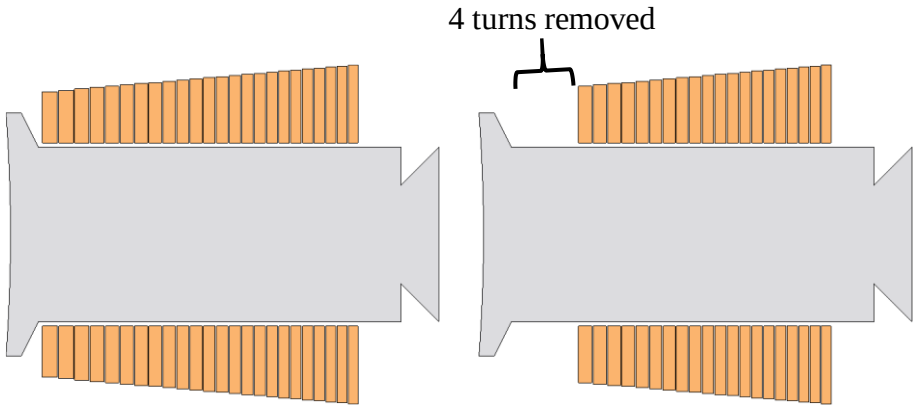


(a) Model A (b) Model B

Figure 3.5 Structures of Models A and B

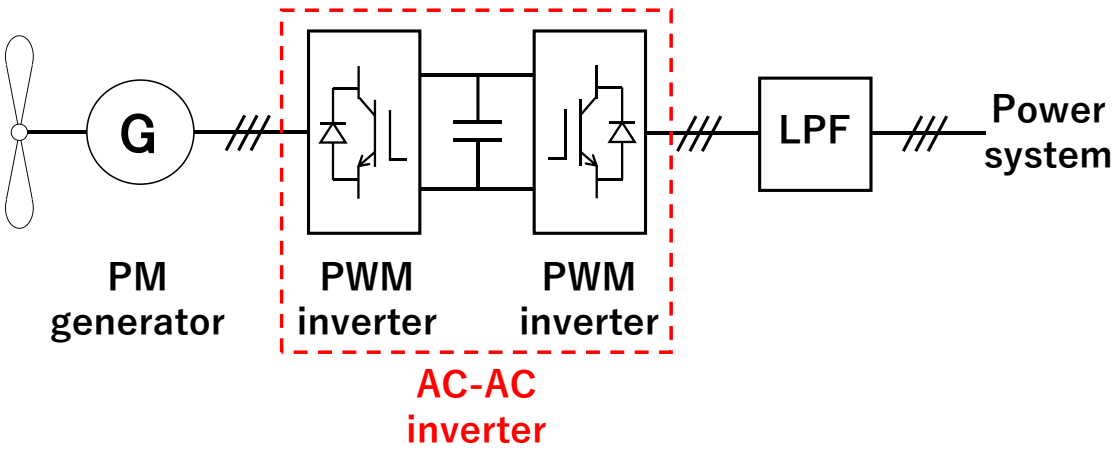


Figure 3.6 System used for the wind generator

Fig. 3.7 shows the loss comparison between Models A and B. Because the first 4 turns have been removed compared with Model A, the copper loss increases by 18.66%, while the windings eddy current loss decreases by 49.63%, and other losses are almost unchanged. As a result, the total loss in Model B is reduced significantly by 21.74% compared with Model A. Model B has an efficiency of 96.77%, which is 0.88% higher than that of Model A.

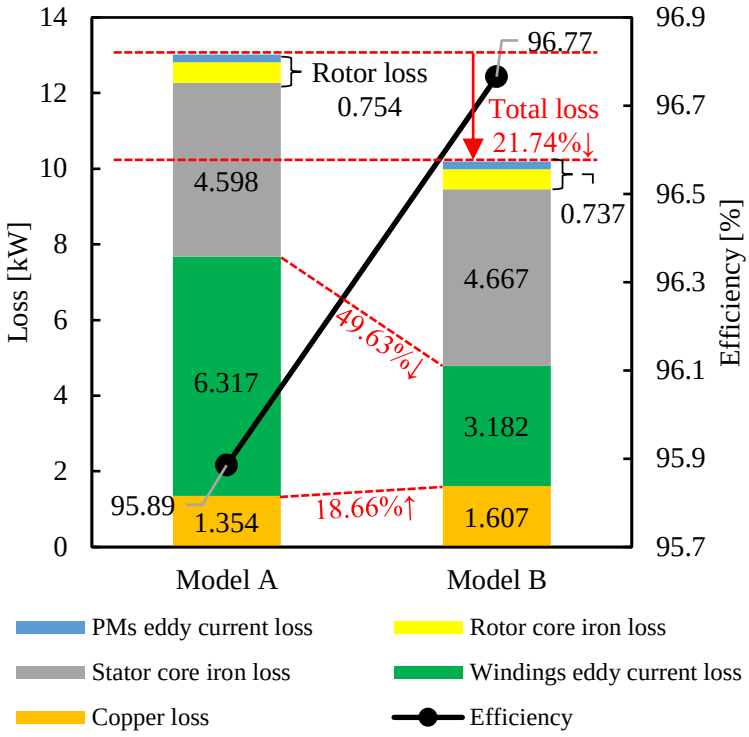


Figure 3.7 Loss comparison between Models A and B

### Subsection 3.2.2 Adjusting tooth-tip shape

Fig. 3.3 illustrates that the windings close to the inner side of the stator generate a significant eddy current loss. The magnetic flux in the IPMSG is expected to be concentrated in ferromagnetic materials. However, the magnetic permeability of ferromagnetic materials around the tooth-tip decreases under the influence of the magnetic saturation, which makes it difficult for magnetic flux to pass and results in an increase in the magnetic flux passing through the windings. On the other hand, by appropriately shaping the tooth-tip, which can suppress the magnetic flux flowing into it, the magnetic saturation around the tooth-tip can be mitigated. As a result, both the magnetic flux $\psi_1$ and $\psi_2$ shown in Fig. 3.2 can be suppressed. Therefore, suppressing the magnetic flux that flows into the tooth-tip and widening the magnetic path of the tooth-tip are discussed in this section to mitigate the magnetic saturation. To achieve this purpose, three dimensions *l1*, *l2*, and *l3* of the tooth-tip, which are shown in Fig. 3.8, have been discussed to further reduce the windings eddy current loss.

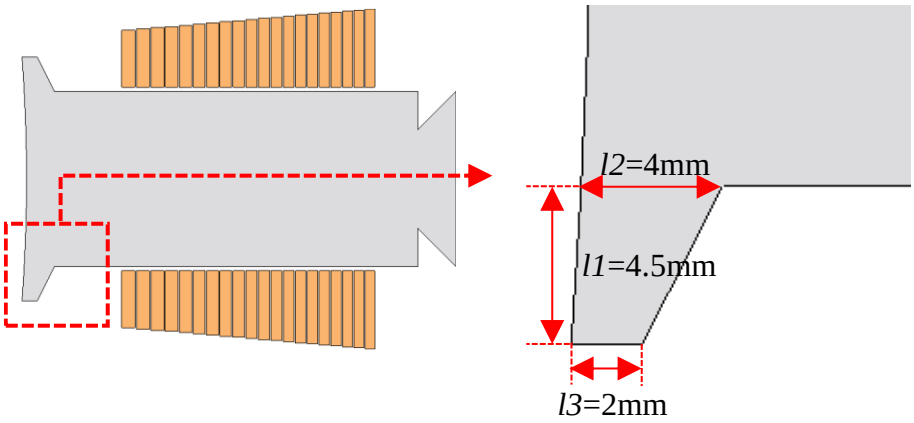


(a) Model B

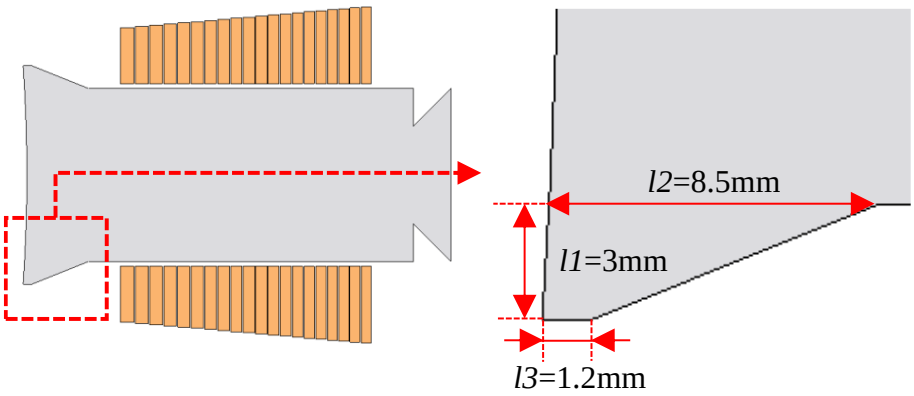


(b) Model C

Figure 3.8 Structures of Models B and C

The main components of the magnetic flux that flows into the tooth-tip are a portion of the interlinkage flux between the rotor and stator and a portion of the magnetic flux that flows across the adjacent teeth. Because the magnetic permeability of air is much greater than that of ferromagnetic materials, magnetic flux flowing into the tooth-tip can be suppressed by reducing *l1* and *l3*, and the width of the magnetic path around the tooth-tip can be widened by increasing *l2*. Due to the mitigation of the magnetic saturation, a portion of the magnetic flux that previously passed through the windings can now flow into the stator via the tooth tip. Moreover, it should be noted that the width of the interlinkage magnetic path between the stator and rotor will be narrowed by a too small *l1* or *l3*, which will also result in an increase in the magnetic flux passing through the windings, and copper loss will also increase at the same time.

In addition, by decreasing *l1*, a portion of the magnetic flux flowing across the adjacent teeth can be suppressed. This portion of the magnetic flux does not interlink with the rotor, which only increases copper and iron losses and does not contribute to power out. Moreover, the magnetic path around the tooth-tip can be widened by increasing *l2*. As a result, copper loss can be reduced because the operating current that generates the same magnetic flux density in the airgap will be smaller.

The 3 dimensions have been changed from *l1* = 4.5 mm, *l2* = 4 mm, *l3* = 2 mm in Model B, to *l1* = 3 mm, *l2* = 8.5 mm, *l3* = 1.2 mm in Model C. The magnetic flux density distribution in Models B and C are shown in Fig. 3.9, and their iron loss density distribution are shown in Fig. 3.10. According to Fig. 3.9, the magnetic saturation around the tooth-tip has been obviously mitigated by adjusting the tooth-tip shape. As a result, it can be seen from Fig. 3.10 that iron loss around the tooth-tip has also been reduced. Moreover, Fig. 3.11 compares the losses of the first 5 turns for Models B and C. The eddy current and copper losses of each turn in Model C have both been reduced in comparison to Model B.

Fig. 11 shows the loss comparison between Models B and C. Model C has a 5.05% reduction in winding eddy current loss and a 4.68% reduction in stator core iron loss when compared to Model B. Moreover, the copper loss in Model C also decreases by 4.39%. As a result, the efficiency of Model C is 96.88%, which is 0.11% higher than that of Model B. Although the efficiency of Model C is only increased by 0.11%, the total windings loss of Model C is 4.558 kW, which is 4.82 % lower than the 4.789 kW in Model B and cannot be ignored for the IPMSG rated at 316.2 kW because there is no redundant heat dissipation system but only its shell for heat dissipation.

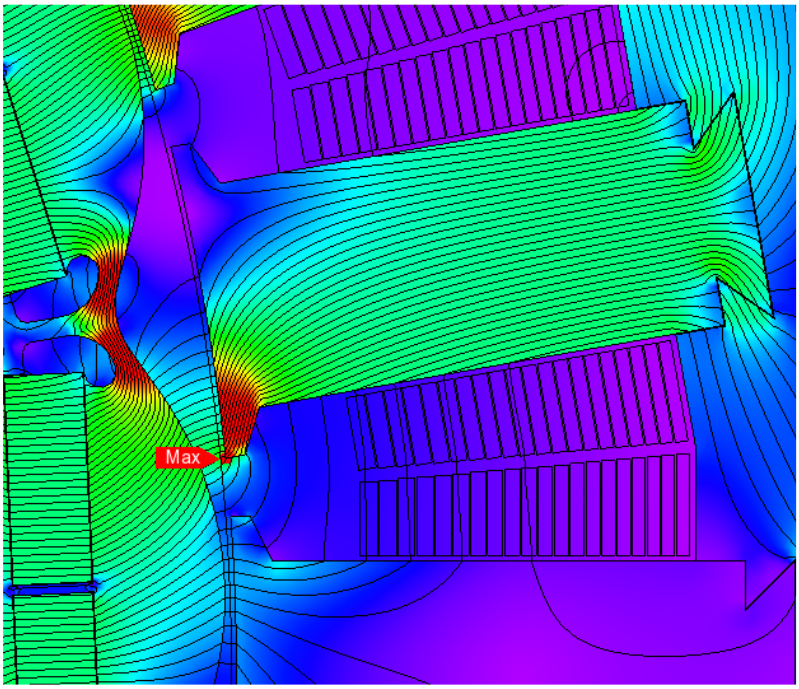


(b) Model B

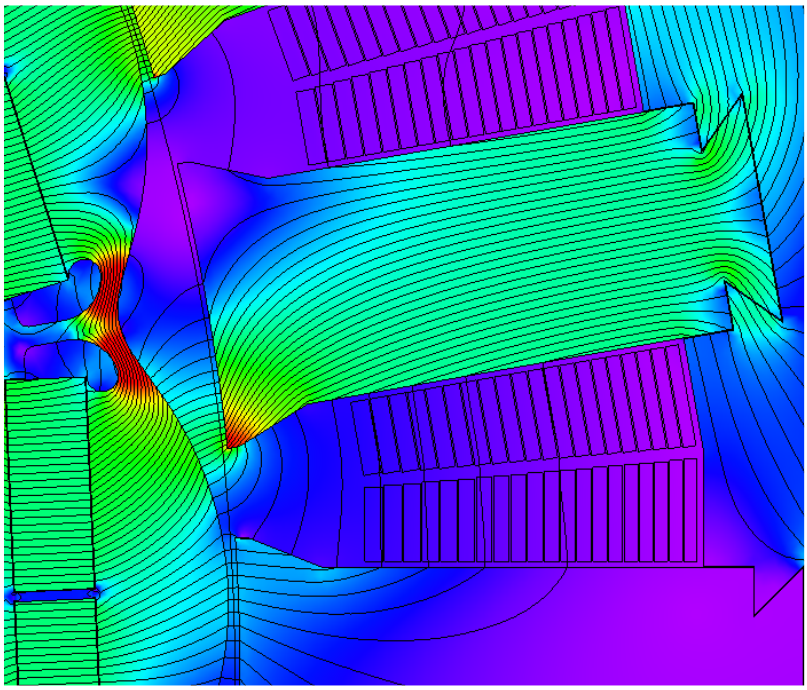


(b) Model C

Figure 3.9 Magnetic flux density distribution in Models B and C

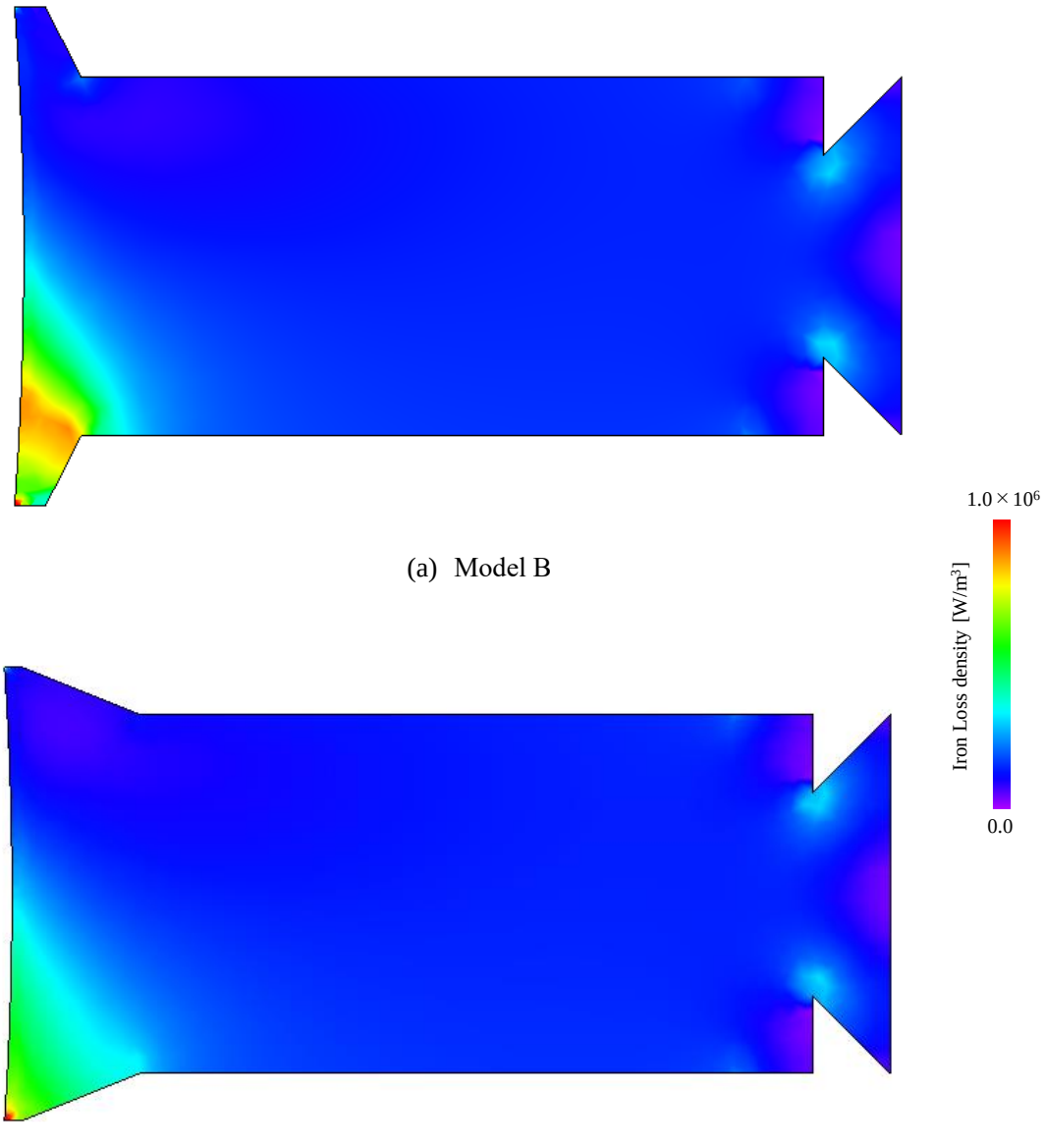


(a) Model B

(b) Model C

Figure 3.10 Iron loss distribution in Models B and C

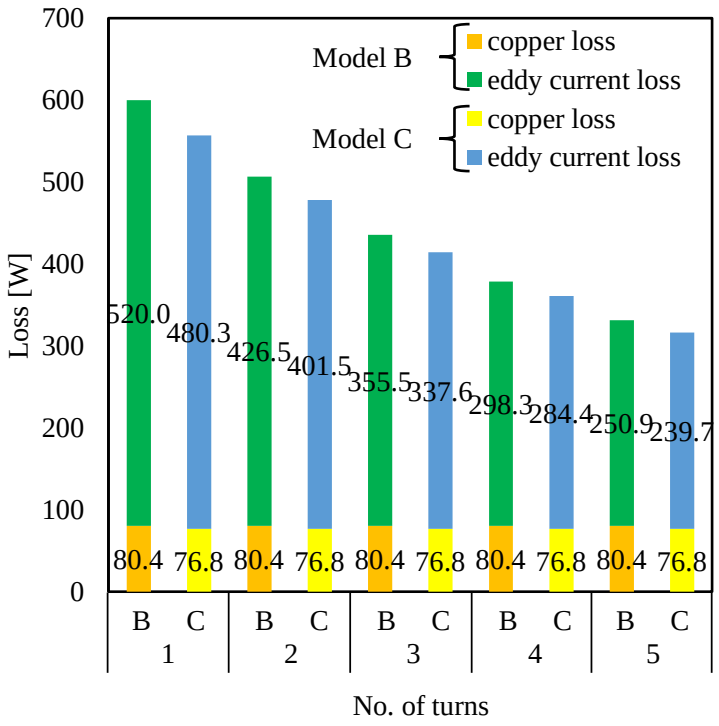


Figure 3.11 Loss comparison of the first 5 turns between Models B and C

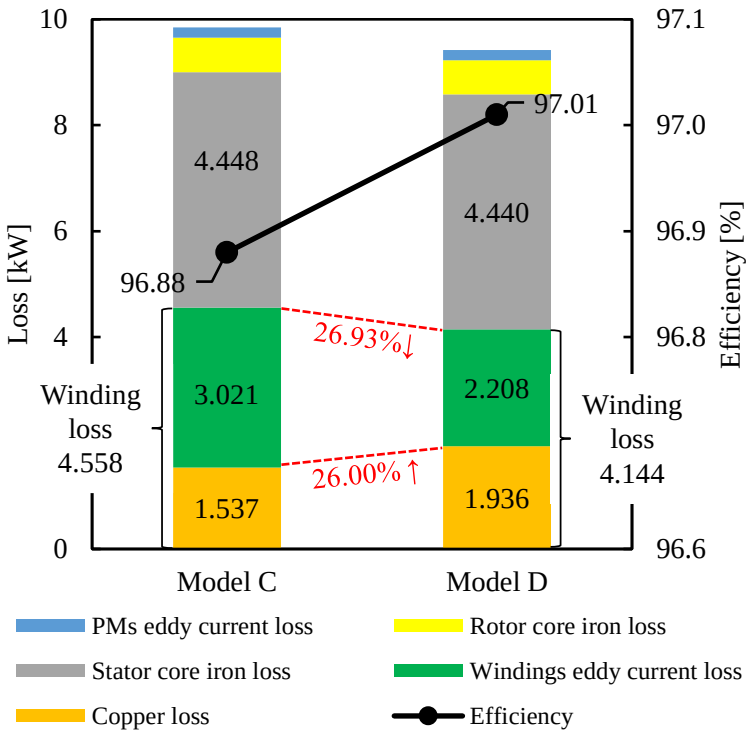


Figure 3.12 Loss comparison between Models C and D

### Subsection 3.2.3 Replacing a portion of windings with aluminum

The material of copper has been widely used for windings in high performance IPMSMs to reduce copper loss due to their low electrical conductivity. However, on the other hand, large windings eddy current loss occurs more easily to the windings with low electrical conductivity, especially in rectangular windings. Compared with copper, the electrical conductivity of aluminum is larger. Adopting aluminum windings will result in a higher copper loss but a lower eddy current loss. To realize a tradeoff between eddy current and copper losses to minimize total loss, replacing a portion of windings with aluminum is discussed in this section.

As mentioned earlier, significant eddy current loss generates more easily in the windings close to the inner side of the stator. Therefore, as shown in Fig. 3.13, a portion of the copper windings close to the inner side of the stator in Model D have been replaced with aluminum in comparison to Model C. Fig. 3.14 shows the calculation results for Models C and D. Eddy current loss and electrical resistivity are inversely proportional to each other when the operating current is the same, while copper loss and electrical resistivity are directly proportional. Consequently, using the losses of each turn in Model C, it is simple to calculate the copper and eddy current losses in Model D. The abscissa represents the turn of aluminum windings in Model D. With the turn of aluminum windings increases, the copper loss increases while the eddy current loss decreases. As a result, when the first 9 turns are replaced by aluminum, the windings total loss reaches a minimum value, which is 4085.46 W.

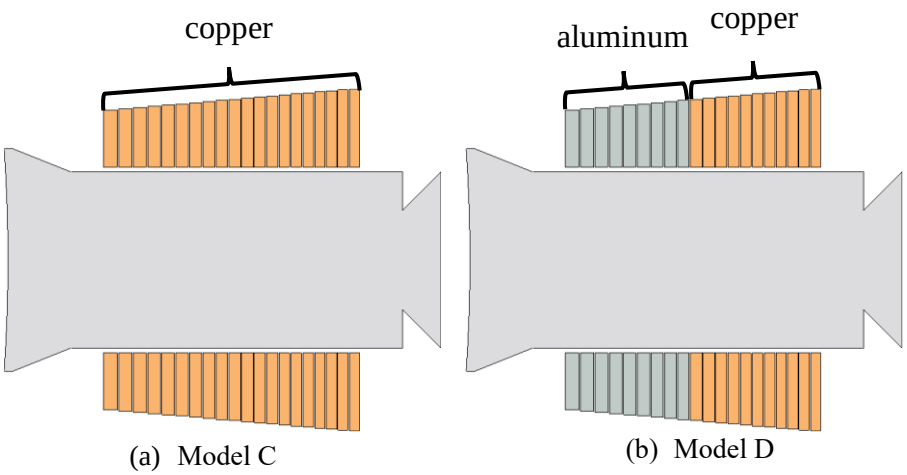


Figure 3.13 Structures of Models C and D

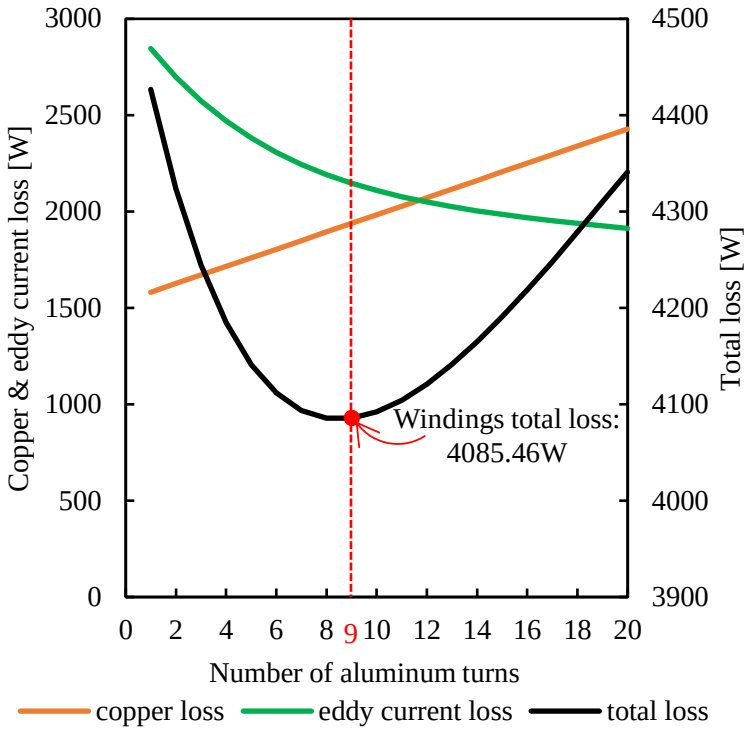


Figure 3.14 Calculation result of adopting aluminum windings

2D-FEM has also been used to verify the calculation results. Fig. 3.15 shows the loss comparison between Models C and D. Compared with Model C, the copper loss in Model D increases by 26.00% while the windings eddy current loss decreases by 26.93% because the first 9 turns have been replaced by aluminum windings. As a result, the windings total loss in Model D decreases from 4.558 kW to 4.144 kW while other losses are almost unchanged. And the error between 2D-FEM results and the calculation results is only 1.43%. The efficiency of Model D is 97.01%, which satisfied the target efficiency of 97% in the design specification.

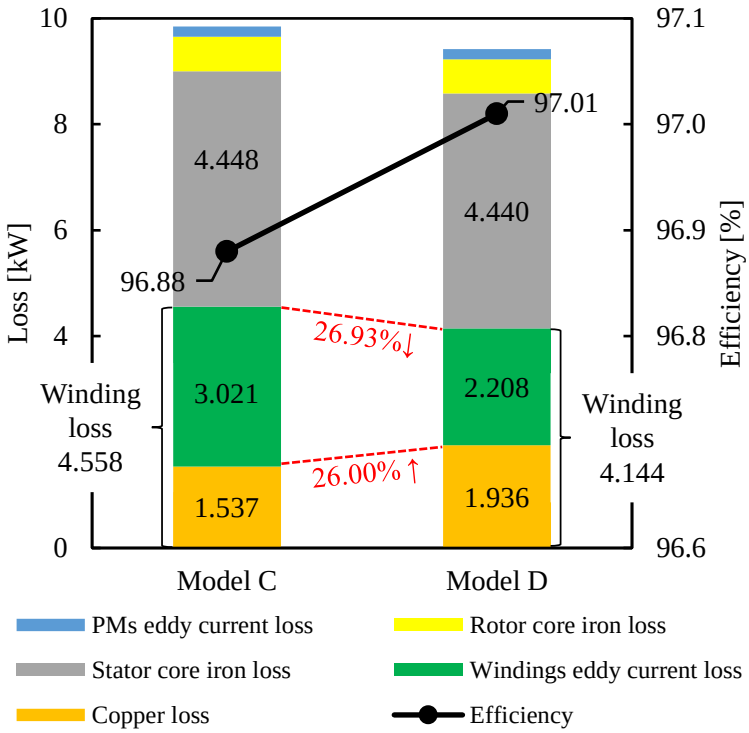


Figure 3.15 Loss comparison between Models C and D

## Section 3.3 Influence of adopting a step-skewed structure

Although the efficiency of Model D satisfied the target efficiency, high cogging torque was generated because a 24p-36s (2p-3s series) combination was adopted. High cogging torque makes it difficult for wind generator blades to rotate, especially in light winds. To lower the start-up wind speed, as shown in Fig. 3.16, a 3-step-skewed rotor structure was adopted in Model E to reduce cogging torque. In general, adopting a step-skewed rotor structure will lead to a decrease in power output. Additionally, heat dissipation also should be considered. Therefore, to keep the current density and power output unchanged, the stacked length is increased from 240 mm in Model D to 255 mm in Model E. Moreover, considering the end leakage of rotor and the axial flux interaction between adjacent rotor steps, the lengths of the middle-step and the side-step in Model E are set to 82 mm and 86.5 mm respectively to achieve the smallest cogging torque [38].

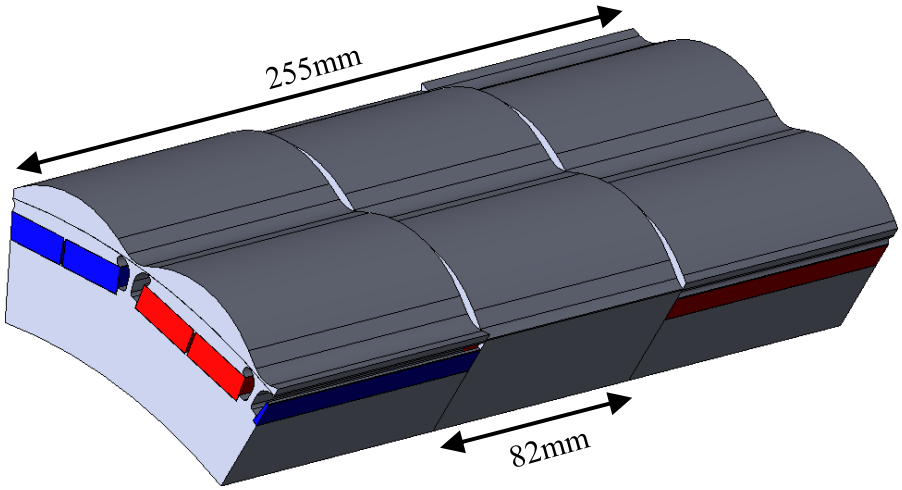


Figure 3.16 Loss comparison between Models C and D

Fig. 3.17 shows the mesh of the coil in Model E. The mesh in coil ending and the alternation of skew-steps are more accurate take the influence of leakage flux into account.

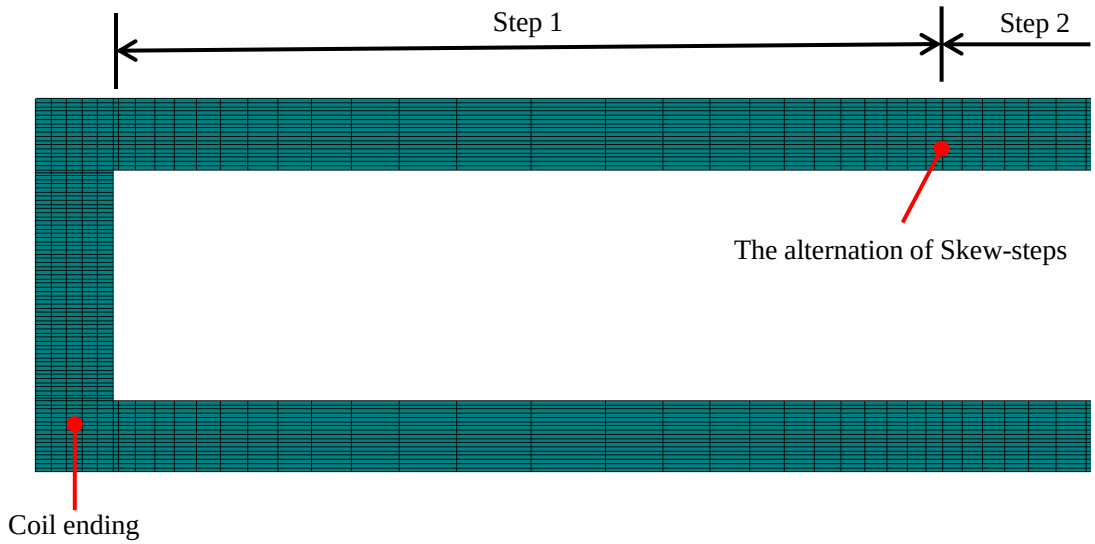


Figure 3.17 Mesh of the coil in Model E

Fig. 3.18 shows the comparison of cogging torque between Models D and E. Compared with Model D, the peak-to-peak cogging torque in Model E significantly decreases from 166.04 Nm to 11.34 Nm. Furthermore, to evaluate the influence of adopting the 3-step-skewed structure on windings eddy current loss. Fig. 3.19 shows the loss comparison of all models. The increase in stacked length in Model E causes the copper loss to increase from 1.936 kW to 2.168 kW in comparison to Model D because the current density is unchanged. Additionally, the windings eddy current loss of Model E is 2.111 kW, which is almost unchanged from that of Model D. As a result, adopting a step-skewed structure can be considered to have almost no influence on the eddy current loss of the windings.

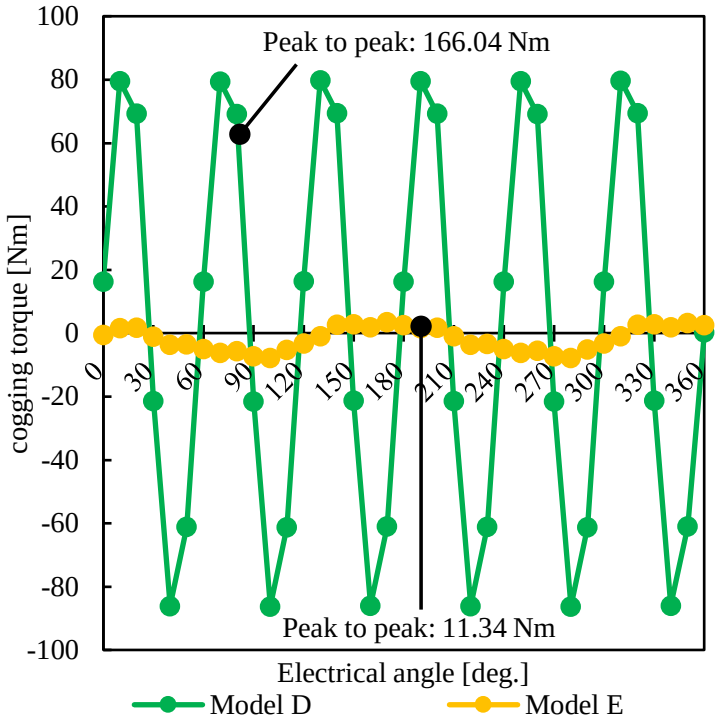


Figure 3.18 Comparison of cogging torque between Models D and E

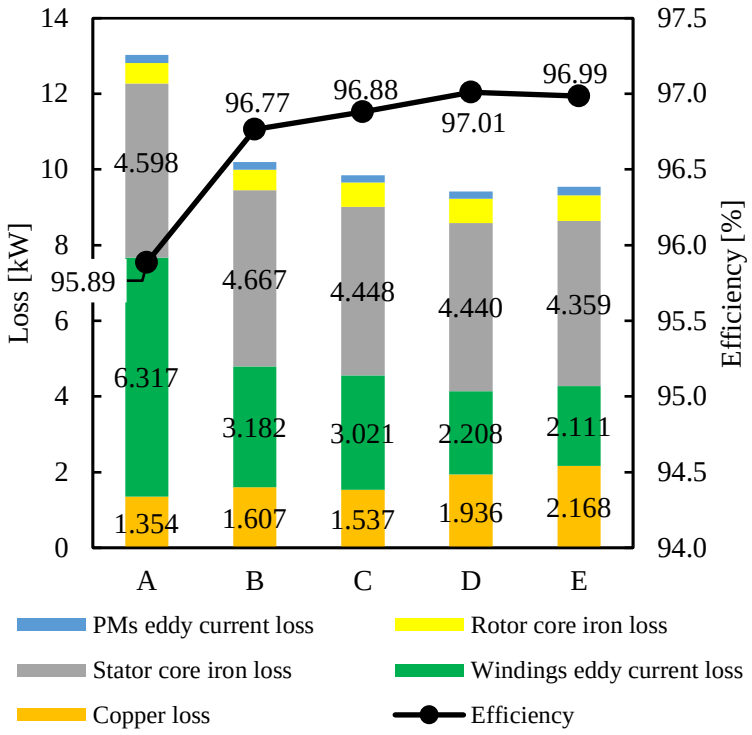


Figure 3.19 Loss comparison of all models

## Section 3.4 Compared with round windings models

In this section, three models adopting round windings are made for comparison to further evaluate the performances of the proposed model. Fig. 3.20 shows the windings of Model D and three round windings models. 2D-FEM is used in this section to save computation time. As was mentioned in Section 3.2, the eddy current loss of windings can be reduced by shortening the current loop. And when the dimension of one stator slot is determined, the eddy current loop for each turn can be shorten by increasing the turn of windings per slot. However, this approach will also result in an increase in voltage. Therefore, considering the inverter voltage limitation, the three round windings models all have 20 turns per slot, which is the same as Model D. On the other hand, parallel strands can be used to reduce the cross-sectional area of each strand while keeping the turn of windings unchanged. As seen in Fig. 3.20, although all three round windings models have 20 turns per slot, the number of parallel stands for each turn varies. A model without parallel strands is called Model F-1. For each turn, Model F-2 has two parallel strands. A model with three parallel strands for each turn is Model F-3. Additionally, the slot factors of the three models adopting round windings are all around 44%, which is a typical value for round windings.

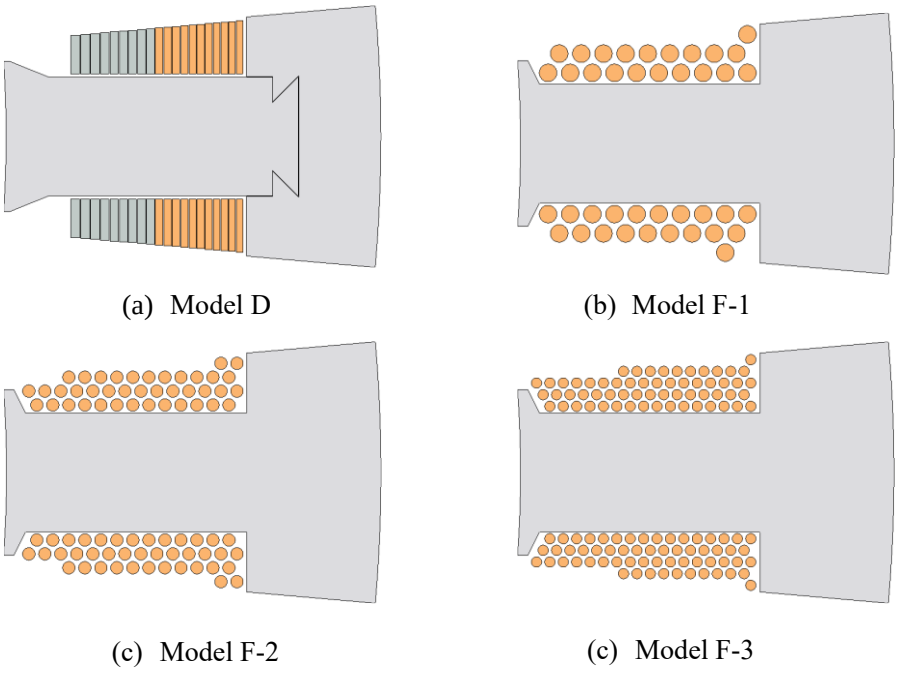

(a) Model D (b) Model F-1

(c) Model F-2 (c) Model F-3

Figure 3.20 Windings of Model D and three round windings models

The loss comparison between Model D and the three round windings models is shown in Fig. 3.21. The windings eddy current loss of Model F-1 is 6.380 kW, which is even larger than the 6.317 kW in Model A. The windings eddy current loss decreases with the increase in the number of parallel strands for each turn, while other losses remain almost unchanged. Moreover, the copper losses of the three round winding models are all larger than that of Model D because of their lower slot factors and larger winding end dead spaces. The windings eddy current loss of Model F-3 is 2.552 kW, which is still 15.58% higher than the 2.208 kW of Model D. And the efficiency of Model F-3 is 96.75%, which does not satisfy the target efficiency of 97% in the design specifications. It should be noted that round windings without parallel strands can be reeled simply by a winding machine. However, when parallel strands are adopted, the electromotive force of each strand varies depending on where it is located in the stator slot. As a result, circulating current is generated in parallel strands, which causes additional loss. Although circulating current can be reduced by methods such as transposed strands, these approaches always increase manufacturing cost [39][40].

Furthermore, Table 3.3 compares the usage of copper and aluminum in windings. Because of larger slot factors, the usage of copper in Models A and B are 58.72 kg and 49.94 kg, respectively, which are all larger than the 32.44 kg in Model F, which adopts round windings. However, due to adopting 2.20 kg aluminum windings, the usage of copper in Model D is 27.05 kg, which is less than that of Model F. Because aluminum is cheaper than copper, compared with the three rounds windings models, manufacturing costs can also be cut by adopting a portion of aluminum windings in Model D.

As a result, the proposed model can still achieve higher efficiency while cutting manufacturing costs when compared to the three round winding models. Moreover, because the rectangular windings in Model D have a better heat dissipation and lower windings losses, the heat dissipation can also be improved compared to the round windings models.

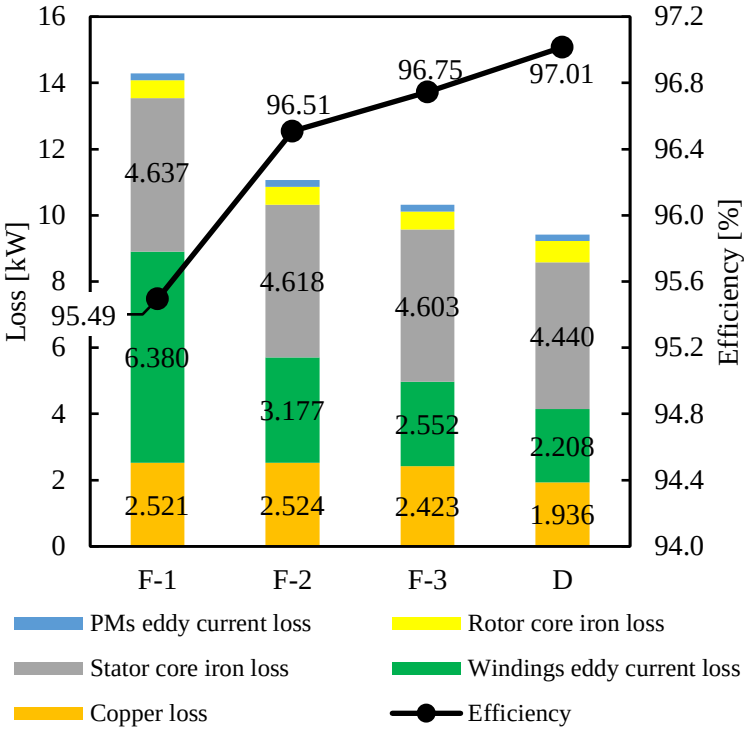


Figure 3.21 Loss comparison between Model D and three round windings models

Table 3.3 Usage of copper and aluminum in windings

| Model | A | B | D | F |
|---|---|---|---|---|
| Copper weight [kg] | 58.72 | 48.94 | 27.05 | 32.44 |
| Aluminum weight [kg] | 0.00 | 0.00 | 2.20 | 0.00 |
| Total weight [kg] | 58.72 | 48.94 | 29.25 | 32.44 |

## Section 3.5 Experimental verification

In this section, a prototype machine of Model E is manufactured to verify the 2D-FEM results. The appearance of the prototype is shown in Fig. 3.22. Aster Windings used for the prototype is shown in Fig. 3.22(a). The first 9 turns are made of aluminum, and the last 11 turns are made of copper. Fig. 3.22(b) shows Aster Windings assembled on the stator core. It can be seen that the windings have different cross-sectional shapes but the same cross-sectional area for each turn, and the windings gradually become flat when they are close to stator yoke. Fig. 3.22(c) shows the appearance of the prototype.

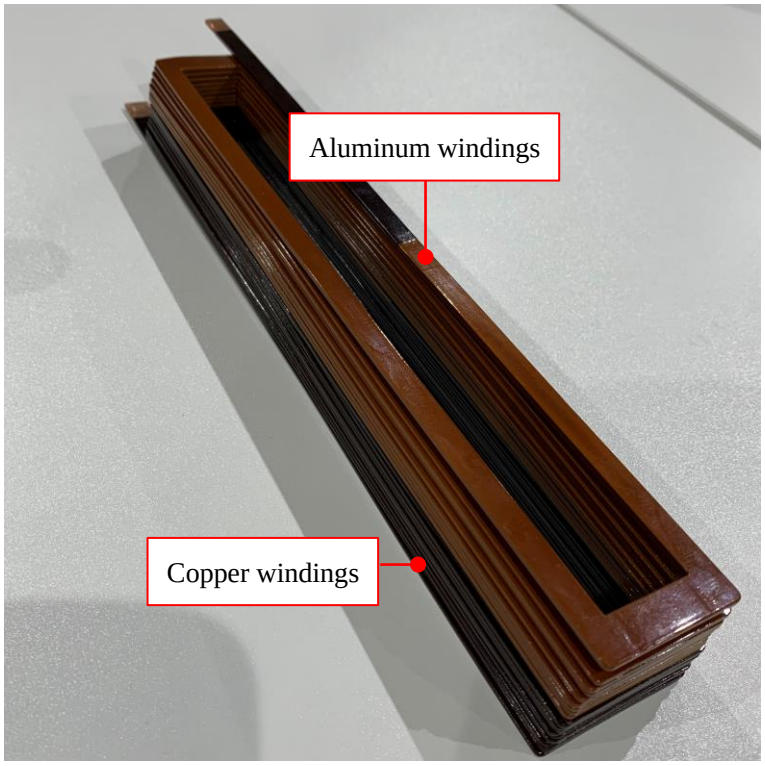


Figure 3.22 Appearance of prototype machine

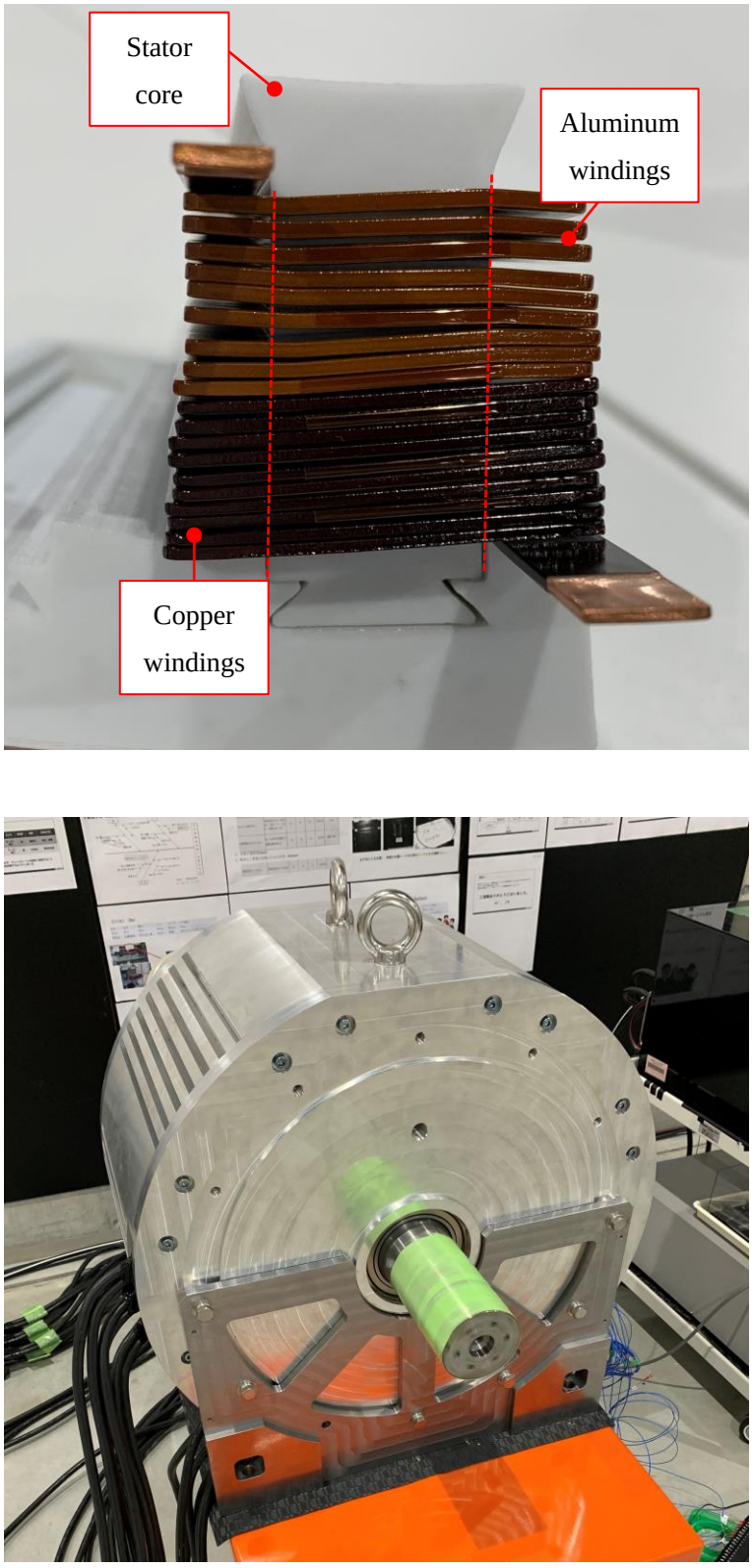


Figure 3.23 Appearance of prototype machine

To save computation time, 2D-FEM is also used to compare with the experimental results. Different from the 2D-FEM models in the previous sections, the 3-step-skewed structure in Model E has been considered. The 2D-FEM results in this section are obtained by superimposing the results of three 2D models which have the same stacked length and step-skewed angle as the three skew steps of Model E.

Fig. 3.24 shows the waveforms of back electromotive forces (b-EMFs) at 2000 rpm. And Table IV shows their fundamental components. Because the rotor end leakage and the axial flux interaction between adjacent rotor steps have been considered, the fundamental component of the b-EMF in the 3D-FEM (Model E) model is smaller than that of the 2D-FEM model [38]. Moreover, it should be noted that the fundamental component of the b-EMF in the prototype is larger than both the 2D-FEM model and the 3D-FEM model.

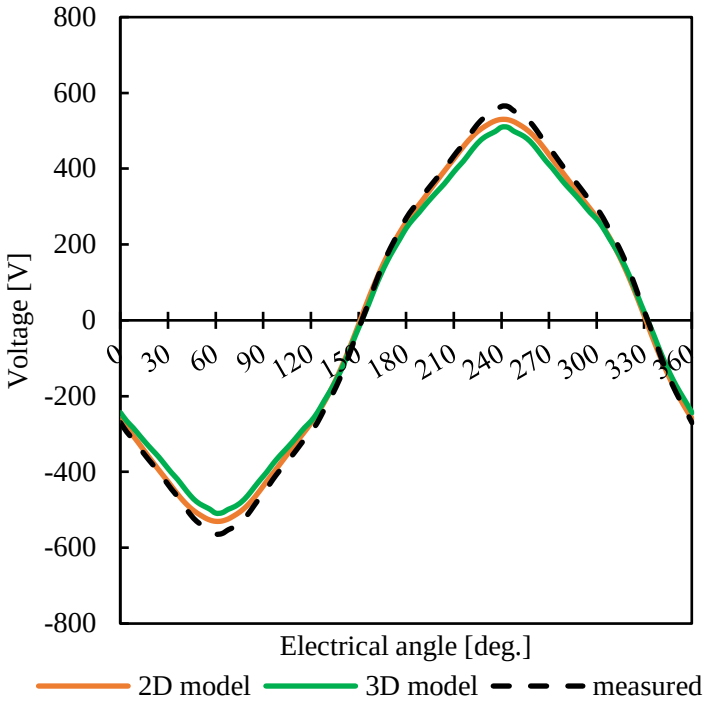


Figure 3.24 Waveforms of back electromotive force (b-EMF)

Table 3.4 Fundamental component of B-EMF

| | Fundamental component of b-EMF [Vrms] |
|---|---|
| 2D model | 363.7 |
| 3D model | 342.6 |
| Measured | 379.5 |

Fig. 3.25 shows the average torque variation with current phase angle at the 1600 rpm and 250 Arms operating point. The manufactured results are in good agreement with the FEM results. Because the b-EMF fundamental component of the prototype is the largest, it should be noted that the average torque of the prototype has the highest absolute value.

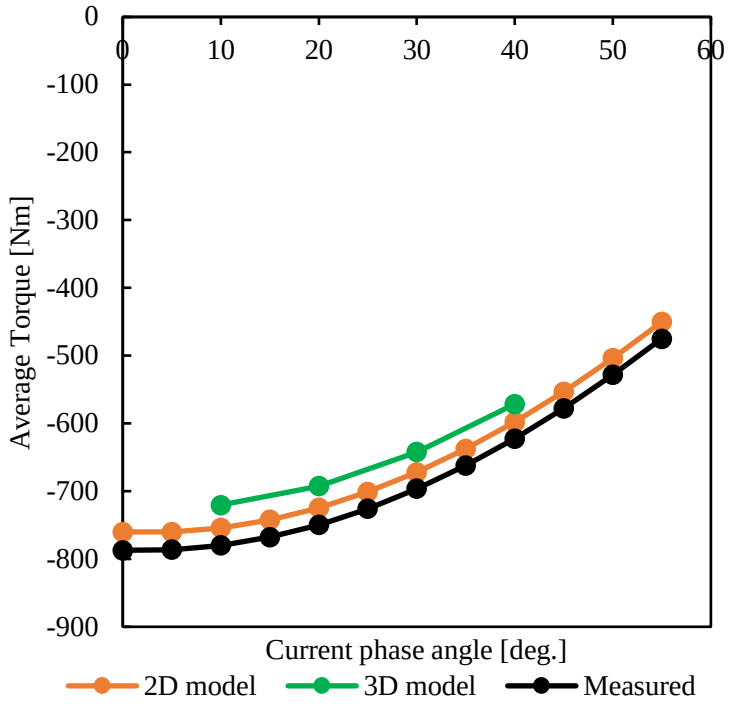


Figure 3.25 Average Torque varies with current phase angle at 1600 rpm and 250 Arms

The prototype has the largest efficiency when the current phase angle is 35 deg at the 1600 rpm and 250 Arms operating point. Therefore, the loss comparison shown in Fig. 3.26 is at the operating point of 1600 rpm, 250 Arms, and current phase angle 35 deg. The total loss of the prototype is not significantly different from the 3D-FEM model. Due to the largest b-EMF fundamental component, the total loss of the 2D-FEM is highest. The efficiency of the prototype at this operating point is 97.25 %, which is larger than the

FEM results.

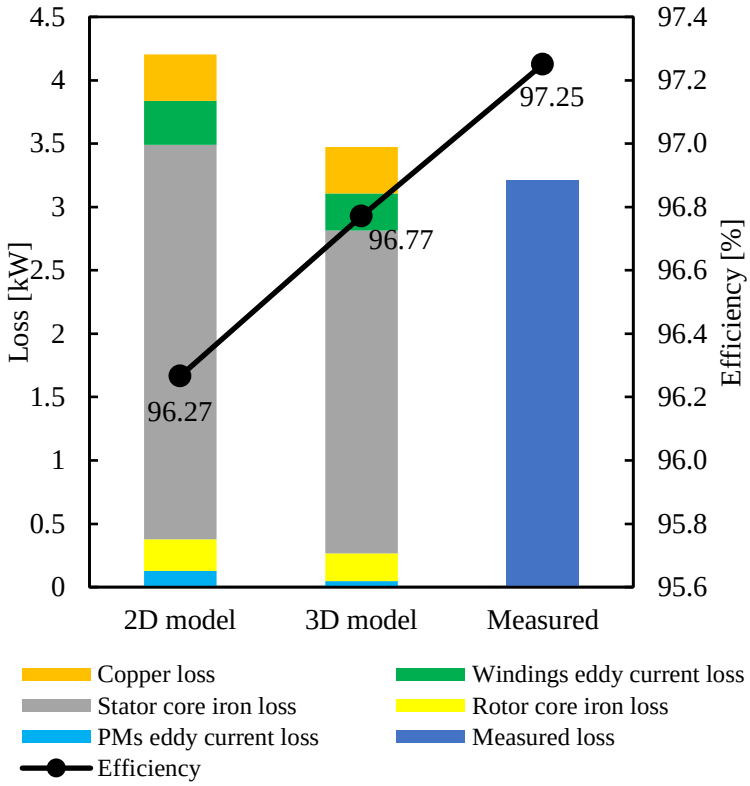


Figure 3.26 Loss comparison at the operating point 1600rpm, 250 Arms and current phase angle 35deg

Fig. 3.27 shows the measured efficiency map of the prototype. The operating area was not completely measured because the maximum torque capacity of the test platform was not high enough. The maximum measured efficiency can exceed 97.5 %, which is higher than that of the FEM results.

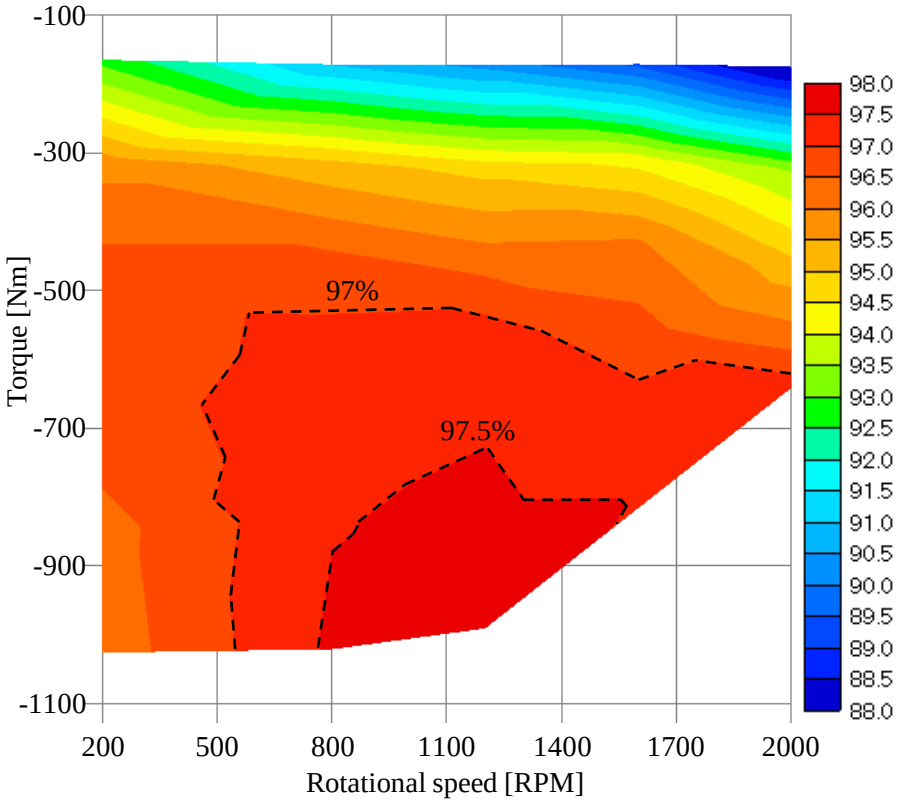


Figure 3.27 Loss comparison at the operating point 1600rpm,
250 Arms and current phase angle 35deg

## Section 3.6 Conclusion of Topic II

This chapter proposed a high-torque IPMSG adopting concentrated windings with special rectangular windings used for a wind generator. Three improvements have been discussed to reduce windings eddy current loss. Among them, removing a portion of windings and replacing a portion of windings with aluminum have been discussed to realize a tradeoff between eddy current and copper losses. And adjusting the tooth-tip shape has been discussed to suppress the magnetic flux passing through the windings by mitigating magnetic saturation around the tooth-tip. Moreover, a 3-step-skewed rotor structure has been adopted to reduce cogging torque. And FEM results show that adopting a step-skewed structure can be considered to have almost no influence on the eddy current loss of the windings. To further evaluate the performances of the proposed model, three models adopting round windings have been made and discussed. And FEM results show that the proposed model can still achieve higher efficiency while cutting manufacturing costs when compared to the three round winding models. Finally, a prototype machine has been manufactured to verify the FEM results. The experimental results show that the efficiency of the prototype can exceed 97.5%. In conclusion, a high efficiency IPMSM with high slot factor and good heat dissipation used for a wind generator has been realized in this chapter.

## Section 3.7 Data of Topic II

Table 3.5 Data of rectangular windings models (Rated operating point)

| | A | B | C | D | E |
|---|---|---|---|---|---|
| Rotational speed [rpm] | 2000 | 2000 | 2000 | 2000 | 2000 |
| Winding resistance (one phase) [ohm] | 0.00172 | 0.00143 | 0.00143 | 0.00181 | 0.00190 |
| Operating current [Arms] | 512.856 | 611.196 | 597.636 | 597.636 | 616.512 |
| Current density[Arms/mm$^2$] | 3.189 | 3.801 | 3.717 | 3.717 | 3.834 |
| Current phase angle [deg.] | 35 | 35 | 35 | 35 | 35 |
| Average torque [Nm] | 1511.345 | 1504.773 | 1506.954 | 1506.994 | 1511.061 |
| Maximum torque [Nm] | 1624.839 | 1614.341 | 1660.957 | 1661.028 | 1579.817 |
| Minimum torque [Nm] | 1386.113 | 1384.655 | 1344.676 | 1344.691 | 1448.343 |
| Torque ripple [%] | 15.80 | 15.26 | 20.99 | 20.99 | 8.70 |
| Line voltage peak value [V] | 622.306 | 533.569 | 507.323 | 507.293 | 499.662 |
| Line voltage fundamental wave effective value [Vrms] | 393.706 | 335.412 | 333.618 | 333.518 | 345.132 |
| THD [%] | 16.09 | 14.95 | 15.77 | 15.77 | 8.28 |
| Copper loss [kW] | 1.354 | 1.607 | 1.537 | 1.936 | 2.168 |
| Total iron loss [kW] | 11.670 | 9.303 | 8.307 | 7.485 | 7.373 |
| Stator core iron loss [kW] | 4.598 | 4.667 | 4.448 | 4.440 | 4.359 |
| Rotor core iron loss [kW] | 0.542 | 0.536 | 0.646 | 0.646 | 0.675 |
| Magnet eddy current loss [kW] | 0.212 | 0.244 | 0.192 | 0.192 | 0.229 |
| Windings eddy current loss [kW] | 6.317 | 3.857 | 3.021 | 2.208 | 2.111 |
| Input [kW] | 303.511 | 315.159 | 305.772 | 306.203 | 306.934 |
| Output [kW] | 316.535 | 326.069 | 315.616 | 315.624 | 316.476 |
| Efficiency [%] | 95.89 | 96.65 | 96.88 | 97.01 | 96.99 |

Table 3.6 Data of proposed model and three round windings models (Rated operating point)

| | D | F-1 | F-2 | F-3 |
|---|---|---|---|---|
| Rotational speed [rpm] | 2000 | 2000 | 2000 | 2000 |
| Winding resistance (one phase) [ohm] | 0.00181 | 0.00234 | 0.00235 | 0.00225 |
| Operating current [Arms] | 597.636 | 599.448 | 598.848 | 598.860 |
| Current density[Arms/mm$^2$] | 3.717 | 5.502 | 5.515 | 5.295 |
| Current phase angle [deg.] | 35 | 35 | 35 | 35 |
| Average torque [Nm] | 1506.994 | 1514.313 | 1513.317 | 1514.571 |
| Maximum torque [Nm] | 1661.028 | 1629.406 | 1626.905 | 1628.153 |
| Minimum torque [Nm] | 1344.691 | 1388.396 | 1389.390 | 1390.832 |
| Torque ripple [%] | 20.99 | 15.92 | 15.69 | 15.67 |
| Line voltage peak value [V] | 507.293 | 524.241 | 525.317 | 522.828 |
| Line voltage fundamental wave effective value [Vrms] | 333.518 | 333.906 | 333.600 | 332.602 |
| THD [%] | 15.77 | 15.84 | 15.64 | 15.59 |
| Copper loss [kW] | 1.936 | 2.521 | 2.524 | 2.423 |
| Total iron loss [kW] | 7.485 | 11.769 | 8.541 | 7.901 |
| Stator core iron loss [kW] | 4.440 | 4.637 | 4.618 | 4.603 |
| Rotor core iron loss [kW] | 0.646 | 0.543 | 0.540 | 0.540 |
| Magnet eddy current loss [kW] | 0.192 | 0.209 | 0.206 | 0.206 |
| Windings eddy current loss [kW] | 2.208 | 6.380 | 3.177 | 2.552 |
| Input [kW] | 306.203 | 302.867 | 305.883 | 306.887 |
| Output [kW] | 315.624 | 317.157 | 316.948 | 317.211 |
| Efficiency [%] | 97.01 | 95.49 | 96.51 | 96.75 |

# Conclusion

This paper mainly consists of two topics.

The first topic proposes a novel rotor structure which can enhance the efficiency of an IPMSM adopting concentrated windings in the wide-speed, middle-torque operating area. The proposed rotor structure employs both large flux barriers and a disproportional airgap on *q*-axis magnetic flux to concentrate the magnetic flux of PMs on *d*-axis while suppressing *q*-axis magnetic flux and the harmonic components of *dq*-axis magnetic flux. Furthermore, this topic also clarified the design method for a suitable rotor structure depending on its target operating area. The results are as follows. For the target wide-speed middle-torque operating area, the proposed rotor structure is most suitable. For a low-speed high-torque operating area, adopting only large flux barriers is most suitable. And for a high-speed low-torque operating area, adopting only a disproportional airgap is most suitable.

The second topic focuses on the reduction in eddy current loss of special rectangular windings in a high-torque IPMSM used for a wind generator. Three improvements have been discussed to reduce windings eddy current loss. Among them, removing a portion of windings and replacing a portion of windings with aluminum have been discussed to realize a tradeoff between eddy current and copper losses. The experimental results show that the efficiency of the prototype can exceed 97.5%. A high efficiency IPMSM with high slot factor and good heat dissipation used for a wind generator has been realized in this topic.

In conclusion, this paper proposed two models which can enhance the efficiency of IPMSMs while fully taking into account the cost and difficulty of manufacturing from the perspective of the rotor in topic I and the stator in topic II.

# Reference


[1] 「省エネモータの原理と設計法」(森本 茂雄・真田 雅之 著)

[2] 「埋込磁石同期モータの設計と制御」（武田 洋次, 森本 茂雄, 松井 信行, 本田 幸夫 著)

[3] トップランナーモータ - 日本電機工業会

[4] エネルギー白書 2021 経済産業省資源エネルギー庁

[5] J. Du, X. Wang and H. Lv, "Optimization of Magnet Shape Based on Efficiency Map of IPMSM for EVs," in *IEEE Transactions on Applied Superconductivity*, vol. 26, no. 7, pp. 1-7, Oct. 2016, Art no. 0609807, doi: 10.1109/TASC.2016.2594834.

[6] L. Fang, J. Jung, J. Hong and J. Lee, "Study on High-Efficiency Performance in Interior Permanent-Magnet Synchronous Motor With Double-Layer PM Design," in *IEEE Transactions on Magnetics*, vol. 44, no. 11, pp. 4393-4396, Nov. 2008, doi: 10.1109/TMAG.2008.2002001.

[7] B. Lee, S. Kwon, T. Sun, J. Hong, G. Lee and J. Hur, "Modeling of Core Loss Resistance for *d-q* Equivalent Circuit Analysis of IPMSM considering Harmonic Linkage Flux," in *IEEE Transactions on Magnetics*, vol. 47, no. 5, pp. 1066-1069, May 2011, doi: 10.1109/TMAG.2010.2099647.

[8] H. Lee et al., "Parameter Design of IPMSM With Concentrated Winding Considering Partial Magnetic Saturation," in *IEEE Transactions on Magnetics*, vol. 47, no. 10, pp. 3653-3656, Oct. 2011, doi: 10.1109/TMAG.2011.2157957.

[9] R. Tsunata, M. Takemoto, S. Ogasawara, and K. Orikawa, "Variable Flux Memory Motor Employing Double-Layer Delta-Type PM Arrangement and Large Flux Barrier for Traction Applications," in *IEEE Transactions on Industry Applications*, vol. 57, no. 4, pp. 3545-3561, July-Aug. 2021, doi: 10.1109/TIA.2021.3068329.

[10] M. N. Uddin and R. S. Rebeiro, "Online Efficiency Optimization of a Fuzzy-Logic-Controller-Based IPMSM Drive," in *IEEE Transactions on Industry Applications*, vol. 47, no. 2, pp. 1043-1050, March-April 2011, doi: 10.1109/TIA.2010.2103293.

[11] Z. Yang, F. Shang, I. P. Brown and M. Krishnamurthy, "Comparative Study of Interior Permanent Magnet, Induction, and Switched Reluctance Motor Drives for EV and HEV Applications," in *IEEE Transactions on Transportation Electrification*, vol. 1, no. 3, pp. 245-254, Oct. 2015, doi: 10.1109/TTE.2015.2470092.

[12] J. T. Chen and Z. Q. Zhu, "Winding Configurations and Optimal Stator and Rotor Pole Combination of Flux-Switching PM Brushless AC Machines," in *IEEE Transactions on Energy Conversion*, vol. 25, no. 2, pp. 293-302, June 2010, doi: 10.1109/TEC.2009.2032633.

[13] A. M. EL-Refaie et al., "Advanced High-Power-Density Interior Permanent Magnet Motor for Traction Applications," in *IEEE Transactions on Industry Applications*, vol. 50, no. 5, pp. 3235-3248, Sept.-Oct. 2014, doi: 10.1109/TIA.2014.2305804.

[14] A. M. EL-Refaie, "Fractional-Slot Concentrated-Windings Synchronous Permanent Magnet Machines: Opportunities and Challenges," in *IEEE Transactions on Industrial Electronics*, vol. 57, no. 1, pp. 107-121, Jan. 2010, doi: 10.1109/TIE.2009.2030211.

[15] M. -J. Kim et al., "Torque Density Elevation in Concentrated Winding Interior PM Synchronous Motor With Minimized Magnet Volume," in *IEEE Transactions on Magnetics*, vol. 49, no. 7, pp. 3334-3337, July 2013, doi: 10.1109/TMAG.2013.2241747.

[16] Ying Fan, Chao Tan, Siyu Chen and Ming Cheng, "Design and analysis of a new interior permanent magnet motor for EVs," *2016 IEEE 8th International Power Electronics and Motion Control Conference (IPEMC-ECCE Asia)*, 2016, pp. 1357-1361, doi: 10.1109/IPEMC.2016.7512487.

[17] Y. Kano, T. Terahai, T. Kosaka, N. Matsui and T. Nakanishi, "A new flux-barrier design of torque ripple reduction in saliency-based sensorless drive IPM motors for general industrial applications," *2009 IEEE Energy Conversion Congress and Exposition*, 2009, pp. 1939-1945, doi: 10.1109/ECCE.2009.5316493.

[18] Y. Xiao, Z. -Q. Zhu, J. -T. Chen, D. Wu and L. -M. Gong, "A Novel Spoke-type Asymmetric Rotor Interior PM Machine," *2020 IEEE Energy Conversion Congress and Exposition (ECCE)*, 2020, pp. 4050-4057, doi: 10.1109/ECCE44975.2020.9236321.

[19] M. Cirani, S. Eriksson and J. Thunberg, "Innovative Design for Flux Leakage Reduction in IPM Machines," in *IEEE Transactions on Industry Applications*, vol. 50, no. 3, pp. 1847-1853, May-June 2014, doi: 10.1109/TIA.2013.2289969.

[20] H. Xu and J. Li, "A Sleeve-Free Interior Permanent Magnet High Speed Motor with Non-Uniform Airgap," 2019 *IEEE International Electric Machines & Drives Conference (IEMDC)*, 2019, pp. 733-738, doi: 10.1109/IEMDC.2019.8785366.

[21] Z. Wu, Y. Fan, C. H. T. Lee, D. Gao and K. Yu, "Vibration Optimization of FSCW-IPM Motor Based on Iron-Core Modification for Electric Vehicles," in *IEEE Transactions on Vehicular Technology*, vol. 69, no. 12, pp. 14834-14845, Dec. 2020, doi: 10.1109/TVT.2020.3041336.

[22] G. De Donato, F. Giulii Capponi, G. A. Rivellini and F. Caricchi, "Integral-Slot Versus Fractional-Slot Concentrated-Winding Axial-Flux Permanent-Magnet Machines: Comparative Design, FEA, and Experimental Tests," in *IEEE Transactions on Industry Applications*, vol. 48, no. 5, pp. 1487-1495, Sept.-Oct. 2012, doi: 10.1109/TIA.2012.2210011.

[23] D. Wu and Z. Q. Zhu, "Influence of Slot and Pole Number Combinations on Voltage Distortion in Surface-Mounted Permanent Magnet Machines With Local Magnetic Saturation," in *IEEE Transactions on Energy Conversion*, vol. 30, no. 4, pp. 1460-1471, Dec. 2015, doi: 10.1109/TEC.2015.2436065.

[24] J. A. Tapia, J. Pyrhonen, J. Puranen, P. Lindh and S. Nyman, "Optimal Design of Large Permanent Magnet Synchronous Generators," in *IEEE Transactions on Magnetics*, vol. 49, no. 1, pp. 642-650, Jan. 2013, doi: 10.1109/TMAG.2012.2207907.

[25] H. Chen, R. Qu, J. Li and B. Zhao, "Comparison of interior and surface permanent magnet machines with fractional slot concentrated windings for direct-drive wind generators," *2014 17th International Conference on Electrical Machines and Systems (ICEMS)*, 2014, pp. 2612-2617, doi: 10.1109/ICEMS.2014.7013942.)

[26] T. M. Jahns, "The expanding role of PM machines in direct-drive applications," *2011 International Conference on Electrical Machines and Systems*, 2011, pp. 1-6, doi: 10.1109/ICEMS.2011.6073289.

[27] G. Bacco, N. Bianchi and F. Luise, "High-Torque Low-Speed Permanent Magnet Assisted Synchronous Reluctance Motor Design," *2019 IEEE International Electric Machines & Drives Conference (IEMDC)*, 2019, pp. 644-649, doi: 10.1109/IEMDC.2019.8785236.

[28] Y. -S. Park, S. -M. Jang, M. -M. Koo, J. -Y. Choi and S. -Y. Sung, "Comparative Investigation on Integrated System of Permanent Magnet Synchronous Generator and Power Converter Based on Machine Topology for Small-Scale Wind Power Application," in *IEEE Transactions on Magnetics*, vol. 49, no. 7, pp. 3846-3849, July 2013, doi: 10.1109/TMAG.2013.2248700.

[29] Z. Gaojia and L. Longnv, "Design Optimization of a Direct-Drive PM Wind Generator With Flux-Modulation Structure," 2020 IEEE International Conference on Applied Superconductivity and Electromagnetic Devices (ASEMD), 2020, pp. 1-2, doi: 10.1109/ASEMD49065.2020.9276166.

[30] J. A. Baroudi, V. Dinavahi and A. M. Knight, "A review of power converter topologies for wind generators," *IEEE International Conference on Electric Machines and Drives*, 2005., 2005, pp. 458-465, doi: 10.1109/IEMDC.2005.195763.

[31] Y. Zhao, D. Li, T. Pei and R. Qu, "Overview of the rectangular wire windings AC electrical machine," in *CES Transactions on Electrical Machines and Systems*, vol. 3, no. 2, pp. 160-169, June 2019, doi: 10.30941/CESTEMS.2019.00022.

[32] P. B. Reddy, A. M. El-Refaie, K. Huh, J. K. Tangudu and T. M. Jahns, "Comparison of Interior and Surface PM Machines Equipped With Fractional-Slot Concentrated Windings for Hybrid Traction Applications," in IEEE Transactions on Energy Conversion, vol. 27, no. 3, pp. 593-602, Sept. 2012, doi: 10.1109/TEC.2012.2195316.

[33] S. Zhu, K. Paciura and R. Barden, "Application of Flat Rectangular Wire Concentrated Winding for AC loss Reduction in Electrical Machines," *2021 IEEE Energy Conversion Congress and Exposition (ECCE)*, 2021, pp. 4619-4623, doi: 10.1109/ECCE47101.2021.9595683.

[34] R. Wrobel, D. Staton, R. Lock, J. Booker and D. Drury, "Winding Design for Minimum Power Loss and Low-Cost Manufacture in Application to Fixed-Speed PM Generator," in *IEEE Transactions on Industry Applications*, vol. 51, no. 5, pp. 3773-3782, Sept.-Oct. 2015, doi: 10.1109/TIA.2015.2434802.

[35] X. Tao, M. Takemoto, R. Tsunata and S. Ogasawara, "Novel Rotor Structure Employing Large Flux Barrier and Disproportional Airgap for Enhancing Efficiency of IPMSM Adopting Concentrated Winding Structure," in *IEEE Access*, vol. 11, pp. 2848-2862, 2023, doi: 10.1109/ACCESS.2022.3232843.

[36] K. Yamada, “Development and Evaluation of an Axial Gap Motor Using Neodymium Bonded Magnet,” *IEEE Trans. Industry Applications*, vol. 54, no. 1, pp. 254-262, Jan.-Feb. 2018, doi: 10.1109/TIA.2017.2710123.

[37] M. Paradkar and J. Böcker, "Analysis of eddy current losses in the stator windings of IPM machines in electric and hybrid electric vehicle applications," *8th IET International Conference on Power Electronics, Machines and Drives (PEMD 2016)*, 2016, pp. 1-5, doi: 10.1049/cp.2016.0320.

[38] X. Ge, Z. Q. Zhu, G. Kemp, D. Moule and C. Williams, "Optimal Step-Skew Methods for Cogging Torque Reduction Accounting for Three-Dimensional Effect of Interior Permanent Magnet Machines," in *IEEE Transactions on Energy Conversion*, vol. 32, no. 1, pp. 222-232, March 2017, doi: 10.1109/TEC.2016.2620476.

[39] P. B. Reddy, T. M. Jahns and T. P. Bohn, "Transposition effects on bundle proximity losses in high-speed PM machines," *2009 IEEE Energy Conversion Congress and Exposition*, 2009, pp. 1919-1926, doi: 10.1109/ECCE.2009.5316037.

[40] I. Petrov, M. Polikarpova, P. Ponomarev, P. Lindh and J. Pyrhönen, "Investigation of additional AC losses in tooth-coil winding PMSM with high electrical frequency," *2016 XXII International Conference on Electrical Machines (ICEM)*, 2016, pp. 1841-1846, doi: 10.1109/ICELMACH.2016.7732774.

[41] M. S. Islam, I. Husain, A. Ahmed and A. Sathyan, "Asymmetric Bar Winding for High-Speed Traction Electric Machines," in *IEEE Transactions on Transportation Electrification*, vol. 6, no. 1, pp. 3-15, March 2020, doi: 10.1109/TTE.2019.2962329.

[42] Y. Li, Z. Q. Zhu and G. J. Li, "Influence of Stator Topologies on Average Torque and Torque Ripple of Fractional-Slot SPM Machines With Fully Closed Slots," in *IEEE Transactions on Industry Applications*, vol. 54, no. 3, pp. 2151-2164, May-June 2018, doi: 10.1109/TIA.2018.2799178.

# Publications lists

## Journal Papers:

[1] X. Tao, M. Takemoto, R. Tsunata and S. Ogasawara, "Novel Rotor Structure Employing Large Flux Barrier and Disproportional Airgap for Enhancing Efficiency of IPMSM Adopting Concentrated Winding Structure," in *IEEE Access*, vol. 11, pp. 2848-2862, 2023, doi: 10.1109/ACCESS.2022.3232843.

[2] X. Tao, M. Takemoto, R. Tsunata and S. Ogasawara, "Reduction in Eddy Current Loss of Special Rectangular Windings in High-torque IPMSM Used for Wind Generator," in *IEEE Access*, doi: 10.1109/ACCESS.2023.3236105.